Developing an integrated methodology for assessing risk and impact of illegal alluvial mining-related environmental stressors in the Pra river basin, Ghana.

ETH Zurich - Environmental Engineering

Developing an integrated methodology for assessing risk and impact of illegal alluvial mining-related environmental stressors in the Pra river basin, Ghana.

Master Thesis

September 13, 2020

CLOC West Africa - Network for Water and Life (NEWAL)
Sabine Nicole Hain
ETH Zurich Institute of Environmental Engineering
Hydrology and Water Resources Management
Supervised by Prof. Dr. Peter Molnar and Dr. Darcy Molnar

ETH Zürich

ACKNOWLEDGEMENTS I must extend my thanks to Prof. Dr. Peter Molnar and Darcy Molnar for guiding me throughout this thesis and providing me with excellent input. I greatly enjoyed our many discussions and will carry many of the learnings with me in the future. I must also acknowledge the entire NEWAL planning team for organizing this project and enabling it in the first place.

This thesis was a collaborative effort, pulling together expertise from many different disciplines. I was fortunate to be able to rely on expert inputs from a variety of individuals, to whom I am extremely grateful. These are:

Raymong Djangma from the Pra Basin Secretariat of the Water Resources Commission
Dr. Marius Floriancic and Dr. Beatrice Marti from the Environmental Laboratory of the Institute of Environmental Engineering, ETH Zurich
Dr. Yang Yue from the Institute of Environmental Engineering Chair of Industrial Ecology, ETH Zurich
Dr. Mirko Winkler and soon-to-be Dr. Dominik Dietler from the Swiss Tropical and Public Health Institute

Galamsey in the Pra Basin
Developing an integrated methodology for assessing risk and impact of illegal alluvial mining-related environmental stressors in the Pra river basin, Ghana.

Supervised by Prof. Dr. Peter Molnar and Dr. Darcy Molnar

Hydrology and Water Resources Management
Institute of Environmental Engineering, IfU
Department of Civil, Environmental and Geomatic Engineering, D-BAUG
Swiss Federal Institute of Technology Zurich, ETH

Cover picture: Artisanal small-scale gold mining in Ghana (left and centre photo, own images); Lake Bosumtwi (own image).

Developing an integrated methodology for assessing risk and impact of alluvial gold-mining-related environmental stressors in the Pra river basin, Ghana

Sabine Nicole Hain

Abstract

Galamsey is a local Ghanaian term that describes small-scale illegal gold mining, primarily in rivers. This thesis investigates illegal alluvial mining-related risks and impacts in the Pra basin of Ghana using a spatially distributed GIS-based approach. Land use, river and geomorphology and environmental pollution were investigated using exclusively public data. Land use was assessed based on Sentinel-2 imagery from Dec. 2018 - Jan. 2020. Iso Cluster Unsupervised Classification in ArcGIS was conducted using a Modified Normalized Difference Water Index (MNDWI)-based image stack to optimally detect mines. In total, 0.95% of the basin are covered in open mining pits, resulting in approx. 2% of the basin if mining-related bareland is additionally considered. The proposed detection method showed high efficiency compared to supervised classification, and an overall accuracy of 91.2%. River and geomorphological impacts of mining were assessed using the Universal Soil Loss Equation (USLE), channel stream power based on mean discharge and slope, as well as actual landscape and riverbed elevation change derived from a DEM of Difference between 2000 and 2015. USLE predicted low rates of erosion across the basin, but was shown to be an insufficient tool to model the dominant processes of gully and channel erosion which are exacerbated by alluvial mining. Mean landscape elevation change in the basin over 15 years was -0.87 m, with mining areas experiencing a significantly elevated mean loss of -3.96 m in this period. All main channels showed significant erosion, with the largest riverbed elevation change taking place in the Lower Pra reach. Stream power indicated concordant behaviour, but requires further on-site verification before it can be used as an indicator. Environmental pollution was assessed in a structured literature review that identified over 2400 heavy metal concentration datapoints of 12 different metals in 168 locations and all environmental compartments with exception of ambient air. 36% of datapoints exceeded WHO recommended limits for the respective environmental compartment. Widespread heavy metal pollution was evident throughout the basin even in locations far away from mining sites, despite no or minimal other anthropogenic and geogenic sources in the basin. Groundwater was found to be heavily polluted with mercury, with 82.1% of measurements exceeding WHO recommended limits. Risk predictions were made based on existing surface water abstraction points in the basin using Pearson Correlation Analysis. Various potential predictors of pollution were investigated. Upstream fraction of mining land use and local channel slope were identified as the only significant predictors of pollution risk. Pollution pathway tracing was conducted to better understand the mechanisms of pollution transport throughout the basin. The analysis was conducted using results from the environmental pollution survey, additional literature review, a specifically developed pollutant routing algorithm, and 2D floodplain analysis. Overall, river-driven processes including contamination via floodplain inundation and aquifer recharge from polluted surface waters were shown to be the dominant pollution transfer processes in the basin, thereby providing a foundation for targeted future research and remediation strategies.

Abbreviations

AD: Agriculture with low water content
ALOS 3D World: Advanced and Land Observing Satellite Digital Elevation Model 3D World
B: Built-up/Bareland
C: Crop management factor (USLE)
CC: Closed canopy
OC: Open canopy
AW: Agriculture with high water content
CCR: Return period of channel capacity exceedance
CO: Corrected cover
CTS: Channel Terrain Steepness Index
DEM: Digital Elevation Model
ESDAC: European Soil Data Centre
ETH: ETH Zurich
FAO: Food and Agriculture Organization
FCC: False Colour Composite Image
GIS: Geoinformation System
GloSEM: Global Soil Erosion Map provided by European Soil Data Centre ESDAC
GW: Groundwater
GWCL: Ghana Water Company Limited
HEC-RAS: Hydrologic Engineering Center – River Analysis System
IWRM: Integrated Water Resources Management
JAXA: Japanese Aerospace Exploration Agency
K: Soil erodibility (USLE)
LS: Length-slope factor (USLE)
M: Mining – Open pits
MNDWI: Modified Normal Difference Water Index
NDVI: Normalized Difference Vegetation Index
NEWAL: Network for Water and Life
NIR: Near-Infrared
OC: Organic matter content
OCHA: United Nations Office for the Coordination of Humanitarian Affairs
P: Erosion control practice factor (USLE)
PPE: Personal Protective Equipment
R: Rainfall erosivity (USLE)
RMSE: Root mean square error
SDGs: Sustainable Development Goals
SED: Sediment
SO: Soil
SRTM: Shuttle Radar Topography Mission
SSED: Suspended sediment
SW: Surface water
SWIR: Shortwave Infrared
TCI: True Colour Image
TOA: Top-of-Atmosphere Reflectance
USGS: United States Geological Survey
USLE: Universal Soil Loss Equation
W: Water

WHO: World Health Organization
WRC: Water Resources Commission

Contents

1. Introduction

The Pra River Basin is the largest river basin in the southwest of Ghana and is home to the country's only significant natural freshwater lake, Lake Bosumtwi (see Figure 1). A large number of licensed industrial and small-scale gold mines, as well as unlicensed illegal artisanal mines referred to as "Galamsey" are active in the area. "Galamsey" stands for "gather them and sell" and has seen a massive upsurge in the Pra basin since 2004 despite strict legislation and ongoing national attention [1], causing a wide range of environmental impacts. The chief regulatory and management body for water resources in Ghana, the Water Resources Commission (WRC), has established the Pra River Basin as a priority basin for an Integrated Water Resources Management (IWRM) scheme in order to effectively coordinate water planning efforts, and in doing so has established a River Basin Board and a Secretariat to oversee IWRM development. An IWRM plan, published by the Secretariat in 2012, identified Galamsey as the top threat to the basin due to its significant impact on the environment [2].

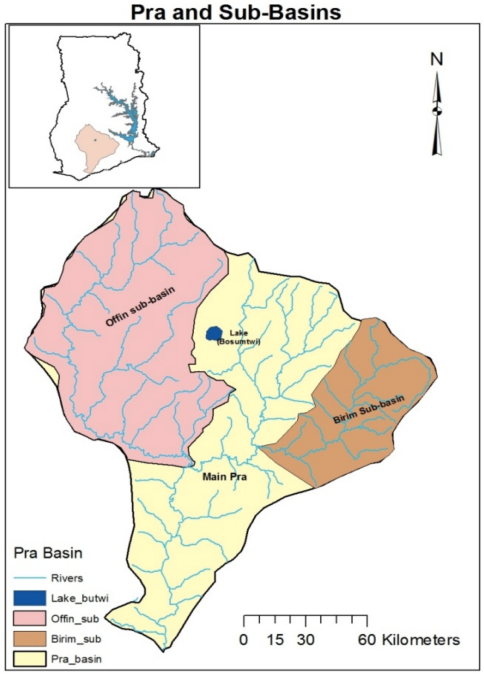

Figure 1: Pra river basin and subbasins Offin and Birim, shown within the context of Ghana [2]

1.1. The Galamsey mining process

Galamsey engages two main types of mining: Either directly along and within rivers, referred to as alluvial mining, or in deep underground mines. Alluvial artisanal mining in the basin, which is the focus of this project, encompasses the extraction of gold and, to a smaller extent, diamonds within alluvial deposits and denuded outcrops [3, 4] through the dredging of riverbeds, -banks and floodplains along the Ashanti gold belt and the Birim diamond field. However, dredging of the riverbeds is strictly forbidden [5] according to Ghanaian law. Gold mining, both of licensed and illegal nature, takes place primarily in the northern sections of the basin, with little known mining activity in the lower reaches [6]. The gold ore exploited by artisanal miners in the Ashanti belt is Quartz-Fe/As sulphide gold lode [7]. Diamond mining is confined to the deposits of the upper Birim reach. The process of alluvial mining of both gold and diamonds entails the removal of vegetation, either from cropland or forests, the removal of the topsoil, and subsequent dredging of alluvial sediment [8]. The dredging of sediment is conducted layer by layer, with each layer being mined

for gold and then deposited on-site until this forms large, deep pits. Large dredging machinery is frequently used, allowing these pits to reach widths of over 100 metres. The majority of Galamsey operations are known to be within close proximity of large-scale industrial mines [9].

In order to extract gold ores, the sediment is comminuted and concentrated via gravity separation. Following concentration, gold separation from ores is achieved using mercury or cyanide. Mercury amalgamation is more frequently applied amongst Galamsey practices in the basin, whereas cyanide is the preferred method of gold leaching in large-scale industrial mines [10]. Comminution, concentration and amalgamation are usually completed directly on-site with no management of tailings. Some operations attempt to filter mercury from these tailings for re-use to save costs. Mercury is usually handled with no personal protective equipment (PPE). Tailings of these processes are released directly back into water bodies or dumped on nearby soils and sediment hills. Mine tailings are highly turbid due to very high suspended sediment content from the comminution process, and can be laced with residual mercury and other toxic heavy metals [11, 12, 3]. Diamond ores are extracted similarly, with little to no comminution and without the need for amalgamation [8].

The gold amalgam is usually transported off-site for combustion in smelting ovens. Smelting ovens separate gold and mercury in the amalgam by vaporizing mercury, which has a lower boiling point. The smelting process is often conducted without PPE and releases toxic mercury fumes into ambient air, where it can be transported over wide distances and eventually deposits either on and in humans, on soils, in surface waters or on crops and vegetation [13]. The open pits resulting from the mining process mostly remain once the mine is abandoned, with little to no reclamation of the original land.

1.2. Environmental impacts of Galamsey

Galamsey incurs various environmental stressors that have long-lasting effects on the ecosystem, as well as on human health. Table 1 summarizes the main groups of environmental stressors and their related risks and impacts.

Acid mine drainage is of particular importance due to the mining of iron sulphide ores in Galamsey operations. The dredging and comminution process increases the exposed surface area of the rock. Exposure to air and water results in the oxidation of sulphides to sulphuric acid, which lowers pH and increases the mobilization of heavy metals contained within the host rock, as well as mercury which is added to form gold amalgam [14]. Metals such as lead, cadmium and arsenic can then leach into surface waters, groundwater, sediment and soils, entering the food chain and leading to human health impacts.

Table 1: Environmental stressors and potential risks and impacts in the Pra basin [15].

Environmental stressor	Risks and impacts of alluvial mining
Land use and land cover change	Deforestation Loss of cropland and other habitat Biodiversity losses Flood risk Loss of nutrient buffering zones along rivers
River and geomorphological changes	Increased soil erosion from bareland Increased sediment delivery to river from mining practices Riverbank and -bed erosion and aggradation Large land mass changes Turbidity and siltation of rivers Dustiness of soils Change in floodplain behaviour
Environmental pollution	Heavy metal pollution from host rock and mercury addition Acid mine drainage due to oxidation of sulphide lodes Deterioration of physico-chemical parameters of water Increases in water treatment costs Loss of viable irrigation and drinking water resources Loss in soil fertility and crop die-off Human health effects

1.3. Current state of research in the Pra basin

Land use has been previously assessed in the basin, but without a focus on optimizing mine detection and solely by using algorithms that rely on the time-intensive collection of training samples [1]. Initial research on river and geomorphology is inconclusive, with simulations not lining up with observations [16, 17] and no research detailing Galamsey's concrete impact. Other research has determined dangerous levels of heavy metal accumulation in the environment, including metals such as mercury, lead, cadmium and arsenic in surface waters, soils, river sediments and groundwater [18, 19, 7, 20, 13] in mostly isolated regional studies. Concerningly, several metals have been shown to mobilize over long distances, even contaminating lower sections of the basin where mining does not occur to a large degree [7]. However, no other anthropogenic activities exist that can explain the high heavy metal concentrations in the basin [3].

Despite the rising awareness and urgency of Galamsey-related effects within the Pra River Basin, studies investigating its risk and impact in a spatially distributed, holistic fashion coupling different environmental compartments have not yet been conducted. Previous research has focused on sampling campaigns of an individual location or few point-source measurements with no proposed interlinkages between environmental compartments or the ability to propose concrete mitigation and adaptation mechanisms. The Business-As-Usual scenario report of the Pra River Basin [6] describes the lack of consolidated spatial information and the evaluation of environmental stressors in isolation and without environmental context as a key hurdle towards meaningful action and highlights the need for an integrated assessment tool such as a GIS-based approach. The lack of mechanistic understanding additionally renders remediatory action difficult and does not allow for targeted allocation of limited resources to mitigate effects.

It follows that Galamsey-related effects and their relation to public health, agriculture and ecosystems is

a growing concern for multiple stakeholders [2, 6, 21]. Many riverside communities are dependent on the river network for their main water supply. The region is also one of Ghana's primary cocoa production areas [2], and farmers have expressed concerns over diminishing crop yields and diminished quality of crops. The cost of treatment as well as operational instability of the surface water abstraction plants within the basin operated by Ghana Water Company Limited (GWCL), Ghana's state-owned water provider, have also been rising in the recent past, due to increasingly turbid waters, silt-clogging and general reductions in water quality that can be traced back to mining processes [6, 22].

2. Research goals and guiding questions

This thesis is conducted within the context of the Cluster of Cooperation "Network for Water and Life" (NEWAL) in West Africa, a collaborative project between academic institutions in Ghana, Cote d'Ivoire, Liberia, and Switzerland. NEWAL aims to encourage an integrated research approach to enable the transition to more sustainable and resilient societies in line with the Sustainable Development Goal (SDGs). Galamsey is at the interface of the Ghanaian economy, society and environment, therefore directly impacting multiple SDGs. In line with NEWAL's mission, the goal of this thesis is to assess environmental stressors and related risks and impacts due to illegal alluvial mining in a comprehensive and spatially distributed approach. The following research goal underlines this purpose:

Comprehensively analyze alluvial mining-related risks and impacts on land use, river and geomorphology and environmental pollution, by interfacing publicly available data and developing methods where required to assess impact pathways in order to prioritize further action.

In order to achieve these research goals, the following guiding questions have been defined:

1. What is the magnitude of illegal alluvial mining and related impacts in the basin? Where are these mines located?
2. How does mining affect river and geomorphological processes such as erosion in the basin?
3. How significant is heavy metal contamination within the basin?
4. What are the dominant impact pathways for mining-related heavy metal pollution in the basin?
5. Can we answer these questions using exclusively public data?

This thesis employs various methods to quantify the effects of Galamsey on the outlined environmental stressors of land use change, river and geomorphological change, and environmental pollution, as well as pollutant pathways, to hopefully enable sustainable change that preserves ecosystems and livelihoods.

3. Materials and Methods

Potential environmental stressors and their related risks and impacts were investigated along three main workstreams:

- Land use and land cover change
- River and geomorphological changes
- Environmental pollution and pollutant transfer pathways

The diverse methods applied to answer the main research questions are outlined in the following sections.

3.1. Study Area

The Pra basin is located in the Southwest of Ghana between latitudes 5°N and 7°30'N and longitudes 2°30'W and 0°30'W, and is the largest of the Southwestern basins of Ghana [2]. The basin overlaps with Ghana's main gold producing region over the Ashanti gold belt [8]. The main Pra river originates in the Kwahu plateau and flows 240 km into the Golf of Guinea, joined by its main tributaries Offin (Western branch) and Birim (Eastern branch) along the way. The basin is the most densely populated in Ghana at over 4 million inhabitants in an area of 23188 km^2, of which 58% depend on the river network for their water supply [2, 6]. 42% of the population have no access to potable water, relying on untreated surface waters to meet their needs [6]. The topology is hilly and undulating with a maximum elevation of 848 m.a.s.l. The hydrogeology is characterized by crystalline basement rocks and the Birimian and Tarkwaian formations, which are granitic and gneissic and possess no primary porosity [23, 24]. The climate in the basin is classified as wet sub-equatorial with two rain seasons (May-June and September-November) and annual precipitation ranging between 1300 and 1900 mm [4]. The basin is dominated by both subsistence and cash crop farming. The main cash crops are cocoa and palm, which are grown intensively in the basin. Subsistence crops grown in the basin in descending order of yields are cassava, maize, plantain, taro, yam, rice, groundnuts, and cowpea [25]. Individual irrigation systems exist for rice and vegetables such as tomatoes, peppers and eggplant, but irrigation is not practised to a high degree within the basin. However, decreasing levels of precipitation due to climate change are expected to lead to a marked increase in irrigation requirements to uphold previously rain-fed croplands [26].

3.2. Data

Sentinel-2 1C level images at 10-60 m resolution were accessed through the United States Geological Survey (USGS) Earth Explorer. Seven tiles spanning the Pra basin were downloaded after filtering for minimal cloud cover ($< 1\%$) during the dry months of December - February in the years 2018 to 2020. The USGS Earth Explorer database provides images that have been previously subjected to atmospheric and radiometric correction, as well as geometric and orthorectification. Sentinel-2 products at Level 1C therefore required no additional processing following the download [27]. The wide search window was required to achieve optimal visibility due to cloud cover. Terrain data was accessed as a 30 m resolution 1 Arc-Second Global Shuttle Radar Topography Mission (SRTM) Digital Elevation Model (DEM) from the year 2000. The JAXA ALOS 3D World DEM from the year 2015 was also retrieved from the Japanese Aerospace Exploration Agency to analyze landscape evolution in the basin.

Rainfall erosivity values in the basin were available through the GloSEM Global Soil Erosion Map at 25 km resolution through the European Soil Data Centre (ESDAC) [28]. Soil texture parameters were sourced from the FAO Digital Soil Map of the World [29]. Shapefiles of basin boundaries as well as regional and

district-level boundaries were available through the Geoscience Lab Landscape Portal [30] and the UN Centre of Humanitarian Data OCHA [31] respectively.

OpenLandMap provides global data on annual mean, minimum and maximum monthly runoff in raster format from 1960-2015 [32]. Additionally, simulated data for individual locations within the basin was available within the 2012 IWRM Pra Basin report from the Pra Basin Secretariat of the Water Resources Commission [2]. The simulated flow data from the IWRM report were based on hydrographs from the gauging station of Twifo-Praso between 1999 and 2006 which were not available for this project. Ghana Water Company Limited (GWCL) water abstraction sites were also listed in this report.

The open-source Hydrologic Engineering Center - River Analysis System (HEC-RAS) by the U.S. Army Corps of Engineers was downloaded over the official website [33]. Data was processed in the ArcGIS Desktop V. 10.7.1 GIS suite, in HEC-RAS and in MATLAB R2020a.

3.2.1. Validation of the FLO1K annual mean monthly flow dataset

The FLO1K discharge values [32] from OpenLandMap provide spatially distributed information on channel discharge within the basin for the years 1960-2015. In order to verify their accuracy, the mean FLO1K discharge values were compared to the simulated discharges at the locations listed within the Pra Basin IWRM report [2] during the period of 1999 to 2006.

The mean FLO1K discharge between 1999 and 2006 was computed by averaging the corresponding raster layers in ArcGIS. The locations with discharge values in the IWRM report (Offinso, Adiembra, Bekwai, Ampunyase, Dunkwa, Osino, Akim Oda, Mmuronem, Assin Praso, Twifo Praso, Daboase) were then plotted on the averaged FLO1K map and their local values at these sites were extracted. The values were compared using linear regression.

3.3. Understanding the life cycle of alluvial mining

In order to gain an understanding of the life cycle of an alluvial mine from initial excavation to potential reclamation or abandonment, the progression of a mining field was assessed using Google Earth temporal imagery available through Google Earth Pro. The region of the upper Birim near Akyem Mampong was selected due to availability of temporal imagery at this site.

3.4. Land Use and Land Cover Change

3.4.1. Delineation of the basin and river network

The Pra basin was delineated based on the 30 m SRTM DEM using the Spatial Analyst Toolkit available in ArcGIS. The DEM was filled to remove sinks. Flow direction and flow accumulation were computed using the Spatial Analyst Hydrology module. A drainage threshold of 7000 raster pixels, corresponding to 6.3 km^2 upstream drainage area, was set to differentiate between hillslope and channel flow. Verification of the drainage threshold was conducted based on ground truth validation of Sentinel-2 imagery and Google Earth images. Upon selection of the drainage threshold, the streams were extracted using the Streams to Feature function in ArcGIS Spatial Analyst Toolbox.

3.4.2. Land use classification and optimization of the mine detection process

In order to determine the magnitude and scope of alluvial mining within the basin and to provide a foundation for further spatial analysis, a land use assessment was conducted in ArcGIS. The Sentinel-2 missions provid multispectral imagery for 13 bands at 10, 20 or 60 m resolution. Two types of classification algorithms exist: Supervised classification, which relies on the selection of training samples and the accurate detection of ground truth, and unsupervised classification, which automatically detects distinct spectral signatures in a given image or stack. Both types are available within the ArcGIS suite. Supervised classification is time-intensive and requires the definition of training samples by the user, which can introduce a significant user error. For this reason, unsupervised classification using the Iso Cluster Classification algorithm in ArcGIS was selected for this project. This allows an efficient classification using minimal user inputs, therefore streamlining the automatic detection process. [34]

Iso Cluster Classification requires a "stack" and a "minimum number of classes" as input. In land use classification, a "stack" describes composite images of desired bands (e.g. a true colour red-green-blue or false-colour composite image) or indexes, such as the Normalized Difference Vegetation Index (NDVI) or the Modified Normalized Difference Water Index (MNDWI). Mining pits have three distinguishable features that are relevant for detection based on spectral signature: They are filled with water, they are highly turbid, and they are unvegetated. The MNDWI, which differences the green band (Sentinel band 3) and shortwave infrared (SWIR) (Sentinel bands 11 and 12), is frequently used for the enhancement of water features and moisture content in satellite imagery [35, 36], while the NDVI can distingiuish between vegetated and non-vegetated areas. Initial image analysis showed that open mining pits present with high Top-of-Atmosphere Radiance (TOA) in both the blue and green bands (bands 2 and 3), with distinctly lower TOA in SWIR2 (band 12) compared to other bands. Due to this spectral signature, a stack approach based on the MNDWI was chosen to first identify wet patches. A false-colour composite image was created for all tiles using the ArcGIS Image Analysis extension consisting of the blue, green and SWIR2 bands of the Sentinel-2 imagery. The SWIR2 band was selected over SWIR1 in initial testing, as the MNDWI computed with SWIR2 showed higher sensitivity to waterbodies compared to SWIR1. The false colour composites drastically simplified the visual identification of open mining pits and showed adequate class separation based on moisture content. To additionally support the separation of vegetated and non-vegetated area, as well as turbid from non-turbid waters, the true colour image (TCI) was added to the stack. The red band (B4) aids in this distinction. A minimum number of classes of 30 was chosen to ensure sufficient class separation based on initial trial-and-error (see Appendices C and B for calculation procedures, classification images and additional details on the applied methodology).

The Iso Cluster Classification algorithm's output (classified image with 30 distinct classes) was then manually post-processed by assigning and aggregating the automatically detected classes to desired land use classes based on Google Earth and Sentinel-2 imagery. The classified tiles were then mosaiced and clipped to the Pra basin boundary. Remaining cloud cover and larger areas of misclassified land were manually corrected in post-processing by removing the wrongly classified areas with polygon extraction. Following the classification procedure, the spectral signatures across all bands were extracted from a single tile. The average spectral signatures in Top of Atmosphere reflectance (TOA) of each band were computed for each land use class for comparative purposes.

3.4.3. Accuracy assessment

Approximately 200 samples per land use class were selected based on the TCI and the MNDWI-based composite image as "ground-truth". The corresponding land use classification was then extracted in ArcGIS and compared to the ground-truth in a confusion matrix.

3.4.4. Land use in proximity of rivers

Land use in the proximity of a river can substantially impact river morphology, hydrology, flooding behaviour, water quality, riverine vegetation, and riverbank and -bed erosional and depositional processes. Additionally, due to the comprehensive ban [5] on direct alluvial mining in Ghana, it was of interest to analyze the character of current "Galamsey" operations with regard to their distance to the main river network. In order to extract this composition of the river buffer, defined in this case as the area within a given distance from the midline of a river, a buffer analysis of the river network and land use was conducted using the Buffer function from the ArcGIS Proximity toolkit. 12 buffer distances (50 m, 100 m, 200 m, 300 m, 500 m, 750 m, 1000 m, 1500 m, 2500 m, 2750 m, 3000 m , 3500 m) were selected based on an initial visual interpretation of the Sentinel-2 and Google Earth images.

3.5. River and geomorphology changes

Various methods were used to assess changes to river and geomorphology in the basin. The Universal Soil Loss Equation (USLE) was applied to the basin to model landscape erosion processes. Stream power computed using annual mean monthly discharge and the channel slope was computed to approximate transport capacity of the rivers, as well as to highlight zones that are particularly exposed to bank and bed erosion or deposition. To validate the simulated findings of the USLE and the stream power assessment, a DEM of Difference was computed using the 2000 SRTM and the 2015 ALOS 3D World DEMs.

3.5.1. Universal Soil Loss Equation (USLE)

Annual soil loss was modelled using the USLE according to the methodology outlined in the USLE Handbook (see Equation 1) [37].

$$A = R \cdot K \cdot LS \cdot C \cdot P \tag{1}$$

A	Annual soil loss [t/ha/a]
R	Rainfall erosivity index
K	Soil erodibility index
LS	Length-slope steepness index
C	Crop management index
P	Erosion control practice index

As discussed in Section 3.2, the GloSEM rainfall erosivity raster at 25 km resolution from the European Soil Data Centre (ESDAC) was applied in order to avoid the high processing requirements needed to assemble higher resolution rainfall erosivity data. Soil erodibility was computed based on FAO soil texture data from the FAO Soil Map of the World and the K factor computation procedure by Wischmeier and Smith [37] in Equation 2. The Slope-Length Steepness Index was computed using the 30 m SRTM DEM based on the formula by Wischmeier and Smith in Equation 3 [37] and supplementary ArcGIS computation notes provided by ESDAC [38]. The crop management factor C was based on the land use classification and reported literature values by land use, listed in Table 2. Erosion control practice index P was set to 1, since no large-scale erosion protection practices are known to be applied within the basin.

$$100K = 2.1 * M^{1.14} * (12 - a) + 3.25(b - 2) + 25(c - 3) \quad (2)$$

K	Soil erodibility factor
M	(Percent silt)*(100 - Percent clay)
a	Percent organic matter
b	Soil structure class = 2
c	Profile-permeability class = 5

$$LS = \left[\frac{FlowLength}{22.13}\right]^{m} * (65.41Sin^2(Slope) + 4.56Sin(Slope) + 0.065) \quad (3)$$

LS	Length-slope steepness index
$FlowLength$	Flow length derived from DEM in ArcGIS
$Slope$	Slope of a pixel in radians
m	LS exponent: m = 2 if slope < 0.01%; m = 3 if slope is 0.01-0.035%; m = 4 if slope is 0.035-0.05%; m = 5 if slope >0.05%;

Table 2: Crop management factors C by land use class. Open mining pits are considered as C = 1 due to their fallow bareland nature. The land use classes were taken from the results of the land use classification.

Land Use Class	**C Factor**
Closed canopy	0.0001 [17, 39, 40]
Open canopy	0.005 [41]
Agriculture - High water content	0.15 [41]
Agriculture - Low water content	0.3 [41]
Mining - Open pits	1 [42]
Built-up/Bareland	0.35 [17, 39, 40]
Water	0 [17, 39, 40]
Corrected cover	0 [17, 39, 40]

3.5.2. Stream power

Stream power was calculated according to Equation 4. Mean annual flow was based on the FLO1K discharge values over the time period of 1960 to 2015. Channel slope was computed in ArcGIS using the 30 m SRTM DEM.

$$\Omega = Q \cdot I \quad (4)$$

Ω	Stream power [m^3/s]
Q	Mean annual flow [m^3/s]
I	Channel slope [-]

Stream power variations along the river network can be used as a proxy of sediment transport capacity and the dynamic behaviour of sediment erosion and deposition along the riverbank and -bed. Areas that present as local maxima of stream power have high sediment transport capacities, resulting in riverbank and -bed erosion, whereas areas of local stream power minima can be interpreted as local deposition zones,

particularly when downstream of a local erosion zone. Local maxima and minima in the stream power map were manually identified and assigned to either erosion or deposition zones. Reaches without a distinct behaviour were not classified.

3.5.3. Landscape and riverbed elevation change

The available DEMs from the years 2000 and 2015 were differenced according to Equation 5.

$$\Delta z = DEM_{2015} - DEM_{2000} \tag{5}$$

In order to represent the erosion processes along the channel, a 750 m double-sided buffer is extracted from the DEM of Difference. The mean landscape elevation change in this buffer is then used as a proxy of riverbed elevation change for comparison with the USLE and stream power calculations.

3.6. Environmental pollution and pollution transfer pathways

In order to fully capture the scope of environmental pollution derived from artisanal alluvial mining in the basin, a spatially (both over the basin and within different environmental compartments) and temporally (season-to-season) distributed approach is required. Various methods were applied in this thesis to quantify existing heavy metal pollution and model pollutant transfer pathways in the basin.

3.6.1. Heavy metal pollution survey

A systematic literature review was conducted to identify relevant papers containing spatially distributed heavy metal concentration data in various environmental compartments. This data was consolidated to form a baseline heavy metal pollution assessment and to build a foundation for analyzing spatial and temporal patterns. Where possible, statistical analyses by sub-basin, season and compartment, and a comparison to WHO water and sediment concentration limits for heavy metals were conducted. The compartments surface water, groundwater, sediment, suspended sediment, soil and fish were surveyed.

The keywords "Pra basin", "Ghana" and "heavy metals" were searched in the ETH Online Library. Results older than 2000 were excluded. Heavy metal concentrations with location data were recorded in a GIS database. Physico-chemical parameters of water quality such as pH as well as periphery data such as aquifer properties (depth to groundwater, aquifer type, etc.) were also gathered within the survey to aid in the answering of the research questions.

3.6.2. Risk model for surface water abstraction

Surface water abstraction sites in the basin have been facing increasing treatment costs and even operational shutdowns due to Galamsey-related pollution and turbidity [2]. For this reason, it was of interest to develop measures of risk for these locations to investigate potential relationships between pollution, mining areas and other factors. Surface water abstraction sites were listed in the IWRM Report [2]. These sites were subjected to a risk analysis correlating local pollution levels derived from the pollution survey, classified according to Table 3, and various potential risk predictors. A Pearson Correlation Analysis was conducted to determine significant predictors of heavy metal pollution at a given site, coupled with a

Student-t test to determine significance. If exact location data was not available in the pollution database, local pollution was approximated based on the nearest available measurements. Potential predictors of surface water pollution risk that were analyzed included local discharge (mean annual flow derived from the FLO1K dataset), upstream area, local slope, flow length, and the upstream land use fractions of mining, built-up/bareland, agriculture and forests, which were extracted from the land use classification for each location. The locations of the GWCL sites are visualized in the Map Appendix in Section K.

Table 3: Pollution level classification of water abstraction sites.

Level	Definition
Undetectable	Toxic heavy metals undetectable or below WHO limits across all known environmental compartments
Low	Some evidence of heavy metal pollution in individual environmental compartments, mostly below WHO limits
Moderate	Evidence of multiple heavy metals in multiple environmental compartments near or marginally above WHO limits
High	Significant pollution of multiple heavy metals in multiple environmental compartments above WHO limits

3.6.3. Overview of potential pollutants and pollution pathways

Determining the dominant pollutant transfer pathways in the basin is key to deriving targeted management and remediation strategies. Figure 2 visualizes potential pollutant transport and storage mechanisms related to alluvial mining. For the purpose of this project, primary transport processes are defined as transport processes that do not involve intermittent storage mechanisms and therefore should not cause distinguishable temporal delays. Secondary transport processes take place following intermittent storage, potentially altering the temporal distribution of pollutant concentrations in the basin. Primary transport processes include surface and subsurface flows over surfaces from mining pits, direct infiltration of pit waters into groundwater and transport within the aquifer, aquifer recharge from polluted surface waters, floodplain inundation, transport via groundwater flow, and wind transport. Secondary storage and transport processes include soil deposition and fixing, storage within fluvial sediment, and resulting remobilization from high flows into surface water and onto floodplains, and soil washout from precipitation, high groundwater levels, or inundation. Within this project, transport processes and storage mechanisms were assessed using a diverse set of methods and literature data.

3.6.4. Pollutant routing algorithm to assess surface and sub-surface flows

Surface and sub-surface flows from mining pits can contaminate underlying terrain. The potential magnitude of these flows was assessed using a tailored pollutant routing algorithm created specifically for this thesis. The algorithm is derived from the commonly applied D8 flow routing algorithm and uses the DEM and a pollution source raster to model potential contamination of the landscape. This concept was adapted from previous applications in large-scale industrial mining that utilized the D8 algorithm [43, 44] to prioritize sampling control locations. The implementation of the algorithm within this thesis distributes flow along all pixels downstream of a given point, instead of only to the downstream pixel with the steepest slope, allowing for a worst-case assessment of potentially contaminated area. The algorithm was implemented in MATLAB. The pollutant source layer was derived from the land use classification, where pixels classified as mining sites are assigned an initial pollutant potential of 1, and all other pixels an initial pollutant potential of 0. The initial pollutant source matrix was then scaled up to match the

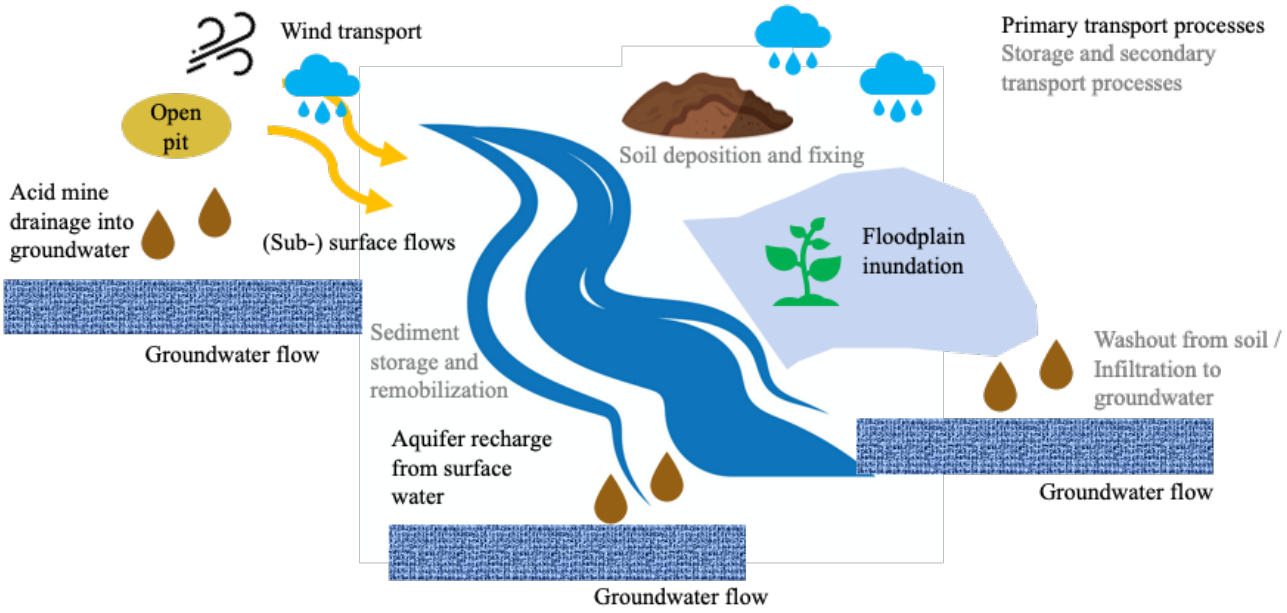

Figure 2: Potential pollutant transport pathways and storage mechanisms.

DEM resolution of 30 m. No decay or sorption was taken into account. The algorithm was constructed as follows (see Figure 3 for visualization):

1. The inputs (30 m DEM, upscaled 30 m pollutant source matrix) of the algorithm are loaded into the program.
2. For each cell, the slope to all adjacent cells is computed based on the DEM.
3. Adjacent cells with upward slopes from the current cell are assigned a flow weight of zero (flow cannot be routed uphill). All other adjacent cells are assigned a flow weight partitioned according to slope steepness. In total, each cell can distribute a sum flow of 1 to adjacent cells.
4. The flow into each adjacent cell is loaded into 8 matrices, assigned according to a cardinal direction (N, NE, E, SE, S, SW, W, NW).
5. The directional matrices are multiplied with the initial pollutant source matrix, to yield the flow routing to each cell. Cells with an initial pollutant potential of 1 are set to remain 1 during the simulation for numerical stability.
6. The inflow of each cell based on the flow directions of the adjacent cells is computed according to Equation 6.
7. The inflow matrix computed in step 5 is set as the new pollutant source matrix. Steps 4-6 are repeated for n iterations. The iteration number n determines the simulation length of the flow distance based on the raster resolution, e.g. 100 iterations at a raster resolution of 30 m models potential contamination via surface and sub-surface flows over a distance of 100x30m (3km).

The algorithm is provided in Appendix J.

$$Inflow = E_{i,j-1} + SE_{i-1,j-1} + S_{i-1,j} + SW_{i-1,j+1} + W_{i,j+1} + NW_{i+1,j+1} + N_{i+1,j} + NE_{i+1,j-1} \quad (6)$$

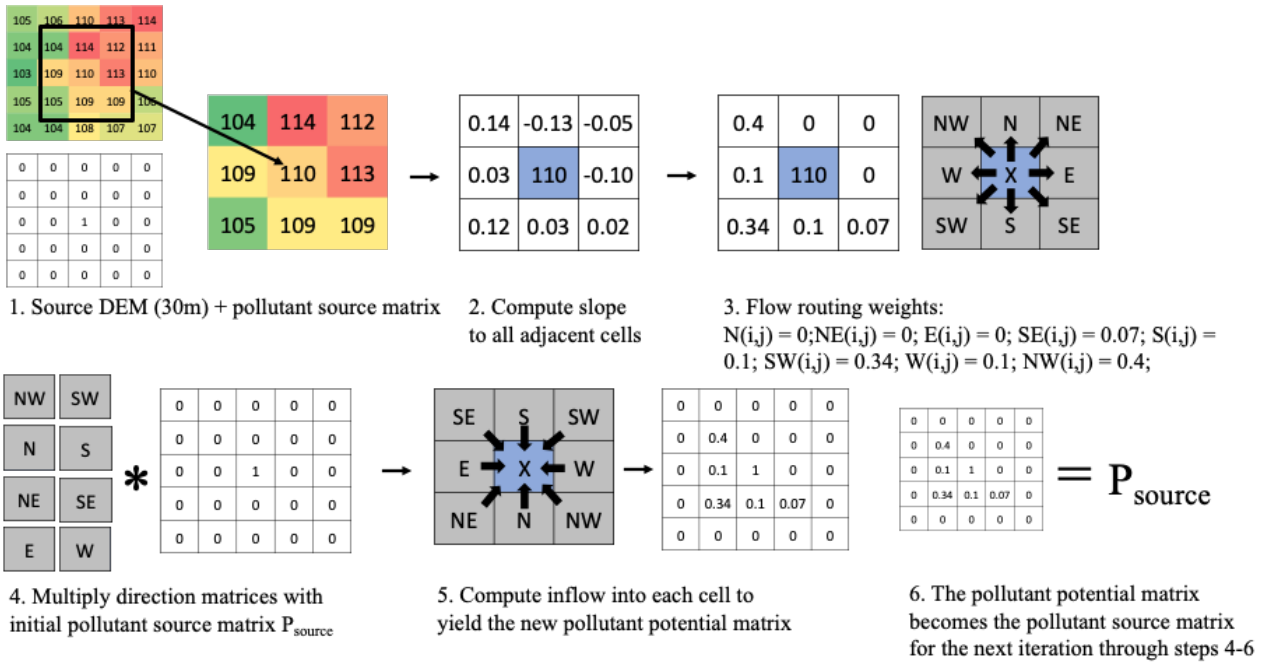

Figure 3: Visualization of the pollutant routing algorithm for pollution contamination tracking via surface and sub-surface flows.

3.6.5. Floodplain inundation modelling

Rivers can transport mining-related pollutants over wide distances in both surface water and sediment. During the rainy season, rivers in the Pra basin are known to inundate large areas, potentially leaching toxic heavy metals into soils and groundwater. In order to establish regional differences in inundation risk, floodplain inundation is modelled in HEC-RAS using the 2000 DEM and Gumbel frequency flow curves derived from annual maximum mean monthly discharges of the maximum FLO1K dataset. Five case study regions were selected to represent different regions in the basin (see Appendix M for locations):

- Twifo Praso in the Lower Pra reach
- Assin Praso in the Middle Pra reach
- Dunkwa in the lower Offin reach
- Tontokrom in the upper Offin reach
- Osino in the upper Birim reach

The following approach was followed to model frequency floods at 1, 2, 5, 10, 15, 20 and 50 year return periods, generated according to the method outlined in Section 3.6.6:

1. Extraction of the upstream basins at the given case study locations using ArcGIS Spatial Analyst;
2. Generation of the terrain in HEC-RAS using the SRTM 30m DEM;
3. Creation of a 2D computational grid at 200m resolution in HEC-RAS with grid refinement along channels;
4. Setting of boundary conditions (BC):
   - Internal BC: Flow hydrograph as the quasi-steady flow at a given return period
   - External BC: Energy slope at outlet approximated by local channel slope ("normal depth" option in HEC-RAS)
   - Manning's roughness coefficient = 0.035 to model natural channels and floodplains [45];

5. The model is run over a simulation duration of 5 days;
6. Generation of the output maximum inundation maps and retrieval of statistics on maximum inundation area and longitudinal expansion.

3.6.6. Computation of Gumbel frequency curves of discharge based on max. FLO1K

The maximum FLO1K dataset provides annual maximum mean monthly discharge values simulated for the years 1960-2015 [32]. These values were converted to Gumbel frequency curves by extracting the required data at the case study locations and computing their frequency distribution using the procedure outlined by the Consortium of Universities for the Advancement of Hydrologic Sciences [46].

3.6.7. Generalization of floodplain inundation risk factors

The floodplain inundation risk characterization was assessed using the comparative value "mean channel width" W_{mean}, computed as the quotient of maximum inundation area and the longitudinal floodwave expansion along the channel. W_{mean} was calculated for each case study at each return period. In order to assess risk without requiring floodplain modelling, which is computationally intensive and requires expert handling, W_{mean} was characterized using two indexes of floodplain inundation behaviour based on terrain and hydrology:

- Channel Terrain Steepness (CTS): CTS was computed as the standard deviation of the DEM in a 750m double-sided buffer of the river network. The CTS measures surface roughness and distinguishes deeply incised valleys with minimal floodplain behaviour from flat plains where wide inundation can be expected.
- Return period of channel capacity exceedance (CCR): Extracted from the HEC-RAS model results as the return period at which backwater effects first occur. This index could also be assessed at a given location by estimating bathymetry or by reviewing previous flood behaviour.

Using the CTS and CCR indexes and the results of the case studies, a risk matrix was created to enable a semi-quantitative risk assessment of floodplain inundation risk in a given region within the basin.

3.6.8. Groundwater-related pathways, wind transport and intermittent storage processes

Groundwater-related processes were analyzed through the results of the pollution survey as well as through a literature review of local aquifer properties. No ambient air concentration values for heavy metals were available to this project, therefore wind transport was excluded from the analysis. The potential for intermittent storage processes was analyzed using the outcome of the pollution survey, since storage processes can be determined based on temporal differences in contamination.

4. Results

The following sections outline the results of this thesis. Maps are provided in Map Appendices 1 to M and the Web-GIS. Raw data is provided within the Digital Appendix (see Appendix A for relevant links to the Web-GIS and the Digital Appendix).

4.1. The mining life cycle

Figure 4 visualizes various stages in the mining process via an example in the upper Birim basin near Akyem Mampong. In 2008 (Figure 4a), the area was covered by dense forests, wetlands, individual crop fields and a natural river run. By 2014 (Figure 4b), the river had been dredged to approx. 1 km in width and the resulting mining field housed hundreds of open mining pits filled with highly turbid waters. Aging of the mining pits that are no longer cultivated is evident based on their discolouration from muddy and turbid to dark green, which likely occurs due to to sedimentation and potentially eutrophication. In 2018 (Figure 4c), these pits lie mostly abandoned based on their colour, and have persisted in the environment. Some vegetation is returning on the bareland. However, in 2020 (Figure 4d), Sentinel-2 imagery showed multiple dark patches of land in the area that could be evidence of vegetation die-off due to heavy metal toxicity.

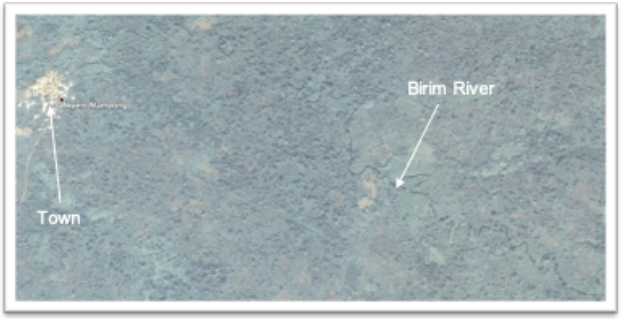

(a) 04.01.2008 Google Earth – Dense forests, wetlands and cropland around Akyem Mampong. No evidence of mining.

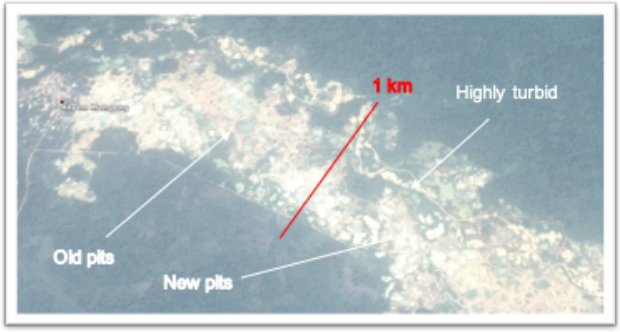

(b) 26.12.2014 Google Earth – Widespread riverbed extraction, dredging, open pit mining, deforestation.

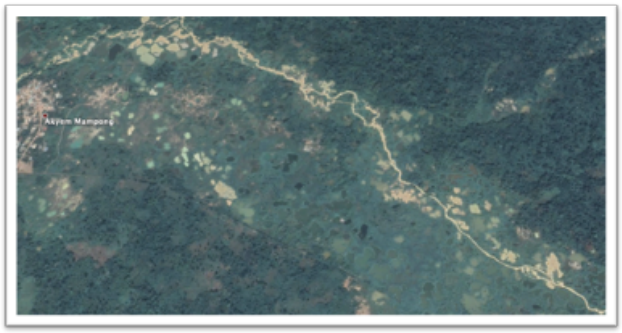

(c) 09.12.2018 Google Earth – Pits eutrophied, sedimentation evident, mining site mostly abandoned.

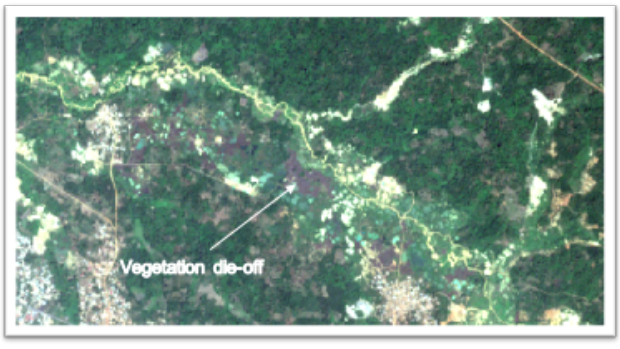

(d) 02.01.2020 Sentinel 2 True Colour Image – Potential vegetation die-off evident.

Figure 4: The mining life cycle based on a case study near Akyem Mampong in the upper Birim reach.

4.2. Land Use

4.2.1. Land use in the Pra basin

The results of the classification are listed in Table 4. The land use map is visualized in Map Appendix B. Seven distinct land use classes were distinguished in the output of the classification based on ground-truth verification and comparison to existing studies [47] (see Appendix C for an example). Rivers downstream of mining sites were classified as mining sites by the algorithm due to their highly turbid nature. Wrongly classified areas under cloud cover were manually corrected in post-processing. The Pra river delta was misclassified as a mining area due to the high moisture content in surrounding soils, and was also corrected in post-processing. Corrected classifications are included as a land use class as "Corrected cover" (CO). No separation could be achieved for built-up and bareland areas due to their similarity in spectral signature. The spectral signatures of individual land use classes for each Sentinel-2 band are visualized in Appendix E. A comparison of the NDVI and MNDWI indexes by land use class is shown in Appendix F. In total, 221 km^2 of the Pra basin are covered in mining pits. Based on a visual estimate, at least an equal amount of bareland and/or dry cropland area can be attributed to the mining class, resulting in an estimate of 2% total land use of alluvial mining.

Table 4: Land use classification of the Pra basin derived using unsupervised Iso Cluster Classification.

Land Use Class	Short ID	Description	Area [km^2]	Fraction
Closed canopy	CC	Closed canopy forests	2690	11.63%
Open canopy	OC	Open canopy forests, dense agricultural orchards	4953	21.41%
Agriculture 1	AW	Cropland with high water content (e.g. active cropland), patches of grassland and remaining low vegetation with high water content	9466	40.93%
Agriculture 2	AD	Cropland with low water content, dry grassland, cropland following slash-and-burn treatments, remaining low vegetation with low water content	3727	16.11%
Mining - Open pits	M	Alluvial mining pits filled with water, and rivers downstream of mining sites	221	0.95%
Built-up and bareland	B	Settlements, natural bareland, roads, mining-related bareland	1940	8.39%
Water	W	Water cover (primarily Lake Bosomtwi and reservoir lakes)	53	0.23%
Corrected cover	CO	Manually corrected areas	79	0.34%
Total			**23129**	

The land use classification highlighted two hotspots with a high density of open pit mining: The middle reaches of the Offin sub-basin and the Oda and Jimi tributaries, spanning approx. 140 km along the main Offin river from Kyekyewere to Bonteso, and the upper reach of the Birim sub-basin over a span of approx. 85 km between Kyebi and Subi. In these sections, the natural channel has been entirely dredged up to a lateral width of 4 km. Beyond the densely dredged mining reaches of the mid-Offin and the upper Birim, all main tributaries show evidence of sparse alluvial mining activity along the river channels in the upper reaches, and minor mining activity in the lower Pra basin.

4.2.2. Classification accuracy and confusion matrix

The results of the land use classification accuracy assessment are summarized in Table 5.

Table 5: Confusion matrix of the land use classification accuracy assessment based on random sampling.

LU Class	CC	OC	AW	AD	M	B	W	Sens.
CC	190	19	1	0	0	0	0	**90.5%**
OC	3	175	18	0	0	0	0	**89.3%**
AW	0	17	159	8	3	0	0	**85.0%**
AD	0	0	17	173	0	17	0	**83.6%**
M	0	1	1	2	208	3	0	**96.7%**
B	0	0	2	6	0	232	0	**96.7%**
W	0	0	1	0	0	0	93	**98.9%**
Spec.	**98.4%**	**82.5%**	**79.9%**	**91.5%**	**98.6%**	**92.1%**	**100%**	

4.2.3. Land use in proximity of rivers

Figure 5 visualizes the fraction of land use per class in various distances to the river network normalized by the total fraction, and shows that mining occurs primarily within close proximity of the river compared to the other land use classes. Significant positive correlations with river proximity were found for the M (r=0.834, p=0.075%) and AD (r=0.894,p=0.009%) classes (see Figure 6a). Significant negative correlations with river proximity were found for the CC (r=-0.994, p=0.000%) and OC (r=-0.948, p=0.000%) classes (see Figure 6b). B (r=0.226, p=47.93%) and AW (r=0.576, p=5.024%) are insignificantly positively correlated at the 5% confidence interval (see Appendix G). Within a 1.5 km buffer of the riverbed, land use consists of 8.6% CC, 20.9% OC, 42.7% AW, 16.9% AD, 1.3% M and 9.1% B.

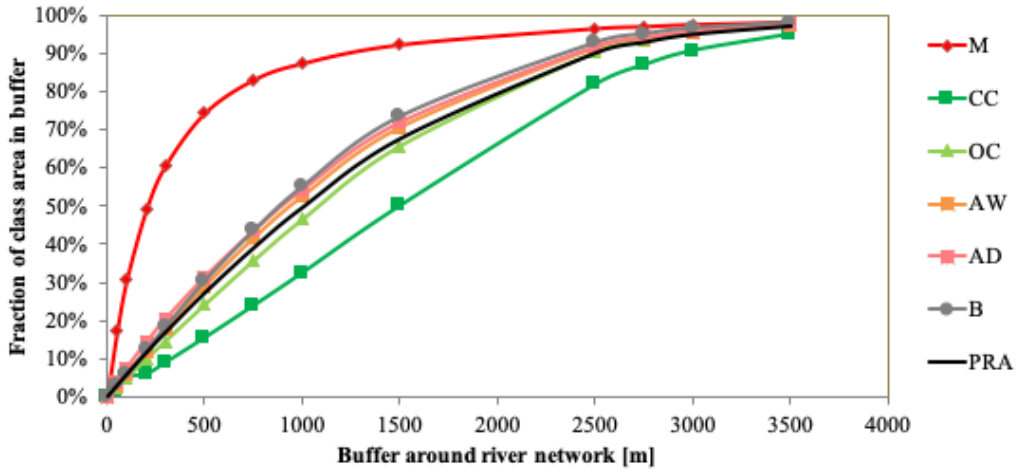

Figure 5: Fraction of total land use by class within various distances of the river network.

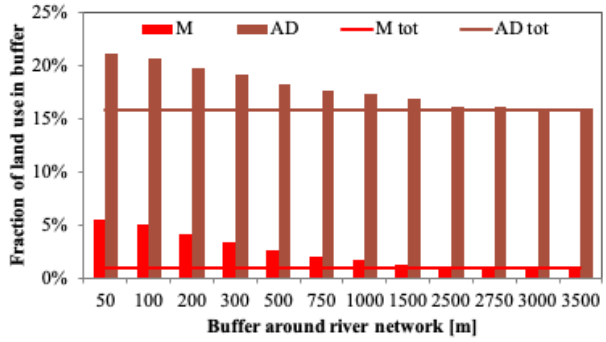

(a) Proximity analysis of the M and AD classes comparing proximity to river to fraction of land use.

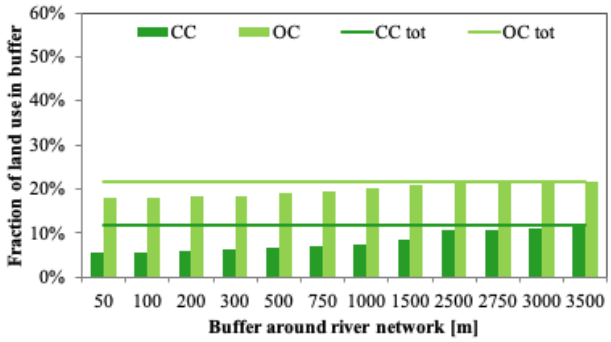

(b) Proximity analysis of the CC and OC classes comparing proximity to river to fraction of land use.

Figure 6: Proximity analysis of the land use surrounding the Pra basin river network.

4.3. Erosion and river morphology changes

4.3.1. Soil erodibility factor K

The soil erodibility factors computed according to Wischmeier and Smith [37] are listed in Table 6. All soils within the basin have a soil structure class of 2 and a profile-permeability class of 5 [41]. Soil erodibility can be considered low to moderate across the basin [48].

Table 6: Soil types, properties and erodibility factors K within the Pra basin computed according to Wischmeier and Smith. Soil structure is assumed as class 2, and profile-permeability as class 5 according to the FAO classification system. "OC" stands for organic carbon content.

Soil Type	Sand	Silt	Clay	Soil Texture	OC %	M	K
Orthic Acrisols	48.5%	15.9%	35.6%	Sandy clay loam	2.25%	1024	0.1053
Leptosols	58.9%	16.2%	24.9%	Sandy clay loam	0.97%	1217	0.1262
Nitosols	63.1%	10.3%	26.7%	Sandy clay loam	0.60%	751	0.0955
Ferric Acrisols	49.9%	7.3%	42.7%	Sandy clay loam	1.23%	418	0.0720
Xanthic Ferralsols	57.1%	13.7%	29.3%	Sandy clay loam	0.91%	966	0.1089

4.3.2. Annual soil loss according to the USLE

Total annual soil loss derived using the Universal Soil Loss Equation is summarized in Table 7. The annual soil loss map is listed in Map Appendix C. Overall, the USLE estimates that 96.8% of the basin experiences very low to moderately low erosion rates per year with a mean loss of 1.07 t/ha/yr. Mean annual soil loss classes were defined according to the classification system in the reference study by Adongo T. et al. [49], which analyzed soil loss in northern Ghana. Small localized patches of high erosion were predicted on the hillslopes of the Kwahu plateau in the Northeast, on the eastern edge of the Atewa range in the upper Birim reach, along the Tarkwaian formation from Lake Bosumtwi to Dunkwa, and along the channel of the heavily dredged mid-Offin.

According to the USLE, open pit mining contributes to annual soil loss by approx. 58.20 kt/a (see Table 8) if assessing only mining pits. Assuming that active mining land is 50% open pits and 50% mining-related bareland (constituting 11.38% of built-up/bareland land use), this results in a predicted annual soil loss of 99.03 kt/a due to mining, or 3.97% of total annual soil loss.

Table 7: Total annual soil loss in the Pra basin.

Erosion Class [-]	**Soil Loss [t/ha/yr]**	**Mean Soil Loss [t/ha/yr]**	**Area [%]**	**Total Soil Loss [kt/yr]**
Very Low	0-1 t/ha/yr	0.26	68.4%	372.4
Low	1-2 t/ha/yr	1.43	16.4%	499.9
Moderate Low	2-5 t/ha/yr	2.98	12.0%	762.3
Moderate	5-25 t/ha/yr	8.69	3.1%	578.9
High	25-60 t/ha/yr	33.61	0.1%	75.7
Very High	>60 t/ha/yr	79.94	0.01%	11.7

Table 8: Mean annual soil loss by land use.

Land Use Class [-]	**Area km^2**	**Mean soil loss t/ha/a**	**Total soil loss kt/a**
Closed forest	2689.85	0.02	6.48
Open forest	4953.10	0.28	140.23
Agri-wet	9466.32	1.29	1224.21
Agri-dry	3727.14	1.89	704.46
Mines	220.78	2.63	58.20
Built-up/Bare	1940.37	1.84	358.88

4.3.3. Stream power

The stream power map and the erosion and deposition zones identified based on stream power are visualized in Map Appendices H and I. The validation results of the FLO1K dataset, which were used to compute stream power, are summarized in Appendix H. Stream power was shown to be discharge-driven and even throughout the basin, increasing in the lower reaches due to the confluence of the Middle Pra and the Offin.

4.3.4. Landscape and riverbed elevation change

Landscape and riverbed elevation change from 2000-2015 are visualized in Map Appendix D. The riverbed elevation change shows significant erosion of all main channels. The mean elevation change of the basin is -0.87 m. Assuming a soil density of 1.3 t/m^3 and a porosity of 0.3, this means the basin experiences a net erosion rate of approx. 1200 Mt/a. Table 9 summarizes the mean net elevation change per land use class from 2000 to 2015. With exception of the water class, mining areas experienced the most significant erosion. An example of erosive behaviour underlying mining sites is demonstrated in Appendix I. The computed landscape elevation change is subject to the respective accuracies and calibrations of the DEM, which are estimated at a vertical root mean square error (RMSE) of 3.53 m for the SRTM DEM and at 2.14 m for the ALOS 3D World DEM [50].

4.4. Environmental pollution and pollutant transfer pathways

4.4.1. Summary of the literature review

The ETH library database yielded 153 studies related to the keywords "Pra basin", "Ghana" and "heavy metals". Abstracts were screened for overall relevancy and presence of spatially referenced data. In total, the initial literature screen yielded 16 studies in the region that include spatially referenced data related

Table 9: Mean elevation change of the DEM of Difference from 2000 to 2015 by land use class.

Land Use [-]	**Mean Landscape Elevation Change, 2000-2015 [m]**
CC	0.705
OC	-0.373
AW	-0.936
AD	-0.921
M	-3.959
B	-0.438
W	-107.968
CO	-1.815

to open pit mining and pollution [51, 12, 3, 4, 52, 53, 7, 11, 54, 55, 56, 57, 18, 19, 58, 10]. A total of 2433 heavy metal point concentration data points across 168 locations and 12 metals (Al, As, Cd, Cr, Cu, Fe, Hg, Mn, Ni, Pb, Se, Zn) in all environmental compartments (surface water, groundwater, sediment, suspended sediment, soil, fish) were recorded, with exception of ambient air. Location, concentrations and sources were recorded in a digital database, and then uploaded to ArcGIS using unique indexes for each measurement location. The map of datapoint locations is given in Map Appendix J.

4.4.2. Heavy metal pollution from alluvial mining in the basin

High levels of heavy metal pollution are evident across every subbasin and within all environmental compartments with exception of ambient air, which was not analyzed due to a lack of data. The exceedance of all datapoints by environmental compartment is listed in Table 10 and by subbasin in Table 11. The full pollution analysis by metal, compartment and subbasin is given in Appendix L. Sections L.1 and L.2 summarize the statistics by season, subbasin, compartment and metal. Sections L.3 and L.4 visualize WHO exceedance. Due to the large size of the database, the raw data set including datapoint references is only provided within the supplementary material of this report.

Overall, surface water showed the most frequent exceedance of WHO levels, followed by soil. Suspended sediment showed the least frequent exceedance. At a subbasin level, the Middle Pra and the Offin experienced the most frequent exceedance by a wide margin. Surface water showed particularly frequent exceedance of WHO recommended limits for As, Cd, Cr, Fe, Hg, Ni and Pb (see Tables 32 and 37). Groundwater shows high levels of WHO exceedance for Hg, Pb and Se. Sediments have particularly high Al, Cd, Cr, Ni and Pb exceedance of WHO recommended limits. However, only 4.3% of sediment datapoints exceed WHO limits for Hg, despite consensus that sediment is usually a significant Hg sink [59], particularly compared to surface and groundwater. This lower exceedance is mirrored in the suspended sediment concentrations from the Birim subbasin as well.

Analysis of WHO limit exceedance by subbasin and environmental compartment (Sections L.3 and L.4) demonstrate the widespread pollution within the basin. In total, 36% of the recorded heavy metal concentrations sampled in the basin are above WHO recommended heavy metal limits. Concerningly, 82.1% of groundwater Hg measurements exceed the recommended WHO limits for drinking water. All non-exceeding Hg values in groundwater were determined in a single study of the Birim subbasin in 2010 [4]. 16.7% of the collected fish datapoints showed mean mercury levels in excess of the WHO recommended limit of 0.5 mg/kg, even far upstream of the mining sites in the Barekese reservoir (see Appendix L.5) [57, 54].

In environmental compartments where seasonal data was available (surface water, sediment and soil), distinct seasonal variance is evident (see Table 18 in Appendix 32). The majority of studies identified higher Hg levels during the wet season compared to the dry [19, 7, 23, 4] in both surface water, soil and groundwater. However, not all data analyzed in these respective studies was available at seasonal scale to enter into the database, therefore this is not fully represented in the compiled data. A similar trend was also shown for Ni and Pb in surface waters and Cd in sediment (see Table 18 in the Appendix). Contrastingly, Hg concentrations in sediment were higher in the dry season compared to the wet season (see Figure 33 in the Appendix). Hg concentrations in suspended sediment were not given at seasonal resolution, but showed very high variance in location (see Table 18 in Appendix 32).

Table 10: Heavy metal pollution data points (each metal counted separately) sourced in the literature review by environmental compartment and WHO limit exceedance across 168 locations in the basin. Additional detail is available in Appendix L.3. The corresponding WHO limits are listed in Appendix D. Fish not shown due to small sample size.

	# Data points by season				WHO Rec. Limits	
Compartment	**Wet**	**Dry**	**Unspec.**	**Total**	**% Above**	**% Below**
Sediment	256	255	198	709	33%	67%
Groundwater	6	6	556	568	27%	73%
Surface water	324	324	228	876	46%	54%
Soil	21	21	5	47	40%	60%
Suspended sediment	0	0	176	176	23%	77%
Total				**2376**		

Table 11: Heavy metal pollution data points (each metal counted separately) sourced in the literature review by subbasin and WHO limit exceedance across 168 locations in the basin. Additional detail is available in Appendix L.4. The corresponding WHO limits are listed in Appendix D. SW = Surface Water; GW = Groundwater; SED = Sediment; SSED = Suspended Sediment; SO = Soil; Fish not shown due to small sample size.

Subbasin	# Data points by compartment						WHO Rec. Limits	
	SW	**GW**	**SED**	**SSED**	**SO**	**Total**	**% Above**	**% Below**
Lower Pra	212	390	163	0	31	796	38.9%	61.06%
Middle Pra	134	80	119	0	7	340	51.5%	48.53%
Upper Pra	28	40	27	0	1	96	26.0%	73.96%
Offin	276	22	194	0	8	500	48.4%	51.60%
Birim	202	26	200	168	0	596	14.3%	85.74%

4.4.3. Risk model for water supply

The locations of known GWCL surface water abstraction plants, their pollution class and the statistics of the potential risk predictors are listed in Table 12.

Table 12: GWCL surface water abstraction sites and potential predictor statistics. Area refers to upstream area. Q_{mean} refers to mean annual flow extracted from the mean FLO1K dataset. Class refers to pollution level according to Table 3. M, B, A and C refer to fractions of upstream land use. M = Mining - Open pits; B = Built-up/Bareland, A = Agriculture (combined class of AW and AD), C = Canopy (combined class of CC and OC). Flow Length refers to the normalized flow length from upstream normalized to Daboase as the basin outlet.

Site	**Subbasin**	**Area**	Q_{mean}	**Class**	**Slope**	**M**	**B**	**A**	**C**	**Flow Length**
[-]	[-]	[km^2]	[m^3/s]	[-]	[%]	[%]	[%]	[%]	[%]	[-]
Owabi	Offin	65.93	1.24	Low	9.0	0.1%	90.5%	8.3%	0.3%	0.04
Barekese	Offin	28.47	8.43	Low	8.3	0.1%	47.8%	49.1%	1.6%	0.03
Kibi	Birim	50.44	1.44	High	1.8	0.5%	4.3%	29.5%	65.7%	0.03
Osenase	Birim	33.24	1.21	Low	2.4	0.1%	1.1%	39.0%	59.8%	0.04
Osino	Birim	304.87	4.79	High	0.6	1.2%	4.8%	49.2%	44.8%	0.11
Bunso	Birim	146.48	2.88	High	1.8	0.8%	4.3%	45.4%	49.5%	0.09
Obuasi	Jimi	277.59	4.03	Low	4.9	0.1%	7.4%	51.8%	40.8%	0.11
Konongo	Anum	85.33	1.66	Mod,	1.8	0.3%	18.4%	57.5%	23.9%	0.08
Anyinam	Birim	413.24	6.86	Mod.	0.8	1.8%	6.4%	49.4%	42.4%	0.14
Kwabeng	Birim	557.97	7.82	Mod.	4.6	1.9%	6.9%	50.6%	40.7%	0.15
Akim Oda	Birim	3176.30	32.45	Mod.	0.6	0.7%	3.0%	47.6%	48.7%	0.37
Ofoase	Pra	4124.20	44.32	Low	0.0	0.2%	4.1%	49.7%	44.7%	0.29
Dunkwa	Offin	7473.80	68.87	High	0.0	2.1%	14.5%	67.0%	16.2%	0.57
Twifo-Praso	Pra	19774.62	184.24	High	3.8	1.1%	7.5%	57.4%	33.6%	0.82
Daboase	Pra	21649.91	204.63	High	0.0	1.1%	7.0%	56.9%	34.7%	1

The results of the Pearson Correlation Analysis are summarized in Table 13. Local slope and upstream fraction of mining area were shown to be significant predictors of local pollution levels at the 95% confidence interval. Pollution levels increase with lower slopes and larger fractions of upstream mining areas.

Table 13: Results of the Pearson Correlation Analysis and Student-t test on local pollution levels comparing potential predictors of pollution.

	Area	**Flow**	**Slope**	**M**	**B**	**A**	**C**	**Flow Length**
r-value	0.463	0.449	-0.536	0.623	-0.421	0.356	0.260	0.488
p-value	0.082	0.093	0.039	0.013	0.118	0.193	0.349	0.065

4.4.4. Surface and sub-surface flow

The generated potential surface and sub-surface flow contamination map is visualized in Map Appendix L. The map shows only marginal potential of contamination of the surface before pollutants reach the rivers. Appendix K demonstrates an example of the algorithm inputs and resulting outputs.

4.4.5. Floodplain inundation modelling

Figure 7 visualizes W_{mean} computed as the quotient of maximum inundated area and longtitudinal expansion for each case study and simulated return period. Mean channel width is a measure of lateral floodplain expansion. Risk characterizations were developed based on W_{mean} for each case study region.

All simulation output data is listed in Appendix M.

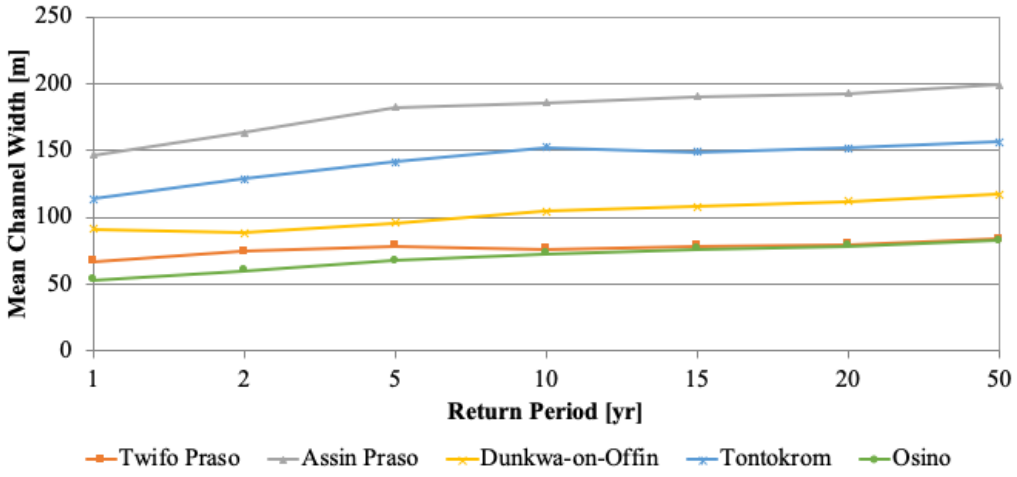

Figure 7: Mean channel width W_{mean} as a measure of lateral floodplain expansion

CTS is visualized in Map Appendix M. Table 14 summarizes the CTS, CCR and related statistics extracted from the simulation to predict risk characterization. The floodplain risk model, which is shown in Figure 8, was then developed based on the statistics of the simulation as well as the visual analysis of the inundation boundaries.

Table 14: Statistics of the 2D Floodplain Model in HEC-RAS.

Case Study	Upstream area [km^2]	CCR [yr]	Q at CCR [m^3/s]	CTS [m]	Risk Class [-]
Twifo Praso	7829	10	603	10	Low
Assin Praso	3847	5	240	6	High
Dunkwa	16212	1	82	10	Moderate
Tontokrom	8383	15	165	8	Moderate
Birim	232	50	>20.7	7	Low

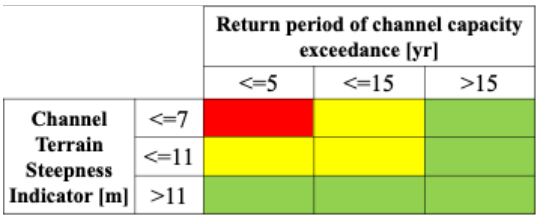

Figure 8: Risk matrix determined through the 2D floodplain inundation model of 5 case studies in the basin. CCR = Return period of channel capacity exceedance; CTS = Channel Terrain Steepness.

4.4.6. Groundwater-related transport processes

The potential of pollution transfer within the aquifer and via surface water recharge into the aquifer was investigated using outcomes of the pollution survey as well as information from literature. The pollution

survey identified high levels of overall pollution within groundwater (see Figure 34 in Appendix L.3), with high variance (see Table 18 in Appendix L.1) between locations. As previously mentioned in Section 4.4.2, Hg concentrations found in literature are usually higher during the wet season with an overall exceedance of Hg WHO recommended levels of 82.1% in groundwater, while 27% of overall groundwater datapoints for all metals exceed recommended WHO limits for drinking water, indicating a high degree of exposure to contamination risk.

The Pra basin aquifer is underlain by the Tarkwaian and Birimian groups, which comprise metavolcanic and metasedimentary rocks and weakly foliated volcanic rocks and granitoids, as well as the Dixcove granite complex [60]. The aquifer does not possess primary porosity sufficient for groundwater flow [23, 61, 60]. Permeable sections are discrete and irregular along fractures and weathered sections, and permeable aquifer material exists only in small pockets of alluvial sediments along channels [23]. This implies that transport within the aquifer over large distances is unlikely. However, high pollutant concentrations may be transferable from mines to boreholes that are located along the same fracture in the aquifer. Drainage of polluted pit waters into the groundwater aquifer may be impaired due to the formation of a clayey isolating top-layer within the pits resulting from comminution processes of the fluvial sediment, which has been demonstrated in various studies [62, 47]. The non-permeable Tarkwaian belt reaches from Lake Bosumtwi in the upper reaches of the basin through Upper Pra and Offin subbasins [24], likely precluding polluted aquifer waters of the Offin mining stretches from being transferred further downstream to the Middle and Lower Pra reaches at meaningful concentrations. Hydrochemical appraisal of groundwater-rock interactions in the basin indicated that a majority of groundwaters were chemically similar to surface waters, undersaturated with key geogenic minerals present in the basin, and of low buffering capacity, indicating small residence times and small transport distances in the aquifer [23, 61]. While the low buffering capacity makes groundwater particularly vulnerable to acid mine drainage [14], this confirms that aquifer transport does not explain the widespread groundwater pollution in the basin. Contrastingly, the surface-water-typology of most groundwaters in the basin points heavily to river-driven recharge processes along the channel. This is compounded by very low groundwater levels in many regions of the basin [63], particularly in the Middle Pra reach. It is therefore inevitable that the polluted river will lose water to the aquifer, introducing high concentrations of pollutants into groundwater even far away from mining sites.

5. Discussion

5.1. Land use and geomorphology

Overall, the proposed method to streamline mine detection through unsupervised Iso Cluster Classification using a false colour composite MNDWI-derived image stack was shown to be relatively low effort and highly accurate (see Appendix C). The false colour composite image of Sentinel-2 bands 2, 3 and 12 enabled the quick visual identification of mining sites, which proved to be a strength as an input into unsupervised classification. Significantly, the image allowed for the classification of mining pits that were hardly visible on true colour composite images due to their discolouration, so both new and old pits can be detected with similar accuracy. It is highly recommended that this method of classification be used to monitor the emergence of new mining fields, as well as the progression of existing mining fields.

Seven land use classes were identified: Closed canopy forests, open canopy forests, high-water-content agriculture, low-water-content agriculture, open pit mines, built-up and bareland, and water. The basin is dominated by cropland. Closed canopy forests are nearly exclusively limited to the forest reserves, although these were shown to be an effective protective mechanism.

The classification method showed excellent class separation of the mining areas, with 96.7% of the sampled mines correctly classified. The minor loss in classification specificity is due to the highly turbid waters in smaller tributaries flowing through Kumasi, which were wrongly classified as mining pits due to their similar spectral signature. The overall accuracy of the classification is 91.2%. Losses in the accuracy in the CC and OC classes, as well as the AW and AD classes, are due to the high degree of class separation. Combining the canopy classes and the cropland classes would increase overall accuracy to 94.7%. Since the basin is covered by 7 images and these were sourced at different dates, there are minor differences in land use classification at the overlapping edges of the images, likely due to differing water contents at the time of capture (such as due to smaller rainfall events). Due to this, the time of capture and prior rainfall behaviour are sensitive parameters for the classification of the agricultural and canopy classes, as these have the smallest degree of separation by signature amongst each other (see Appendix E).

The land use classification produced results that coincide well with previous classifications by Awotwi A. et al. (2018) [1] using Landsat-8 images, confirming that Sentinel-2 imagery produces similar results to Landsat-based classifications. In comparison to Awotwi A. et al., who classified images from the year 2016 using supervised classification, the current classification showed reduced forest cover (-5.68% for CC, -14.73% for OC), an increase in overall cropland (+18.98% for AW and AD) and an increase for built-up/bareland (+2.22% for B). It is not clear to what magnitude these land use changes are due to actual land use conversions vs. different classification systems. The Landsat study did not separate agricultural classes, while the current classification identified two distinct agricultural classes based on water content due to the MNDWI-derived image stack. This means that the AW class also includes high-water-content orchards and dense crops such as cocoa, which could appear as open canopy forests in images when using a lower resolution classification. Awotwi A. et al. classified mining areas in 2% of the basin, which coincides with the approximated total mining area when considering mining-related bareland. Overall, this does not indicate a significant increase in mining areas between 2016 and 2018. Nevertheless, a true land use change assessment should use the same methodology to assess all time periods.

The water-content-based classification has several other potential uses, primarily in agriculture, that could be exploited in the future. Potential uses include investigating crop vulnerability to drought, soil water content, and investigating the performance of irrigation systems, particularly if coupled with on-site analyses [64].

The proximity analysis of land use in relation to rivers identified several trends. Over 90% of mines occur within a distance of 1.5 km to a river. Overall, open pits and cropland with low water content (M and AD) significantly correlate with river proximity. The AD class represents dry vegetation, meaning this could be a result of vegetation clearing processes on land intended to be used for open pit mining. A similar trend would have been expected for built-up and bareland, however the lack of a significant correlation can be explained by the large built-up area of Kumasi, which skews the results. The significant negative correlation of open and closed canopy forests is in an indicator of deforestation. While this alone does not directly establish a causal link to mining, Awotwi A. et al. (2018) [1] determined an annual mining area growth rate of 12.35% since 2004, which occurred largely at the expense of forests and cropland.

Looking forward, it would be beneficial to separate built-up and bareland areas due to the role of bareland in the mining process, which can be considered an early warning indicator of potential mining activity when near a river. Separation using Iso Cluster Classification could be attempted using a pattern layer such as image standard-deviation, as built-up lands have a higher degree of noise compared to bareland. Coupled with the 5-day flyover period of Sentinel-2, the detection method could be used to take proactive action to prevent Galamsey.

Uncertainties regarding the land use classification occur through user error or within the satellite imagery. The Iso Cluster Classification output must be manually assigned to the desired classes and aggregated in post-processing. This can introduce misclassification due to false assignment. Additionally, ground-truth verification must be conducted with care. Cloud cover presented a key challenge in accessing accurate satellite imagery. The region is prone to a high degree of cloud cover particularly during the wet season, which creates difficulty in accessing full coverage satellite images year-round. For this study, images with adequate cloud cover ($<$1%) could only be sourced in the dry season over a time period of December 2018 to January 2020. This can introduce time-scale errors in the classification. Additionally, it does not allow us to utilize the 5-day resolution of Sentinel-2 data to its full extent.

The magnitude of mining within the basin is worrying due to its highly disruptive impacts on the environment. In many sections of the mining hotspots of the Offin and the Birim, natural channel flow can no longer be detected. The riverbeds and -banks have been completely destroyed by dredging. The mining process also eliminates important nutrient and flood buffering zones alongside the riverbanks, which can have devastating effects. Discharge changes in relation to land use changes have been previously investigated in the basin [62, 47, 65], which showed an increase in surface runoff and decreased baseflow with increasing mining areas. Mining areas often form "clayey", sealed top layers that are impervious and therefore prevent infiltration, while the removal of vegetation impacts soil, which can further worsen this issue [47]. This leads to lower overall soil moisture and can decrease ecosystem resilience to long periods of drought, as well as increase flood risk during extreme rain events. In light of climate change, this behaviour can be expected to increase, additionally putting stress on the environment. Most notably, the analysis of a mining field over time as shown in Section 4.1 shows that large mining fields experience little to no attenuation over many years, and are highly persistent in the environment.

5.2. Erosion and river morphology changes

Predicted annual soil loss in the basin can be considered low at 1.07 t/ha/yr, due to low soil erodibility, low slopes and good vegetative protective cover [49]. This coincides with similar USLE-based studies of the basin [17]. However, specific suspended sediment yield at the Pra basin outlet is approx. 3.29 t/ha/yr [16]. Specific suspended sediment yield usually composed 10-30% of gross erosion [66, 67, 68], inferring that actual erosion is 10-30 times higher than predicted by the USLE. This is also supported by findings

that suspended sediment concentration in the basin are not correlated to rainfall, and that over 60% of suspended sediment consists of bank material [16]. The lack of prediction accuracy in the basin and these underlying findings point to gully and channel erosion being the dominant erosive processes in the basin. These processes are also exacerbated by mining in and around the riverbeds. The USLE is not equipped to model gully and channel erosion [69]. For this reason, it is not recommended to continue assessing erosion in the basin purely using the USLE, which was historic practice [16]. A channel-based model that can accurately capture sediment entrainment due to alluvial mining is required to predict erosion in the river channels. However, this requires higher resolution discharge and sediment data, as well as more complex modelling.

Stream power showed a steady increase towards the outlet, which is to be expected due to the basin's low slopes. Stream power in the Pra basin can be considered discharge-driven, significantly increasing following the confluences of the Pra with the Birim and Offin in the centre of the basin. High slopes are only present in the Northern reaches, where discharges are comparably small. This corroborates findings that indicate bank and bed erosion increase downstream [16], primarily due to increased stream energy. Actual landscape and riverbed elevation change based on DEM differencing within the period of 2000 to 2015 show significant erosion of both the landscape and of the riverbeds, with a mean landscape elevation change of -0.87 m. Computed to mass of soil lost, the elevation change over the basin corresponds to a net soil loss approx. 18-55 times larger than the specific suspended sediment yield. This figure is highly uncertain due to the accuracies of the DEMs, and should therefore only be approached with caution.

All major tributaries experienced a net elevation loss, of which the Upper Pra, the Middle Birim and the Lower Pra experienced the most significant channel erosion rates (see Map Appendix M). The computed mean elevation change by land use class confirms that mining areas experienced the second-largest mean net elevation loss of -3.96 m, second only to the water class, which experienced a mean net elevation loss of -108.00 m (see Table 9). While all water bodies in the basin did show a decrease in size, the drastic elevation change can be assumed to be erroneous due to the different calibrations and accuracies of the DEMs. While the RMSE of the DEMs are only in the range of a couple meters [50], the SRTM DEM has been shown to be highly inaccurate with increasing slope and elevation [70]. This could have a large impact on the gross mean elevation change of the water class, particularly in the steep areas surrounding Lake Bosomtwi. Therefore, the water measure of elevation change can not be considered realistic.

A visual analysis of the landscape elevation change also showed significant erosion in locations where open pit mining is practised, confirming assumptions that open pit mining disrupts natural morphological processes by artificially increasing erosion. The relative comparison of elevation change by land use class confirms expectations despite potentially incorporating some error due to the magnitude of difference in elevation changes by land use and their adherence to expectations. Closed canopy forests were shown to provide the best protection from erosion and were the only land use class to experience a mean net elevation gain. Open canopy forests experienced the lowest rates of mean net soil loss, followed closely by built-up and bareland. Interestingly, both wet and dry cropland had nearly double the rate of mean net soil loss as built-up and bareland. This could be due to protective measures being taken to protect infrastructure in settlements, or due to the uplanding of bareland surrounding mines on areas that serve as sediment dumping grounds. This also supports the implementation of agricultural practices that integrate agroforestry to preserve soil quality and quantity. Overall, the actual landscape and riverbed elevation changes point to moderate levels of erosion of cropland, and severe channel erosion due to mining.

The USLE does not correlate with actual elevation change with exception of the high predicted soil loss on steep slopes in the basin. Riverbed elevation change showed consistency with stream power, however the manually assigned erosion and deposition zones did not correspond to areas of actual erosion or deposition.

This can be explained by the dynamic and inherently unstable nature of the river, which will continuously shift sediment and attempt to again reach equilibrium. This natural dynamic can be significantly altered by disruptive processes such as pit dredging [71]. Sediment transport is therefore unlikely to be captured by a single figure that only combines slope and discharge. Nevertheless, the outlined zones could serve as an indicator of areas that are particularly susceptible to either erosion and deposition, and this should be verified on-site in the future. Additionally, sediment transport is commonly influenced primarily by extreme discharge events, which would indicate that the maximum FLO1K dataset or, even better, actual flood peak data, would provide a more accurate picture of erosion and deposition zones along the channel. This requires higher resolution discharge data.

The potential impacts of erosive processes due to mining can have large impacts on ecosystems, communities and the local economy. Erosive processes have already impacted several surface water abstraction sites of the GWCL in the basin, causing shut-downs and rising treatment costs [2], and can also impact infrastructure such as bridges. Given these results, it is critical that a more accurate and higher resolution sediment transport model be developed for the Pra basin to prioritize where immediate measures are required to stabilize the channels and prevent further damage.

5.3. Environmental pollution survey

The collected data provides a previously nonexistent comprehensive view of mining-related heavy metal pollution in the basin. Heavy metal pollution is evident at levels that can negatively impact human and ecosystem health, and that can not be explained by other anthropogenic processes. Areas far upstream of mining sites were shown to have lower levels of pollution, indicating that the natural background of heavy metals in the basin is far lower than is usually observed in regions affected by mining. [3, 4, 58] Overall, it was shown that pollution can travel far downstream and over significant distances beyond the river channel (see Appendix L). The high degree of contamination far away from mining sites, particularly in compartments previously considered isolated and unaffected by the negative impact of mining such as groundwater, indicates a high degree of mobilization and transport throughout the basin. The highest exceedance of WHO recommended limits in the Middle Pra and Offin is reasonable due to these reaches being most affected by mining in their upper reaches. The comparatively low pollution levels in the Birim reach can be explained by the low suspended sediment concentrations and low sample size, which skewed the results. Nevertheless, the Birim reach still experiences high pollution levels comparable to the other reaches. The Upper Pra is likely less contaminated due to a smaller degree of local mining. However, fish migration could carry Hg-polluted fish upstream, where it can also pose a health risk, as was seen in the fish datapoints (see Appendix L.5) [57, 54]. Significantly, the Lower Pra experiences high levels of contamination that can only be explained by pollution transfer from the upper subbasins, since mining activity is minimal in the lower reaches.

The seasonal variance implies at least some degree of intermittent storage and subsequent remobilization, as well as a non-geogenic origin, since geogenic contaminants would occur at relatively steady concentrations over the year or lower concentrations during the wet season due to dilution [**?** 11]. The elevated concentrations of some metals in the wet season in surface water, soil and groundwater indicate precipitation-driven processes. These include the washing out of highly polluted mining pits into the rivers, the remobilization of heavy metals in sediment due to high flows, and soil and groundwater contamination resulting from floodplain inundation. This is mirrored in the higher concentrations of Hg in surface water, groundwater and soil in the wet season reflected in the majority of research [19, 7, 23, 4], compared to the higher concentrations of Hg in sediment in the dry season. This could be due to increased sedimentation behaviour and lower dilution in the dry season, as well as increased mining activity. The suspended sediment con-

centration values of the Birim river [12] showed very high variance at low temporal scales due to upstream ore processing, particularly compared to surface and groundwaters, which indicates that this compartment is particularly susceptible to inputs from mining over short time periods. This could translate to similar behaviour for sediments further downstream once the suspended sediments deposit in stretches of the river. Mining is more frequent during the dry season [12], which at least partly explains seasonal variance where higher contamination is found in the dry season, such as Cd and Cr in surface waters, and Ni and Zn in sediment. Additionally, this also explains the spatially distributed seasonal data gathered for Hg from a single source, which showed higher concentrations in the dry season contrary to most research. These measurements were taken in direct proximity to active mining sites [58] that were releasing large amounts of Hg into the environment at the time of measurement. Unfortunately, no seasonal data for groundwater was available for other metals beyond Hg, which precludes further analysis of temporal dynamics of groundwater. Nevertheless, the results outline significant mobilization potential by precipitation overall, independent of current mining activity.

The data was not aligned in location, time and compartment due to its sourcing in various research papers, making in-depth analyses difficult. Had the data allowed it, temporal and spatial correlation could have given more detailed insight into leaching and transport processes. Unfortunately, this was not possible due to the highly discordant state of the data. Since the majority of research focuses on only one region and one environmental compartment, the examination of potential mass transfer between compartments is not possible. In the future, lower scale sampling campaigns of a specific region over multiple compartments at a higher temporal resolution could fill these gaps in understanding. Additionally, suspended sediment was shown to be particularly sensitive to mining processes [12], so this compartment should be further explored both from a contamination standpoint, and with regard to remobilization from sediment and transport onto floodplains. This goes hand-in-hand with the need to conduct more in-depth simulations of channel erosion and sediment transport processes.

The heavy metal contamination in the basin is particularly concerning given the projected growth of Galamsey activities [47] and climate change. Higher frequency extreme events such as drought and heavy storms will continue to exacerbate the issue, both potentially increasing the pollution problem in waters, sediments, soil and fish, while putting increasing stress on water resources. Currently, the majority of farming in the basin is rain-fed - this is projected to change in the near future, with increasing reliance on surface-water-fed irrigation systems. Using the highly polluted surface waters in the basin for irrigation purposes could have devastating effects on soil quality, crop yields and crop contamination if not managed appropriately. Surface water abstraction plants in the basin managed by GWCL are already experiencing drastically increased treatment costs and shut-downs due to pollutants and high turbidity. Resulting water needs must then be met either through water deliveries of sachets or drums, or communities resort back to using surface waters. These effects will be compounded by the high persistence of metals such as Hg in the environment, which has been demonstrated in currently non-active historic mining sites of the Pra basin [4]. The endangerment of human and ecosystem health therefore requires immediate action.

5.3.1. Risk model for water supply

All water abstraction sites were found to be in areas with at least low levels of heavy metal pollution, therefore none were classified as "Undetectable" according to Table 3. The plants at Kibi, Osino, Bunso, Dunkwa, Twifo-Praso and Daboase all presented with high pollution. Kibi had previously been closed due to damage from Galamsey [72], while GWCL officials in Dunkwa have urged the drilling of boreholes to compensate for diminished treatment capacity [73] due to frequent maintenace shut-downs. The abstraction sites at the Owabi and Barekese dams are comparatively unaffected by heavy metal pollution since

they are upstream of mining sites. At these locations, the low levels of heavy metal contamination can be attributed to runoff from the urban centre of Kumasi.

The only significant predictors of pollution levels identified for surface water abstraction were slope (negative correlation) and the fraction of total upstream area (positive correlation) attributed to mining. Low slopes can lead to the pooling of polluted surface waters and deposition of polluted sediments. Additionally, floodplain inundation might be more significant in areas with flat terrain, potentially carrying more pollutants outside of the channel. Upstream mining areas are the key source of pollution, therefore the direct relationship is to be expected. No other land use classes showed significant correlations, although built-up/bareland, croplands and forests are insignificantly positively correlated. This suggests that other land use classes, such as forests which can take on a nutrient buffering role near rivers, have little influence on pollution levels, and that this insignificant correlation is simply due to the overall distribution in the basin.

It would have been overall more favourable to conduct the pollution level classification using quantitative values from the pollution survey instead of a qualitative classification. Unfortunately, this was not possible as the datapoints available in each location were often of different metals. Additionally, the pollution levels were based on an assessment of all environmental compartments so that all locations could be assessed. The accuracy of this approach depends on the assumption that heavy metals will be present at comparable levels in surface water if they are present in other compartments, which is partially verifiable given the pollution survey results. To remedy this, additional data should be gathered directly on-site. According to the IWRM Report [2], data on heavy metal contaminants at each site is available through the GWCL which could be used to verify the proposed risk model. Once this validation has taken place, the risk predictors can be used for various purposes. For example, if treatment cost data can also be accessed through the GWCL, this could be used to predict future treatment costs of either existing locations that face expansions in upstream mining or for new projects in development. It could also be used to estimate risk of surface water abstraction for irrigation systems.

5.4. Pollution pathway analysis

The following sections discuss the pollution pathway analysis and the outcomes of the specifically developed and tailored methods to assess contamination via surface and sub-surface flows as well as floodplain inundation.

5.4.1. Surface and sub-surface flows

Surface and sub-surface flows over the landscape from mining pits do not explain the widespread contamination in the basin. The pollutant routing algorithm identified only marginal contamination of surfaces beyond mining areas due to beneficial terrain and location with regard to the river network. If pits are flooded, the washed out waters will reach the channel within a short distance and therefore only contaminate small areas, even when taking into account the worst case of contamination expansion. High sensitivity to falsely classified pixels was evident particularly when these pixels were on high terrain. However, these falsely identified locations provided verification of realistic flow routing (see Appendix K).

The computed contamination potential is not a figure of absolute contamination due to the introduction of a numerical stability criterium in the algorithm. In order to prevent the "ballooning" of exponential pollution rates in pixels surrounded by mining, a boundary condition was implemented to fix all existing

mines at an invariable pollutant potential of 1. Additionally, pollutant routing is conducted according to flow routing assuming an ideal system with no losses, sorption, decay or other interactions. Therefore, the output values should only be interpreted qualitatively. A contamination potential of zero implies no contamination of the surface by surface and sub-surface flows from mining sites. High contamination potentials indicate a high likelihood of contamination.

While the algorithm did not contribute to the outlining of potentially endangered areas due to no significant areas susceptible to surface and sub-surface flow contamination being found, the algorithm could be used to model potential contamination by large-scale mines at higher terrain, or underground Galamsey mines that can contaminate wide areas when they flood during the wet season. Similar algorithms have been applied to prioritize sampling campaigns where pollutants have the highest likelihood of occurrence with great success. This algorithm contributes to future applications by modelling diffuse flows similar to D_{inf}-based methods, whereas existing algorithms investigated within this report focused on only one or two potential flow paths [43, 44]. Additionally, the matrix-based format allows for the addition of various other expansions to the pollutant routing model, such as dispersivity, diffusivity, losses, sorption and other parameters commonly included in mass transfer models.

5.4.2. Floodplain inundation modelling

Overall, floodplain inundation behaviour is significant in the basin, particularly when considering that the modelled floods only represent annual maximum mean monthly flows. True flood peaks will occur at much smaller timescales and with significantly higher magnitudes. Assin Praso experienced the highest degree of floodplain behaviour, followed closely by Tontokrom. Osino and Twifo Praso experienced the lowest inundation.

The CTS was shown to be an incomplete indicator of floodplain inundation risk. For example, the case study modelled near Osino is located within very flat terrain with a CTS below 6 m. Nevertheless, it does not experience significant floodplaining. This can be explained by the hydrological index CCR, which was extracted from the HEC-RAS model. Channel capacity at Osino is high compared to the required capacity, reducing risk of significant lateral floodplain expansion. Overall, the Birim and Middle Pra were shown to have particularly flat riverbeds prone to floodplaining.

The CCR was required to complete the risk prediction in the basin. No hydrology data beyond the FLO1K datasets was available, requiring the extraction of a hydrology index from the model. Since channel capacity could not be inferred from the model and no bathymetry data was available, the return period of the first occurrence of backwater effects noticeable in the model were used to approximate exceedance of channel capacity. Instead of modelling, the CCR could also be derived by looking at local bathymetry, or by analyzing accounts of locals with regard to floods.

The proposed risk matrix (see Figure 8) provides a foundation to build upon with higher resolution data, but it requires additional refinement before it can be applied to the basin on a wider scale. Flooding is wide-spread in the basin during the wet season and reaches far beyond the lateral expansion boundaries modelled here, which should be taken into account in any risk model for flooding.

The HEC-RAS model was rudimentary due to a lack of empirical data such as local bathymetry, surface roughness, or rainfall-runoff relationships. Initially, a rainfall-runoff-based approach was attempted using rainfall based on regional Intensity-Duration-Frequency curves, however this approach was abandoned early on due to very high sensitivity to surface roughness and a lack of calibration data such as resulting

storm hydrographs. The HEC-RAS models were run as quasi-unsteady flow simulations with steady discharge according to a given return period for each region over a 5 day period, since the desired outputs of the model were the maximum inundation boundaries. The maximum inundation boundaries are not sensitive to boundary conditions and Manning roughness. However, actual flood peak progressions greatly depend on these inputs for accurate modelling of velocity and depth. This means that the outputs of the model beyond maximum inundation boundaries are not representative of true flood waves. The accurate modelling of floodplain inundation with regard to inundation depth and velocity could yield important insights into potential sediment transport, bed and bank erosion, contamination potential, as well as danger to local communities, but will require much higher resolution data. Despite the large data requirements, it is nevertheless recommended that this be attempted in the future for verification of the current risk model and for future risk assessments. Finally, it is essential to note that this risk model is only meant for the estimation of heavy metal pollution transfer and contamination risk. The risk model does not represent a flood risk model, as flood depth and velocity are essential parameters to accurately estimate this.

5.4.3. Summary of potential pollution transfer pathways

Table 15 summarizes the outcome of the pollution pathway analysis.

Table 15: Summary of the pollution pathway analysis.

Pathway	Analysis Method	Characterization
Surface and sub-surface flows	Pollutant routing model	Localized, not a primary pollution mechanism
Floodplain inundation	HEC-RAS 2D floodplain model and characterization	Key pathway throughout the basin
Aquifer recharge from polluted surface water	Analysis of groundwater aquifer characteristics, river network and literature review of water typology and recharge patterns	Widespread recharge from polluted rivers in the basin, allowing for transport over large distances
Direct drainage and transport via groundwater	Analysis of groundwater aquifer characteristics and pollution survey data	Accounts only for localized pollution in mining regions, transport over large distances unlikely
Wind transport	Not quantified	Not quantified
Intermittent storage and remobilization	Literature review and analysis of pollution survey data	Distinct intermittent storage and remobilization patterns observable

The only pathways that were shown to have significant pollution transfer potential in the Pra basin are contamination via floodplain inundation, and aquifer recharge from polluted surface waters along the river channel. Surface and sub-surface flows were eliminated as main pathways using the aforementioned pollutant routing model. While direct drainage to groundwater may occur, transport through the aquifer is unlikely over large distances. Intermittent storage processes were evident based on the pollution survey results discussed in Section 5.3. Wind transport was not quantified in this experiment.

The findings highlight both the breadth and depth of the pollution problem, and the importance of the river in basin-wide pollution transfer. The pinpointing of mechanisms at play allows for targeted strategies of remediation and management, as well as the prioritization of future research efforts. Details on these recommendations are outlined in the following section.

6. Recommendations

Various experts in Ghana have projected that Galamsey-related pollution of water resources will necessitate the importing of drinking water from neighbouring countries by 2030 [74]. This positions the Galamsey issue at the forefront of the interface between the Ghanaian economy, environment and society, particularly since rising costs of water will have a larger impact on vulnerable communities. This project was able to pinpoint impact pathways so that targeted research and management can take place in the future, which requires an action-oriented approach.

6.1. Future research

The high-priority research areas outlined by this thesis are as follows:

- The publicly available data used in this thesis provided an excellent exploratory basis, but requires targeted on-site validation. Key gaps that prevent verification of findings are the calibration and validation of channel erosion and deposition zones developed by stream power, and empirical hydrograph data of flood peaks to be used in floodplain modelling.
- The discontinuous aquifer presents a high source of uncertainty within communities in close proximity to mining sites. No high-resolution aquifer data was available within the scope of this thesis. In order to better assess risk of groundwater contamination in communities close to mining sites, the surveying of groundwater flow paths via tracers could yield relevant insight into contamination risk, as well as aid in the optimal placement of boreholes, since high local variance in risk is to be expected.
- Channel erosion and related sediment transport, as well as mobilization of suspended sediments, should be assessed in more detail to determine hotspots of potential erosion and pollution contamination risk. The USLE model was shown to not be an accurate model of erosion in the basin, and should therefore not be used as a measure of mining-related erosion processes in the future. A new approach coupling sediment delivery from mining-related processes and channel-driven transport is required.
- The impact of wind transport was not assessed in the context of this thesis due to a lack of ambient air data. However, other research has highlighted the potential contamination by heavy metal-laced dust which can be transported over wide distances [75]. Ambient air concentration measurements near mining sites should be taken to estimate the risk posed by wind transport.
- Various crops have been shown to be contaminated in the basin and within other impacted mining sites [76, 77, 78, 79], including the main cash crop cocoa [80]. Optimal crop selection could aid in the mitigation of human health risk, such as through the use of excluder plants over accumulator plants in areas with polluted soils [81]. Risk categories for subsistence and cash crops should be compiled for the region in a future step.
- No research has been found within the scope of this thesis that details the magnitude of impacts and potential mitigation strategies related to reclaiming pit fields, which should be conducted before any large-scale actions are taken.
- Climate change will lead to more extreme rain events and prolonged droughts in the future, further intensifying the effects of mining on processes such as surface runoff and baseflow [65, 62, 47]. Additionally, heavy metal pollution of surface waters was shown to be sensitive to dilution processes [12]. Droughts and frequent flooding will put additional stress on water resources, compounding the negative effects of Galamsey. Accurate predictions of climate change's effect on the Galamsey issue is an essential tool required to allocate funding for mitigation and remediation, and should be examined to fill significant gaps in understanding.
- The risk predictors and classifications provided within this thesis were not developed in a participa-

tory process that weighed stakeholder interests. It is key that the IWRM planning bodies develop basin-wide risk tolerance levels and management priorities using a collaborative approach that takes into account all relevant stakeholders, and adjusts the risk assessments as needed.
- Finally, in line with the public data focus of this thesis, the generation, use and application of publicly available data should be further explored, as it proved to be an immensely useful tool in contexts when the generation of on-site data is difficult.

6.2. Management recommendations

The river-driven nature of the majority of risks and impacts felt along the Galamsey effect chain provides the opportunity to leverage synergies with existing IWRM priorities. The Pra basin is prone to widespread flooding [2], which not only endangers communities due to its destructive effect on infrastructure, but was also shown to be a main driver of soil and groundwater contamination with mining-related toxic heavy metals. Comprehensive flood protection measures have been outlined as a key priority within the IWRM report [2], which will also contribute to the mitigation of the pollution problem.

Monitoring should be conducted following the optimized approach developed in this thesis by the respective regulatory bodies, to identify active hotspots and to track progress in tackling the mining issue. Demonstrating the scale of mining is also an important tool in communicating the magnitude of the problem to the public.

The severity of the problem requires targeted remediation, particularly for polluted surface waters if the water supply within the basin is to be secured. Surface waters experience two main effects, namely increased turbidity due to high suspended sediment concentrations, and high concentrations of toxic metals. Since it is known that the majority of suspended sediment is bank material [16], bank erosion protection measures such as re-vegetating dredged banks could tackle this problem effectively, while also providing value to the ecosystem [82]. Tackling the heavy metal pollution issue requires a large-scale approach. Constructed wetlands have been proven successful in removing heavy metals via large-scale phytoremediation, making them an attractive remediation option for the basin as they are relatively low-cost and long-lived [83].

Looking forward, water resources should be selected based on intended use and associated risk. Optimal borehole placement in communities close to mines could prevent high levels of contaminants in drinking water by placing boreholes only in areas where no influence of the mines is felt in the aquifer. This is possible in the basin even at small distances to mining sites due to the discordant nature of the aquifer. However, this requires detailed surveying ahead of time. Water used for irrigation systems and the irrigation technology used should be assessed related to the crop at hand. Excluder plants can be fed with polluted waters at little risk. Spray irrigation systems should only be used if the abstracted water is relatively pure, while soil-limited irrigation systems such as channel and drip systems can provide a safer means of water provisioning to excluder plants if waters are polluted without contamination of the leaves and fruit of the crop [81].

Last but not least, it is essential that relevant stakeholders in Ghana be heard and involved in the decision-making process. Galamsey is driven primarily by a lack of other meaningful economic opportunities beyond subsistence farming. Providing knowledge to communities affected by mining additionally enables these communities to exert pressure on relevant regulatory bodies to better manage this issue. Unfortunately, the crack-down on Galamsey has shown little progress in recent years, but this thesis hopes to again underline the importance and urgency of this issue.

7. Conclusion

This thesis investigated the associated risks and impacts of Galamsey-related environmental stressors, which can be grouped into land use changes, river and geomorphological changes, and environmental pollution. Publicly gathered data was used successfuly to answer the main research questions, and to generate future research and management priorities.

A high magnitude of illegal gold-mining as well as diamond mining was identified within the basin, making up a total of 2% of land use over 440 km^2 using a streamlined classification approach. The method based on the Modified Normal Difference Water Index (MNDWI) and Iso Cluster Classification showed excellent accuracy of the mining class (>96% sensitivity and specificity), and required no definition of training samples. Two hotspots of mining were identified in the Offin and Birim subbasins, spanning 140 km and 85 km respectively and reaching lateral widths of up to 4 km. In these regions, mines are dredged directly into the riverbed, significantly disrupting riverrine processes and destroying the local ecosystem.

Galamsey was also shown to significantly impact channel erosion processes. All main channels in the basin showed distinct erosion in the period of 2000 to 2015 based on a DEM of Difference. The mean elevation change of areas classified as mining sites was -3.96 m, which is the largest net loss recorded with exception of the water class, which was subject to high error from the DEM. Stream power correlates with findings of existing literature, but requires additional calibration and validation to enable its use as an indicator of channel erosion risk zones. The USLE was shown to not be an adequate measure of erosion in the basin, due to its inability to model gully and channel erosion processes which are dominant in the basin. A new approach is required that couples sediment delivery to the channel from mining, and resulting transport in the channel. Higher resolution data on discharges and sediment transport is required to achieve this.

The environmental pollution survey resulted in a comprehensive basin-wide dataset of over 2400 datapoints, representing 12 heavy metal concentrations over 168 locations in all environmental compartments with exception of ambient air. Generally elevated heavy metal pollution was demonstrated, with 36% of datapoints exceeding recommended WHO limits for the respective compartment. The segmentation of various potential pollution transfer pathways allowed for the mechanistic understanding of these transport processes, and highlighted the river-driven nature of pollution within the basin. The main pathways that enable widespread pollution throughout the basin were determined to be contamination via floodplain inundation, and aquifer recharge from polluted surface waters. This newly built understanding allows for the targeted deployment of remediation and mitigation strategies that are often synergistic with other basin-wide planning goals such as comprehensive flood protection and the support of biodiversity in riverine vegetation and wetlands.

Finally, the findings of this thesis were generated using exclusively public data, which highlights the potential of this valuable resource. Nevertheless, on-site verification is required before any action is taken based on the results. Further generation, use and application should be encouraged, particularly within contexts where local sampling is difficult to conduct.

Overall, the results highlight the severity and urgency of the Galamsey problem. The effects are felt basin-wide even in communities far away from mining regions, and associated impacts are persistent in the environment. Given that water resources will be put under additional strain due to climate change, it is essential that measures be taken to prevent further damage and to remediate existing sites.

References

[1] Awotwi A. et al. Monitoring land use and land cover changes due to extensive gold mining, urban expansion and agriculture in the Pra basin of Ghana, 1986-2025. *Land Degrad Dev.*, 29:3331–3343, 2018.

[2] Pra River Basin Secretariat. Integrated Water Resources Management Plan. *Water Resources Commission*, 2012.

[3] Asare-Donkor N. et al. Concentrations, hydrochemistry and risk evaluation of selected heavy metals along the Jimi River and its tributaries at Obuasi a mining enclave in Ghana. *Environmental Systems Research*, 4(12), 2015.

[4] Asare-Donkor N. et al. Hydrochemical characteristics of surface water and ecological risk assessment of sediments from settlements within the Birim River basin in Ghana. *Environmental Systems Research*, 7(1):1–24, 2018.

[5] GNA Ghana Business News. Ban on Galamsey still in force. https://www.ghanabusinessnews.com/2019/02/22/ban-on-galamsey-still-in-force-president/. Retrieved in February 2019. .

[6] Adombire M. et al. Business as Usual (BAU) scenario information and analysis covering the Pra and Kakum river basins. *Nature Conservation Research Centre*, 2013.

[7] Duncan A. et al. Assessment of heavy metal pollution in the main Pra river and its tributaries in the Pra basin of Ghana. *Environmental Nanotechnology, Monitoring and Management*, 10:264–271, 2018.

[8] Geological Survey of Denmark and Greenland. Artisanal and small-scale mining handbook for Ghana. *Ministry of Lands and Natural resources Ghana*, 2007.

[9] Owusu-Nimo F. et al. Spatial distribution patterns of illegal artisanal small scale gold mining (Galamsey) operations in Ghana: A focus on the Western Region. *Heliyon*, 4(2), 2018.

[10] Attiogbe F. et al. The impact of mining on the water resources in Ghana: Newmont case study at Birim North District (New Abirem). *Energy and Environment Research*, 7(2):ISSN 1927–0569, 2017.

[11] Duncan A. et al. Assessment of heavy metal pollution in the sediments of the river Pra and its tributaries. *Water Air Soil Pollut*, 8:229–294, 2018.

[12] Afum B. et al. Heavy metal pollution in the Birim river of Ghana. *International Journal of Environmental Monitoring and Analysis*, 4(3):65–74, 2016.

[13] Hilson G. et al. The environmental impact of small-scale gold mining in Ghana: Identifying problems and possible solutions. *The Geographical Journal*, 168:57–72, 2002.

[14] U.S. Fish, Wildlife Service. Anchorage Fish, and Wildlife Field Office. Acid mine drainage and effects on fish health and ecology: A review. *Reclamation Research Group LLC. Bozeman, Montana*, 2008.

[15] Machacek J. et al. Alluvial artisanal and small-scale mining in a river stream - Rutsiro Case Study Rwanda. Biodiversity and Management of Temperate Floodplain Forests. *Forests*, 11(7):762, 2020.

[16] Kusimi J. et al. Sediment yield and bank erosion assessment of the Pra river basin. *Thesis for the award of Doctor of Philosophy. University of Ghana*, 2014.

[17] Kusimi J. et al. Soil erosion and sediment yield modelling in the Pra river basin of Ghana using the Revised Universal Soil Loss Equation (RUSLE). *Environ Geol*, 53:1651–1662, 2008.

[18] Donkor A. et al. Heavy metals in sediments of the gold mining impacted Pra river basin, Ghana, West Africa. *Soil and Sediment Contamination*, 14(6):479–503, 2017.

[19] Dorleku M. K. et al. Effects of small-scale gold mining on heavy levels in groundwater in the Lower Pra basin of Ghana. *Applied Water Science*, 8:126, 2018.

[20] Gyamfi E. et al. Potential heavy metal pollution of soil and water resources from artisanal mining in Kokoteasua, Ghana. *Groundwater for Sustainable Development*, 8:450–456, 2019.

[21] Kessey K. et al. Small-scale gold mining and environmental degradation in Ghana: Issues of mining policy implementation and challenges. *Journal of Studies in Social Sciences*, 5:12–30, 2013.

[22] Nature Conservation Research Centre. Scaling up investment for ecosystem services to meet the global water crisis desired state solution for the Pra and Kakum basins. *Nature Conservation Research Centre*, 2014.

[23] Tay C. et al. Hydrochemical appraisal of groundwater evolution within the Lower Pra basin, Ghana: A hierarchical cluster analysis (HCA) approach. *Environmental Earth Sciences*, 73:3579–3591, 2015.

[24] Erdelyi M. The Hydrogeology of Ghana. *International Association of Scientific Hydrology Bulletin*, 10(1):44–52, 1965.

[25] Data Africa. Subsistence crop production estimates 2011. https://dataafrica.io/profile/ghana. Retrieved in May 2020. .

[26] Gumma M. et al. Mapping irrigated areas of Ghana using fusion of 30m and 250 m resolution remote sensing data. *Remote Sensing*, 3:816–835, 2011.

[27] European Space Agency. Level 1-C Product Formating. *Sentinel Online*, 2020.

[28] European Soil Data Research Centre. Global Soil Erosion GloSEM. https://esdac.jrc.ec.europa.eu/content/global-soil-erosion. 2019. .

[29] Food and Agricultural Organization. FAO/UNESCO Soil Map of the World. http://www.fao.org/soils-portal/soil-survey/soil-maps-and-databases/faounesco-soil-map-of-the-world/en. Retrieved in June 2020.
.

[30] World Agroforesty. The Landscape Portal. http://landscapeportal.org/. Retrieved in April 2020. .

[31] OCHA Services. The Centre for Humanitarian Data. https://centre.humdata.org/. Retrieved in April 2020. .

[32] Barbarossa V. et al. FLO1K, global maps of mean, maximum and minimum annual streamflow at 1 km resolution from 1960 through 2015. *Scientific Data*, 5(180052), 2018.

[33] U.S. Army Corps of Engineers. Hydrologic Engineering Center - River Analysis System HEC-RAS. https://www.hec.usace.army.mil/software/hec-ras/. Retrieved in June 2020. .

[34] ArcGIS Desktop. Image classification using the ArcGIS Spatial Analyst extension. *ArcGIS Online*, 2020.

[35] Xu H. Modification of Normalized Difference Water Index (NDWI) to enhance open water features in remotely sensed imagery. *International Journal of Remote Sensing*, 27(14):3025–3033, 2006.

[36] Du Y. et al. Water bodies mapping from Sentinel-2 imagery with Modified Normalized Difference Water Index at 10-m spatial resolution produced by sharpening the SWIR band. *Remote Sensing*, 8(4):354, 2016.

[37] Smith D. Wischmeier W. Predicting rainfall erosion losses - a guide to conservation planning. *United States Department of Agriculture. Agricultural Handbook. U.S. Government Printing Office. Washington DC. USA*, 1978.

[38] European Soil Data Research Centre. GloSEM Methods Supplementary Notes. 2019. .

[39] Kothyari U. Jain M. Estimation of soil erosion and sediment yield using GIS. *Hydrological Sciences Journal*, 45(5), 2000.

[40] Klik A. Mutua B. Estimating spatial sediment delivery ratio on a large rural catchment. *Journal of Spatial Hydrology*, 6(1), 2006.

[41] Food and Agricultural Organization. Impact of cassava production on the environment. *Proceedings of the validation forum on the global cassava development strategy*, (1), Rome, 26-28 April 2000.

[42] Lee W. et al. Analysis of temporal change in soil erosion potential at Haean-myeon watershed due to climate change. *Korean Journal of Soil Science and Fertilizer*, 47(2):71–70, 2014.

[43] Hwang C. et al. A study on distribution patterns of trace elements in Chungnam coal mine area using factor analysis and GIS. *Geosystem Engineering*, 1(2):84–94, 1998.

[44] Yenilmez F. et al. Evaluation of pollution levels at an abandoned coal mine site in Turkey with the aid of GIS. *International Journal of Coal Geology*, 86:12–19, 2011.

[45] The Engineering Toolbox. Manning's Roughness. https://www.engineeringtoolbox.com/mannings-roughness-d$_7$99.*html*., *RetrievedinAugust*2020.

[46] Saksena S. Plotting the Flood Frequency Curve using Gumbel Distribution. https://serc.carleton.edu/hydromodules/steps/166250.html. *Consortium of Universities for the Advancement of Hydrologic Sciences CUAHSI. Purdue University*, Retrieved in August 2020.

[47] Awotwi A. et al. Water balance responses to land-use/land-cover changes in the Pra river basin of Ghana, 1986-2025. *Catena*, 3, 2018.

[48] Abata S. et al. A review of soil erodibility: A case study of Ugboju settlement of Oturkpo local government area of Benue state, Nigeria. *EPRA International Journal of Multidisciplinary Research* , 2(6):95–102, 2016.

[49] Adongo T. et al. Spatial soil loss estimation using an integrated GIS-based revised universal soil loss equation (RUSLE) in selected watersheds in northern Ghana. *International Journal of Engineering, Science and Technology*, 11(4):58–71, 2019.

[50] Alganci U. et al. Accuracy assessment of different Digital Surface Models. *International Journal of Geo-Information*, 7(114), 2018.

[51] Adokoh C. K. et al. Statistical evaluation of environmental contamination, distribution and source assessment of heavy metals (Al, As, Cd, Hg) in some lagoons and an estuary along the coastal belt of Ghana. *Archives of Environmental Contamination and Toxicology*, 61:389–400, 2011.

[52] Asiamah G. Heavy metal concentration in the Owere river at Konongo. *Master Thesis at Kwame Nkrumah University of Science and Technology*, 2013.

[53] Boateng T. et al. Pollution evaluation, sources and risk assessment of heavy metals in hand-dug wells from Ejisu-Juaben Municipality. *Environ Syst Res*, 4(18), 2015.

[54] Gyimah E. et al. Bioaccumulation factors and multivariate analysis of heavy metals of three edible fish species from the Barekese reservoir in Kumasi, Ghana. *Environ Monit Assess*, 190:553, 2018.

[55] Hadzi E. et al. Assessment of contamination and health risk of heavy metals in selected water bodies around gold mining areas in Ghana. *Environ Monit Assess*, 190:406, 2018.

[56] Oduro W. et al. Assessment of dissolved mercury in surface water along the lower basin of the river Pra in Ghana. *International Journal of Applied Science and Technology*, 2(1):228–235, 2012.

[57] Oppong S. et al. Total mercury in fish, sediments and soil from the Pra river basin, Southwestern Ghana. *Bull Environ Contam Toxicol*, 85:324–331, 2010.

[58] Nartey V. et al. Assessment of mercury pollution in rivers and streams around artisanal gold mining areas of the Birim North District of Ghana. *Journal of Environmental Protection*, 2:1227–1239, 2011.

[59] Nartey N. et al. Sedimentation and sediment core profile of heavy metals in the Owabi reservoir in Ghana. *Lakes and Reservoirs*, 24:173–180, 2019.

[60] Nude P. et al. Use of multi-media sampling as an integrated approach to surficial geochemical sampling for gold in regional reconnaissance surveys in parts of the Ashanti belt, Southwest Ghana. *Research Journal of Environmental and Earth Sciences*, 5(1):18–25, 2013.

[61] Kortatsi B. et al. Hydrogeochemical evaluation of groundwater in the lower Offin basin, Ghana. *Environ Geol*, 53:1651–1662, 2008.

[62] Awotwi A. et al. Analysis of climate and anthropogenic impacts on runoff in the Lower Pra river basin of Ghana. *Heliyon*, 3, 2017.

[63] Ofosu B. et al. GIS-based groundwater level mapping in Ashanti region of Ghana. *International Journal of Sciences: Basic and Applied Research (USBAR)*, ISSN 2307-4531, 2014.

[64] Huang J. et al. Analysis of NDVI data for crop identification and yield estimation. *IEEE Journal of Selected Tropics in Applied Earth Observations and Remote Sensing*, 7(11):4374–4384, 2014.

[65] Kankam-Yeboah K. et al. Impact of climate change on streamflow in selected river basins in Ghana. *Hydrological Sciences Journal*, 58(4):773–788, 2013.

[66] Golubev G. et al. Soil erosion and agriculture in the world: An Assessment and hydrological implications. *Recent developments in the explanation and prediction of erosion and sediment yield. Proceedings of the Exeter Symposium. IAHS Publ. No. 137*, pages 261–268, 1982.

[67] Hadley R. et al. Relation of erosion to sediment yield. *Proceedings of the third federal inter-agency sedimentation conference. U.S. Water Resources Council, Washington D.C.*, pages 1–139, 1976.

[68] Wallng D. et al. The Sediment Delivery Problem. *Journal of Hydrology*, 65:209–237, 1983.

[69] Alewell C. et al. Using the USLE: Chances, challenges and limitations of soil erosion modelling. *International Soil and Water Conservation Research*, 7(3):203–225, 2019.

[70] Mukul M. et al. Uncertainties in the Shuttle Radar Topography Mission (SRTM) Heights: Insights from the Indian Himalaya and Peninsula. *Scientific Reports*, 7(41672), 2017.

[71] Madison R. Effects of placer mining on hydrologic systems in Alaska - Status of knowledge. *US Department of the Interior. Bureau of Land Management. Alaska*, 1981.

[72] Ghana Web. Kibi residents turn water pumping station into recreational center.https://www.ghanaweb.com/GhanaHomePage/NewsArchive/Kibi-residents-turn-water-pumping-station-into-recreational-center-649449. *Regional News*, 2018. Retrieved on 9th September 2020.

[73] Reporting Oil and Gas. Galamsey is killing water bodies. http://www.reportingoilandgas.org/galamsey-is-killing-water-bodies/. 2013. , Retrieved on 9th September 2020.

[74] Ghana Web. Ghana may import water from 2030 - Lands Minister. https://www.ghanaweb.com/GhanaHomePage/NewsArchive/Ghana-may-import-water-from-2030-Lands-Minister-619288. *General News*, 2018. Retrieved on 10th September 2020.

[75] Shahid M. et al. Heavy metal stress and crop productivity. *Crop Production and Global Environmental Issues. Springer International Publishing*, pages 1–25, 2015.

[76] Bortey-Sam N. et al. Accumulation of heavy metals and metalloid in foodstuffs from agricultural soils around Tarkwa Area in Ghana, and associated human health risks. *International Journal of Environmental Research and Public Health*, 12:8811–8827, 2015.

[77] Ametepey S. et al. Health risk assessment and heavy metal contamination levels in vegetables from Tamale Metropolis, Ghana. *International Journal of Food Contamination*, 5(5), 2018.

[78] Ackah M. et al. Uptake of heavy metals by some edible vegetables irrigated using wastewater: A preliminary study in Accra, Ghana. *Environmental Monitoring and Assessments*, 186(1):621–634, 2014.

[79] Anim-Gyampo M. et al. Assessment of heavy metals in waste-water irrigated lettuce in Ghana: The case of Tamale Municipality. *Journal of Sustainable Development*, 5(11), 2012.

[80] Vitola V. The effect of cocoa beans heavy and trace elements on safety and stability of confectionery products. *Rural Sustainability Research*, 35(330), 2016.

[81] Baker A. et al. Accumulators and excluders strategies in response of plants to heavy metals. *Journal of Plant Nutrition*, 3(1-4):643–654, 1981.

[82] Zhu H. et al. The influence of riparian vegetation on bank failures of a small meadow-type mandering river. *Water*, 10(692), 2018.

[83] Pat-Espadas A. et al. Review of constructed wetlands for acid mine drainage treatment. *Water*, 10(1685), 2018.

[84] Kinuthia G. et al. Levels of heavy metals in wastewater and soil samples from open drainage channels in Nairobi, Kenya: A community health implication. *Scientific reports*, 10(8434), 2020.

[85] Sahlin S. et al. Copper in sediment - EQS data overview. *Department of Environmental Science and Analytical Chemistry (ACES). Stockholm University. ACES Report*, 28, 2018.

1. Map Appendix

A. Digital elevation model (DEM) of the Pra basin

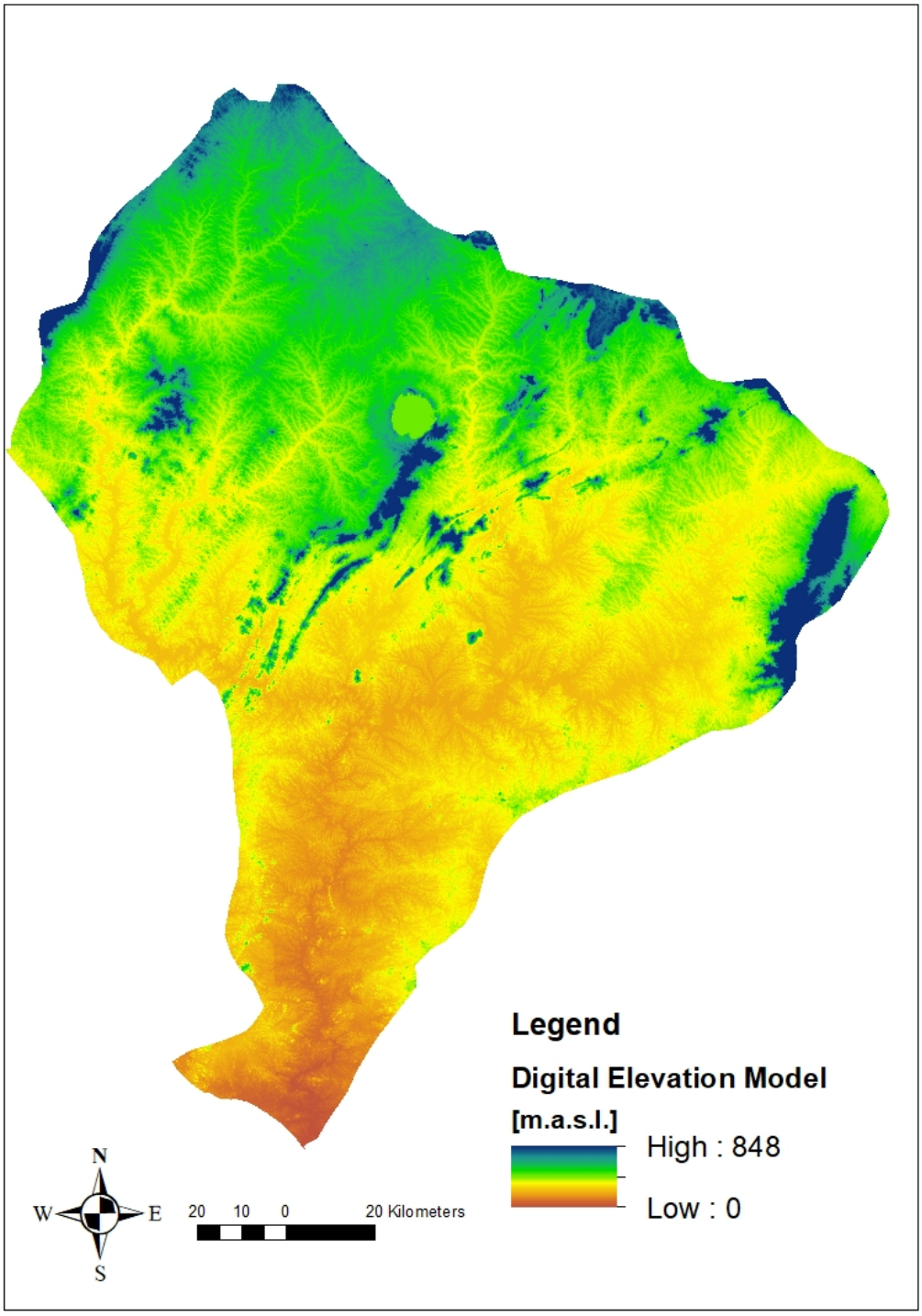

Figure 9: Digital elevation model (DEM) of the Pra basin.

B. Land use classification

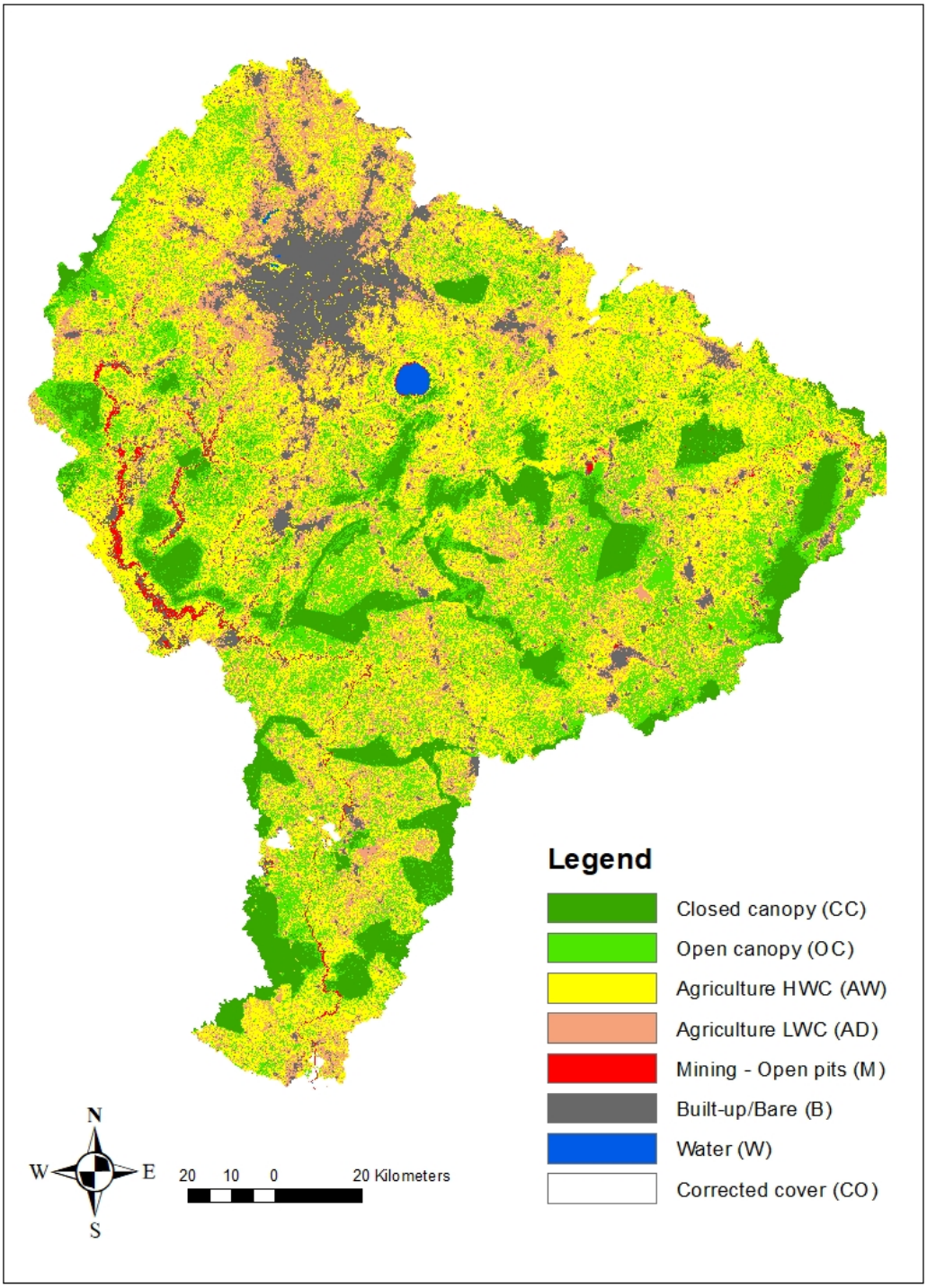

Figure 10: Land use classification.

C. Annual soil loss based on USLE.

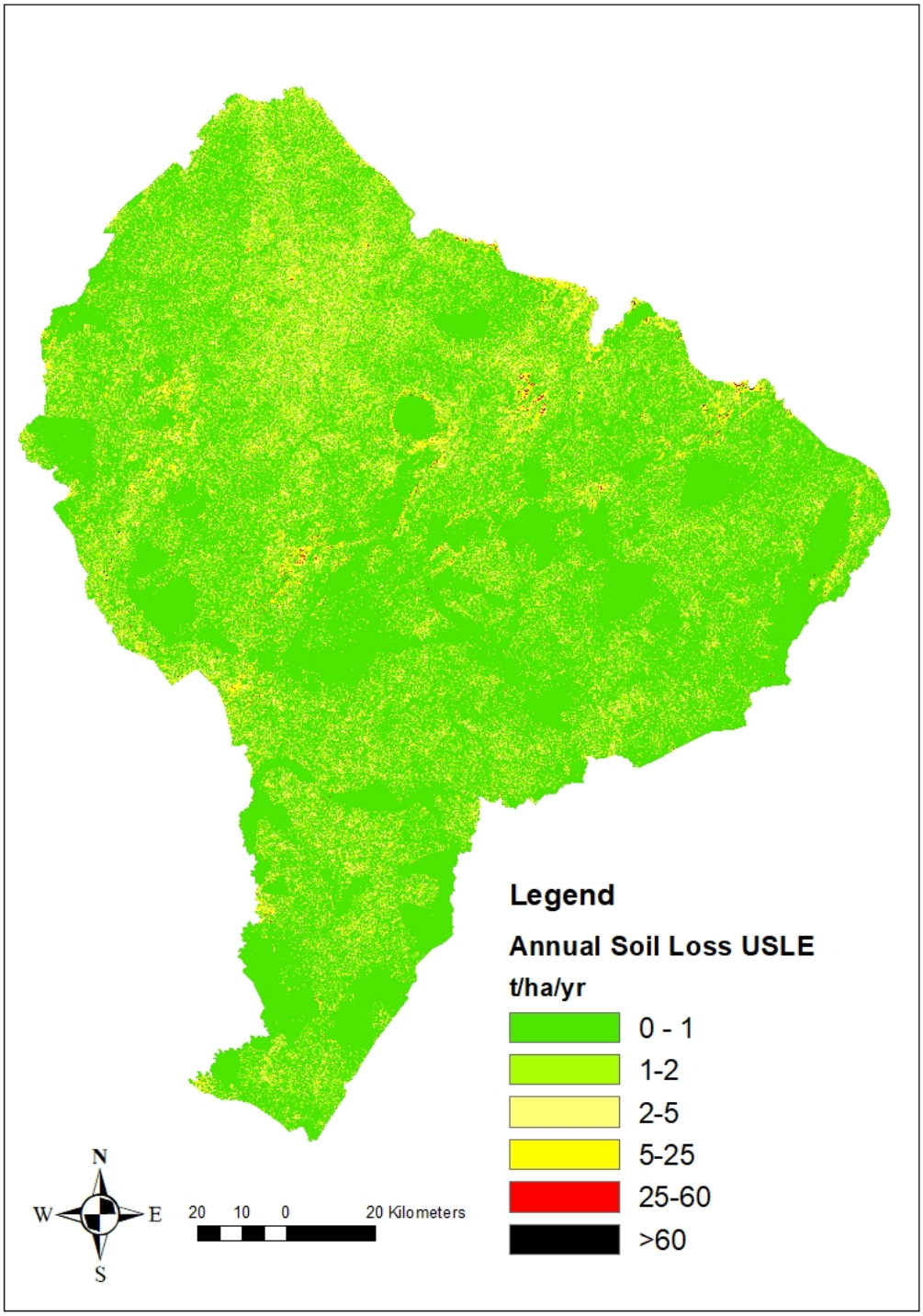

Figure 11: Annual soil loss based on USLE

D. Landscape and riverbed elevation change 2000-2015

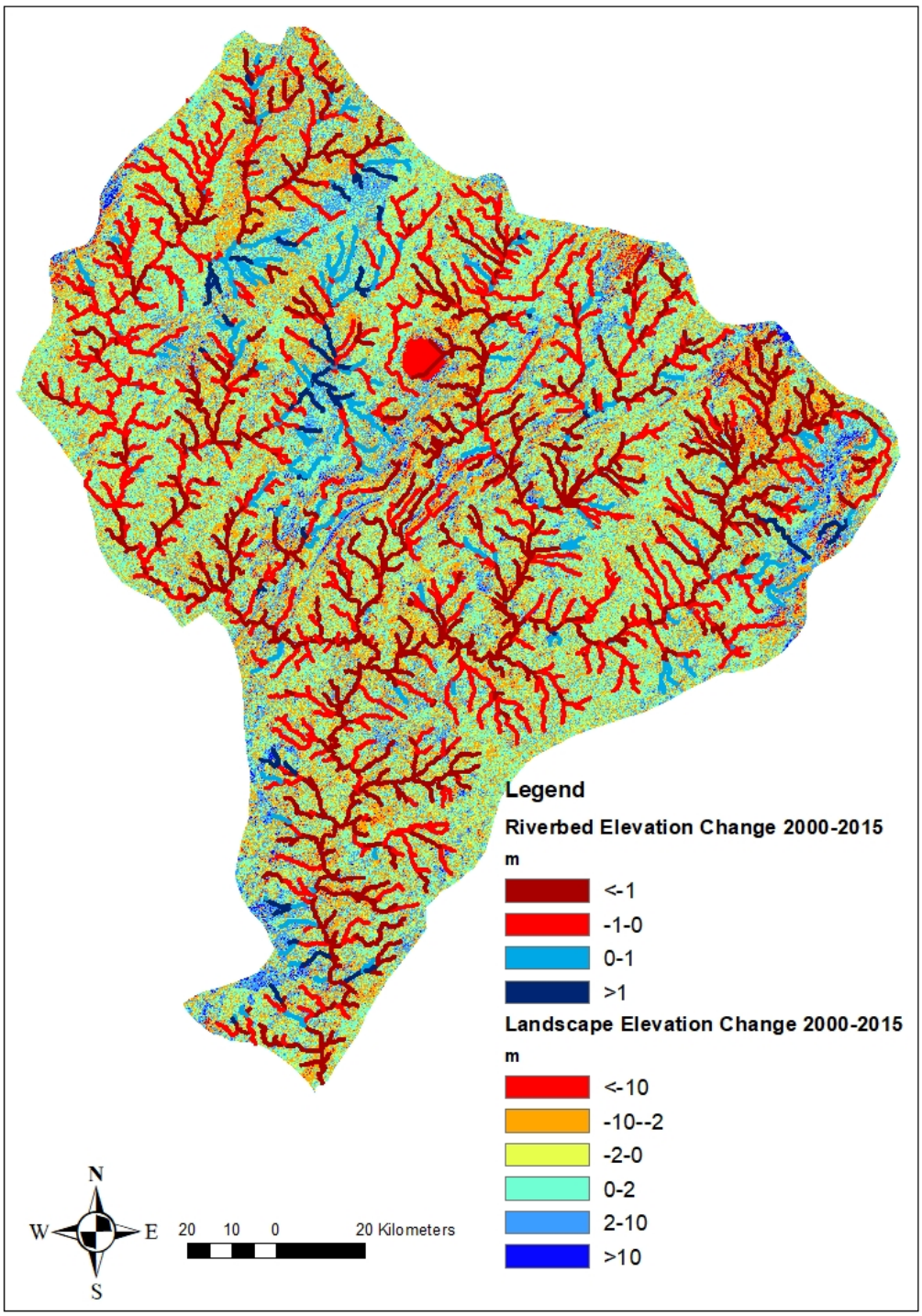

Figure 12: Landscape and riverbed elevation change 2000-2015.

E. Rainfall erosivity factor R

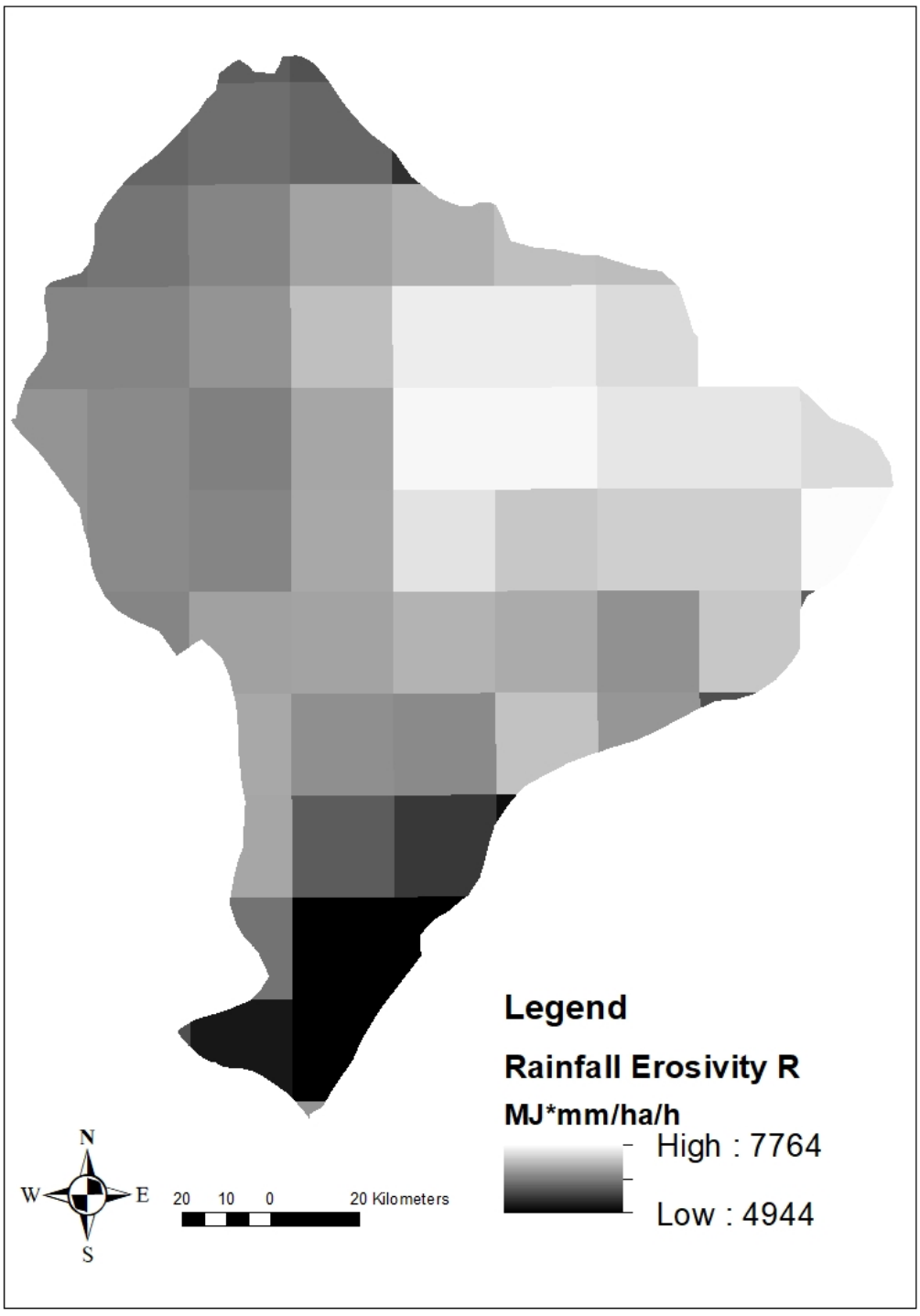

Figure 13: Rainfall erosivity factor R.

F. Soil types

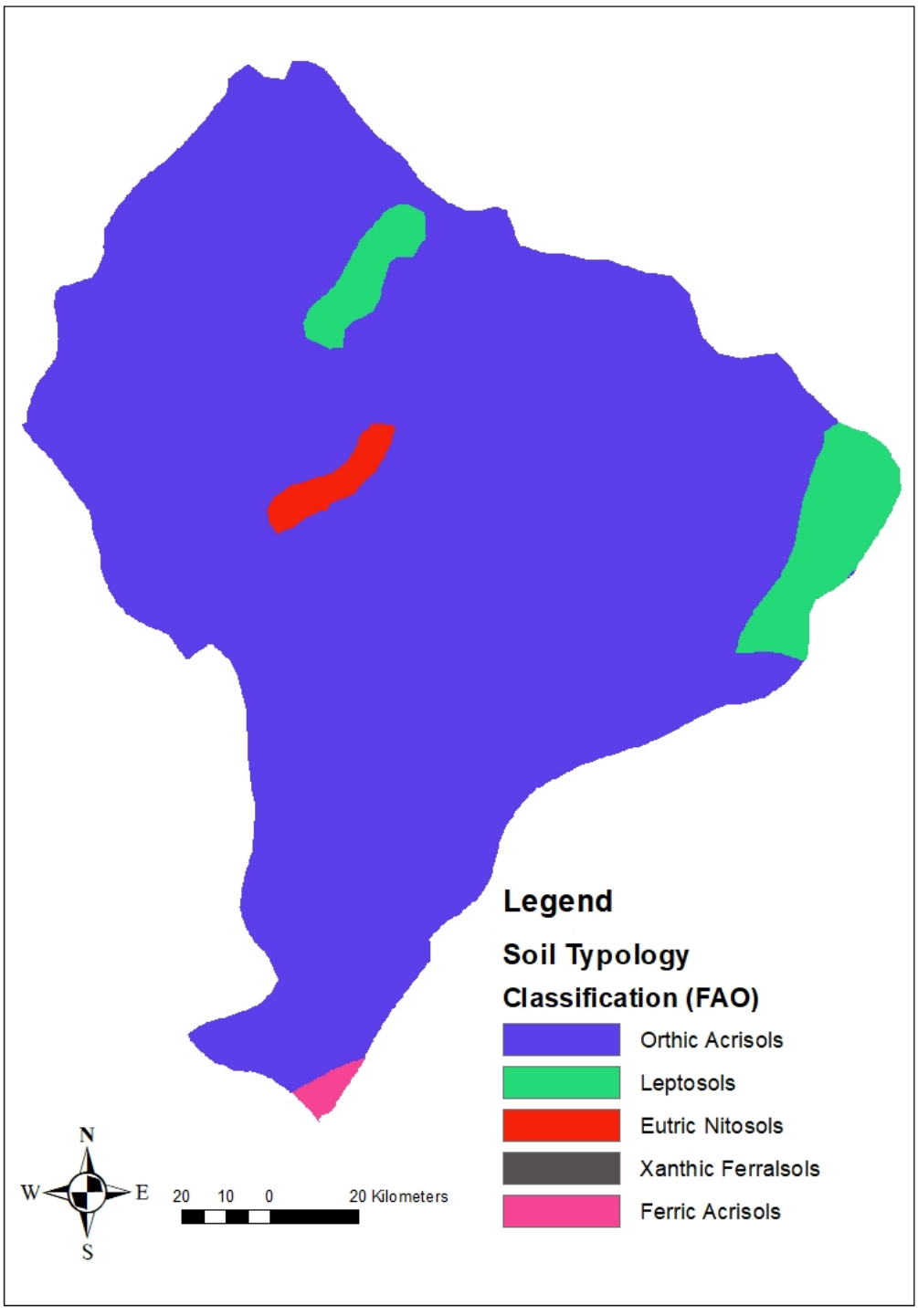

Figure 14: Soil types.

G. Length-slope factor LS

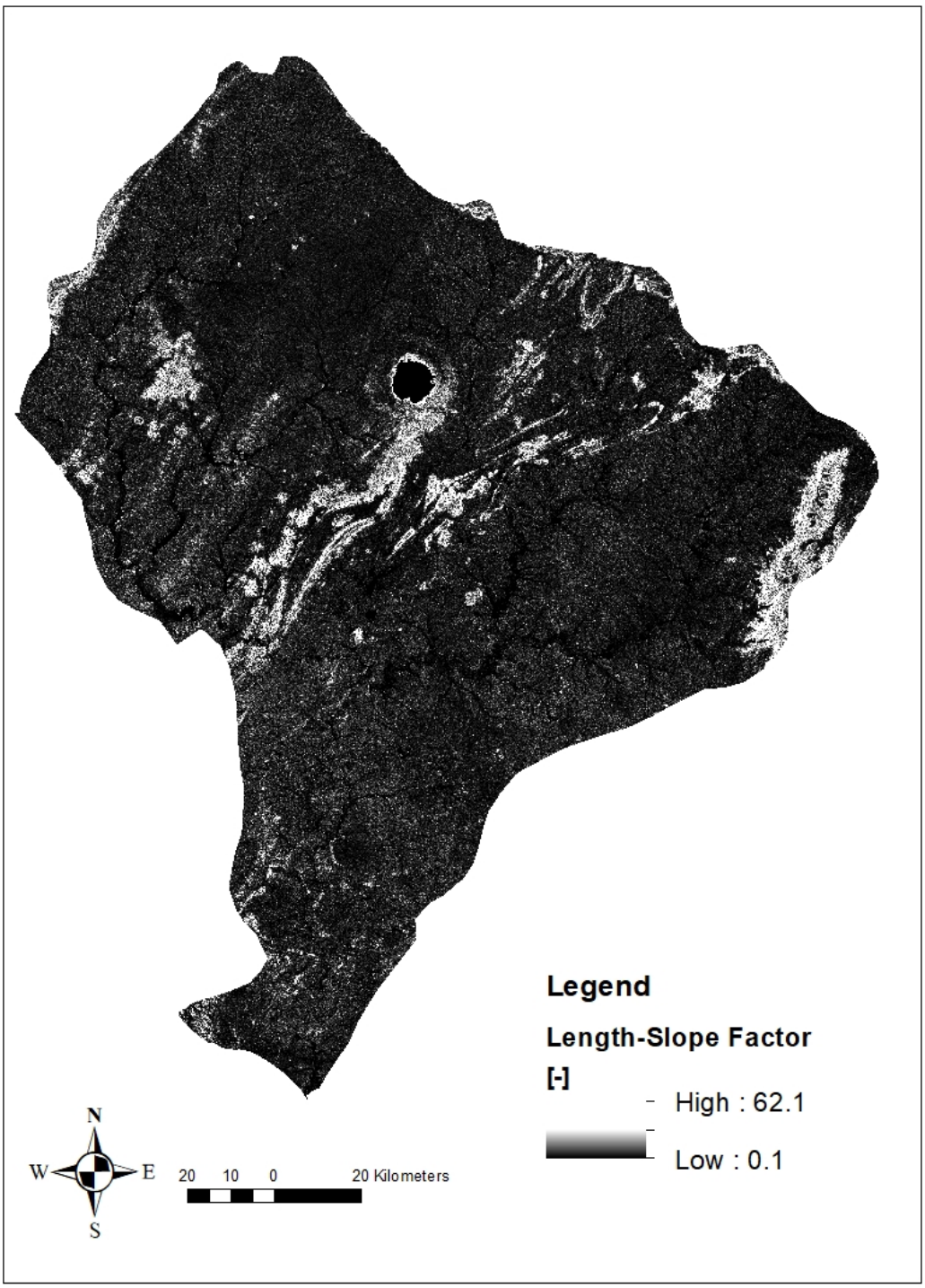

Figure 15: Slope-length factor.

H. Stream power derived from the FLO1K dataset

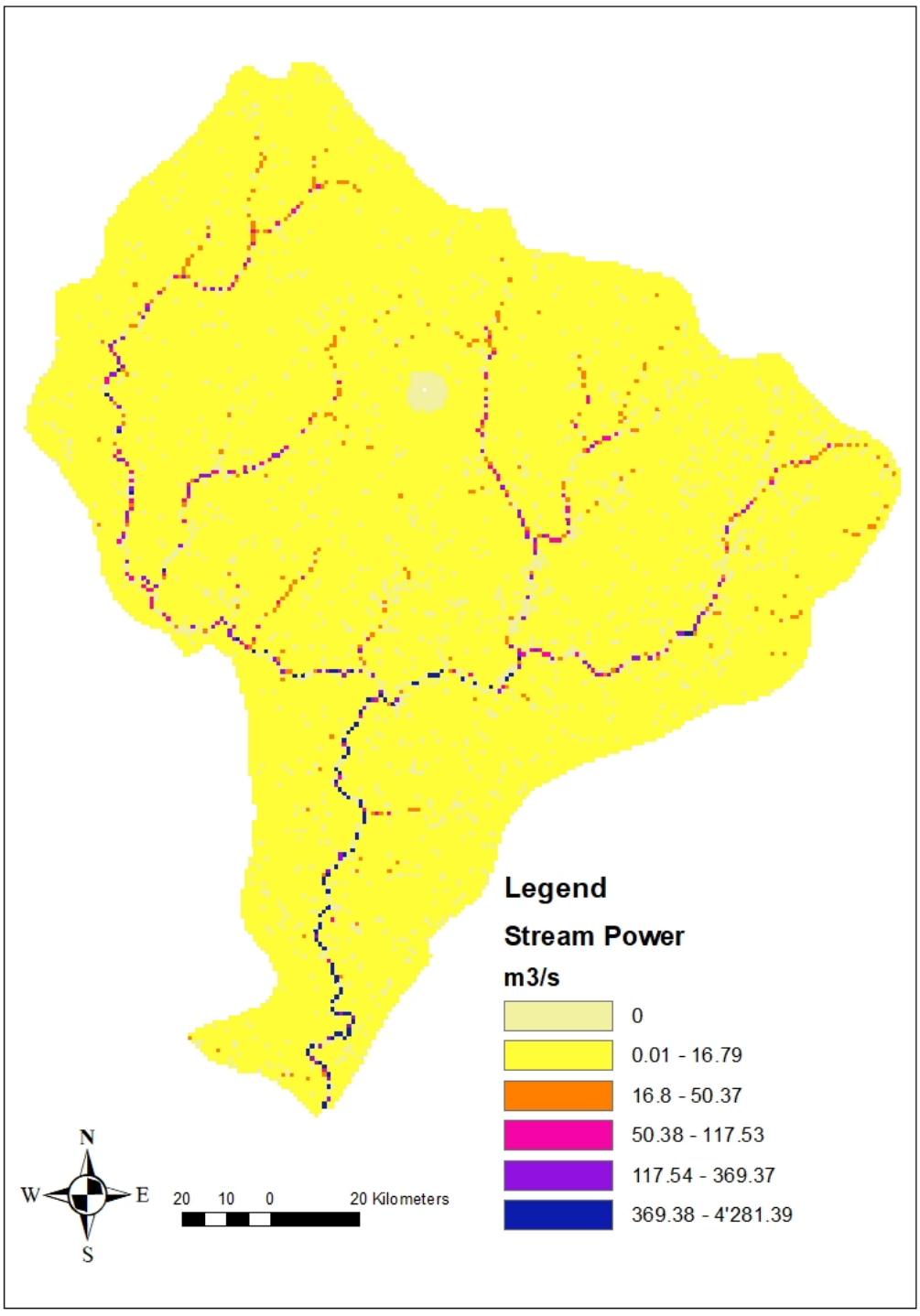

Figure 16: Stream power derived from the FLO1K dataset.

I. Channel erosion and deposition zones derived from stream power

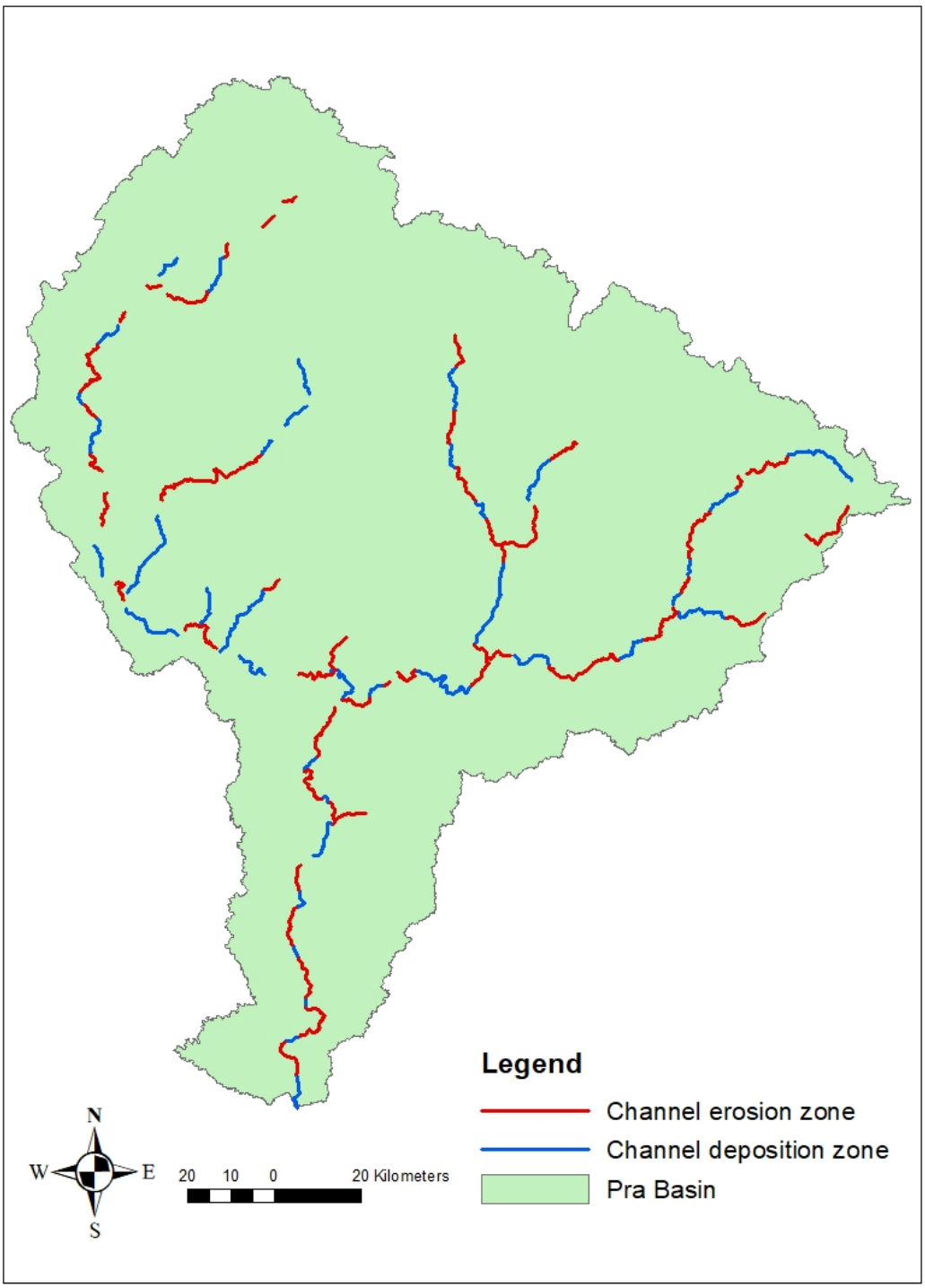

Figure 17: Channel erosion and deposition zones derived from stream power.

J. Heavy metal concentration sampling points

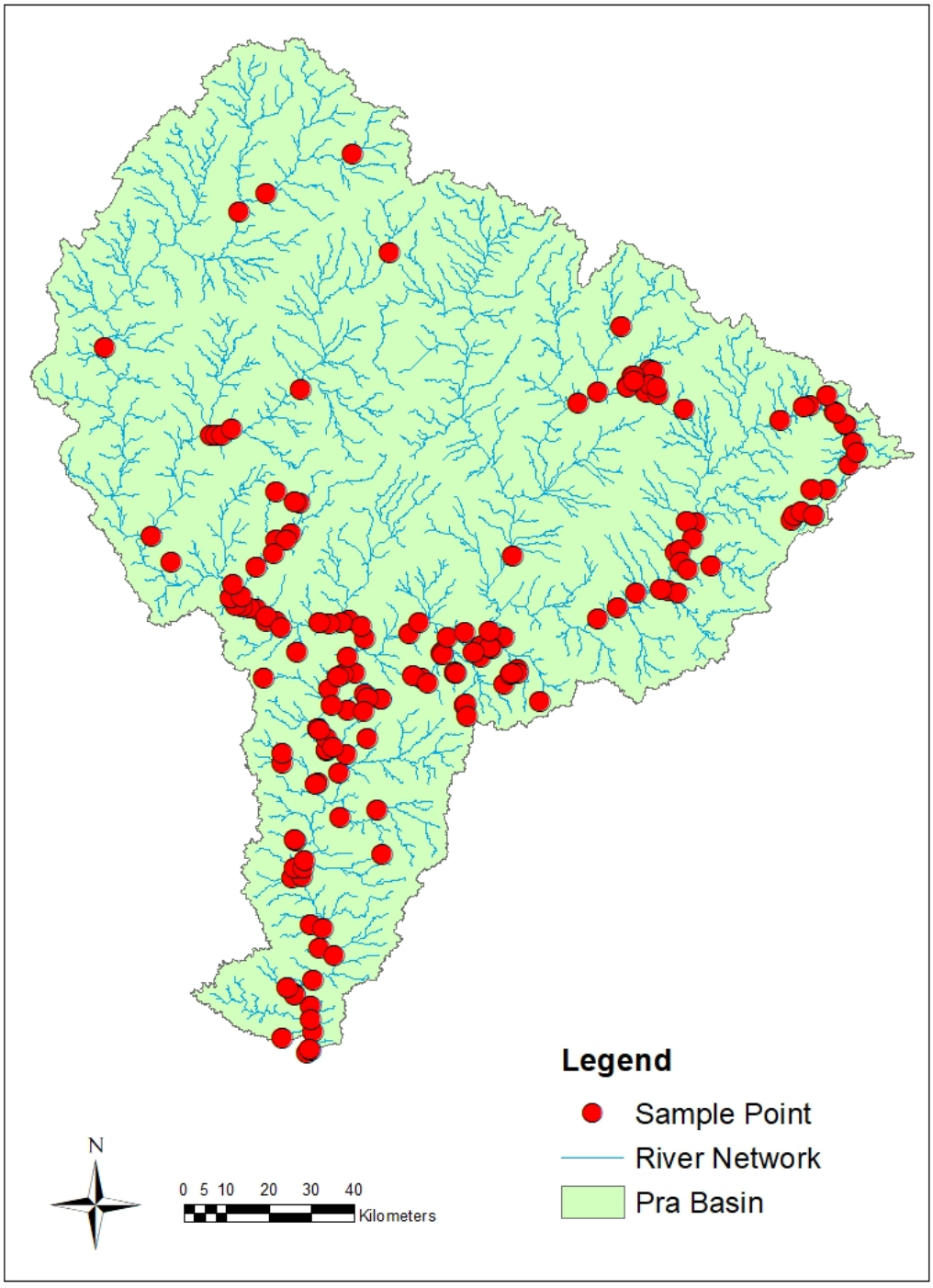

Figure 18: Heavy metal concentration sampling points.

K. Surface water abstraction sites of Ghana Water Company Limited

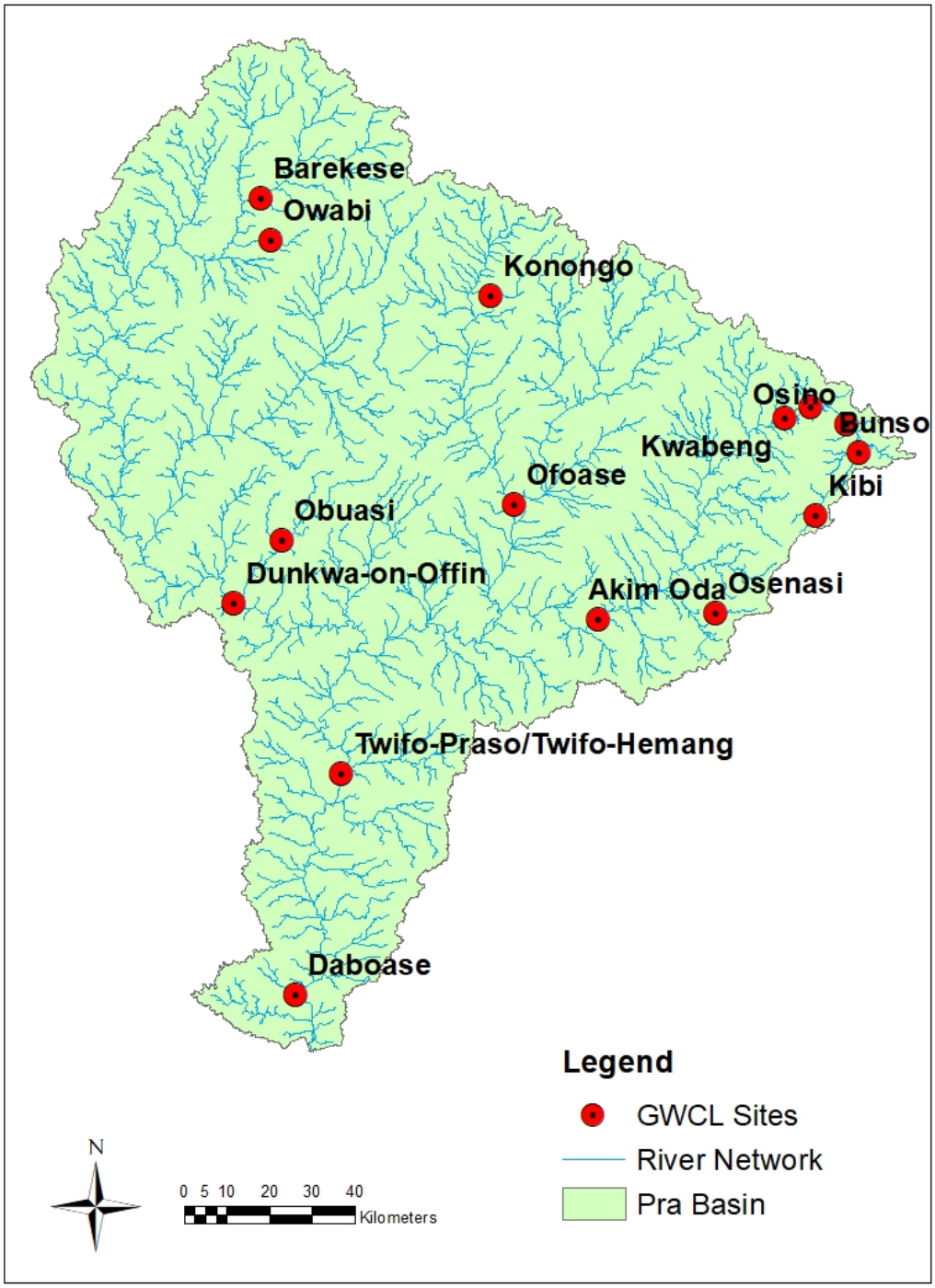

Figure 19: Surface water abstraction sites of Ghana Water Company Limited.

L. Potential surface and sub-surface flow contamination map

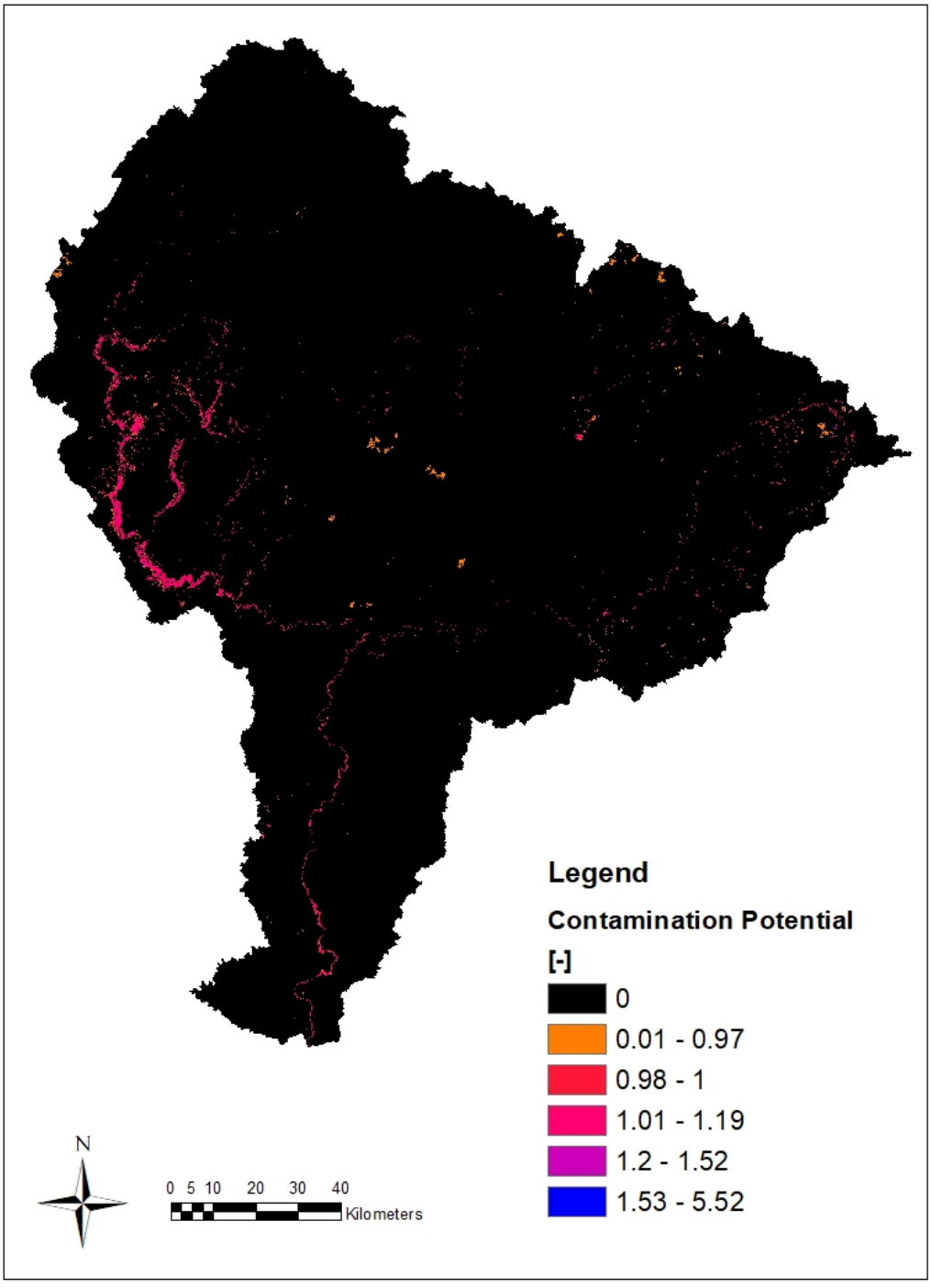

Figure 20: Map of potentially contaminated areas by surface and sub-surface flows, generated using the multi-flow-directional algorithm in MATLAB.

M. Channel terrain steepness

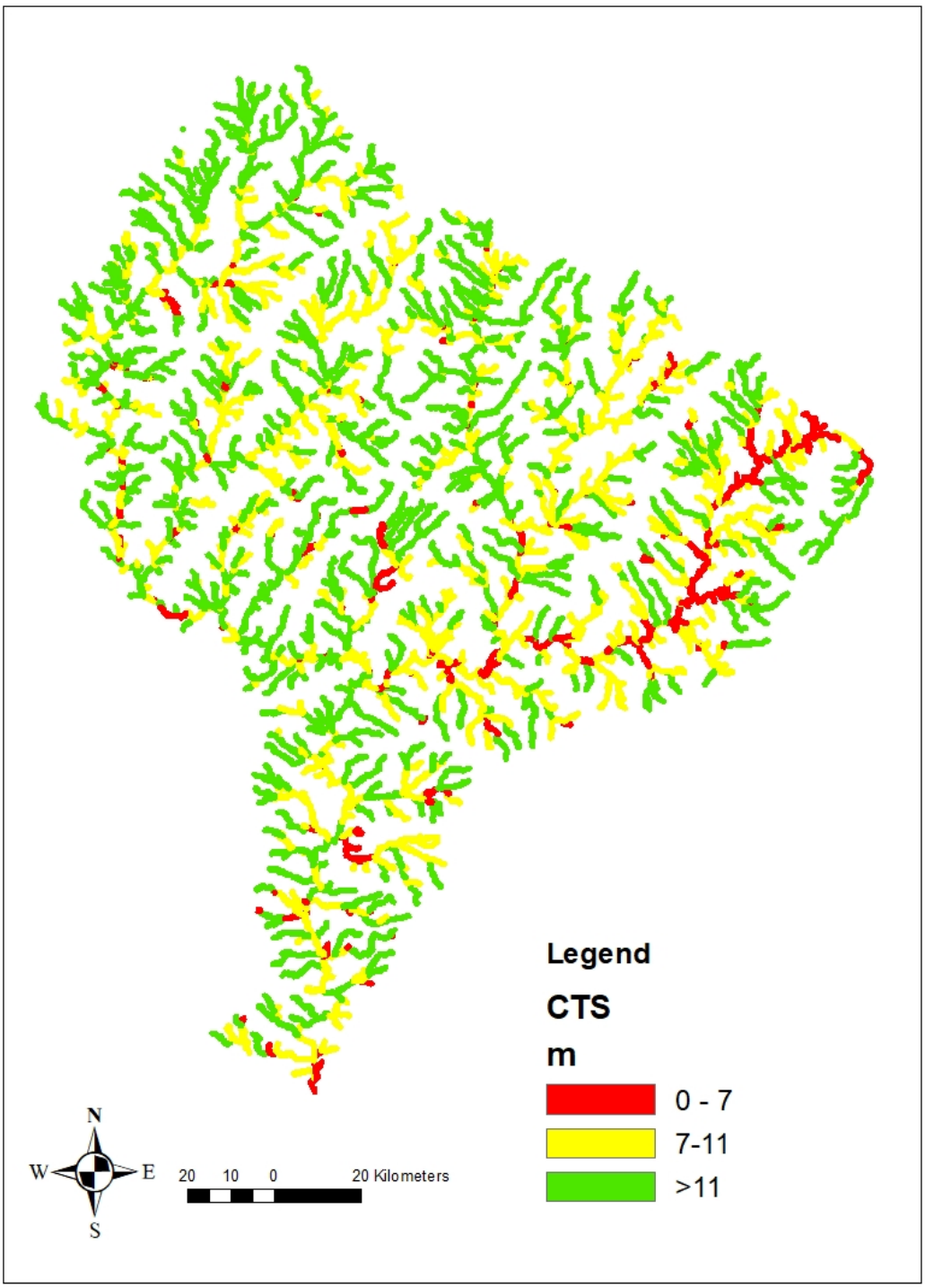

Figure 21: Channel terrain steepness index, derived from the standard deviation of a 750 m double-sided buffer of the DEM.

2. Appendix

A. Digital Appendix and open-source Web-GIS

The Digital Appendix is provided in the supplementary material of the thesis in a **Google Drive**. Please note the Digital Appendix must be opened in the Desktop Excel App to function correctly.

The Web-GIS is provided via **ArcGIS Online**.

B. Calculation of MNDWI and NDVI

This section outlines the computation of the Modified Normal Difference Water Index (MNDWI) and the Normalized Difference Vegetation index (NDVI). The MNDWI compares the green and shortwave infrared (SWIR) bands, e.g. Sentinel-2 bands 3 and 12 respectively (see Equation 7). The NDVI compares the red and near infrared (NIR) bands, e.g. Sentinel-2 bands 4 and 8 respectively (see Equation 8).

The MNDWI distinguishes between areas with high and low water content - the higher the water content, the higher the MNDWI (up to 1). Similarly, the NVDI detects vegetated vs. non-vegetated areas.

$$MNDWI = \frac{Green - SWIR}{Green + SWIR} = \frac{B3 - B12}{B3 + 12} \tag{7}$$

$$NDVI = \frac{NIR - Red}{NIR + Red} = \frac{B8 - B4}{B8 + B4} \tag{8}$$

The MNDWI and NDVI indexes were used as the foundation of mining pit detection. Mining pits are wet, turbid and unvegetated, meaning they have high MNDWI and low NDVI (see Appendices E and F). Using the input bands of the MNDWI and the NDVI, the false colour composite and true colour image shown in Appendix C were used as an input to Iso Cluster Classification. These images combine bands 2, 3, 4 and 12, e.g. blue, green, red and shortwave infrared.

C. Image stack used in classification

Figure 22 compares a true colour image (TCI) from Sentinel-2, which combines the red, blue and green bands, and the false colour composite (FCC), which combines bands 2, 3 and 4 to optimally detect open pit mines. Open pit mines are visualized in bright yellow, and are therefore clearly distinguishable from their suroundings. The FCC also allows for the separation of built-up and bareland, which is difficult to do using only the TCI.

(a) True colour image (TCI) - Sentinel-2 bands 2, 3 and 4, and delineated river network.

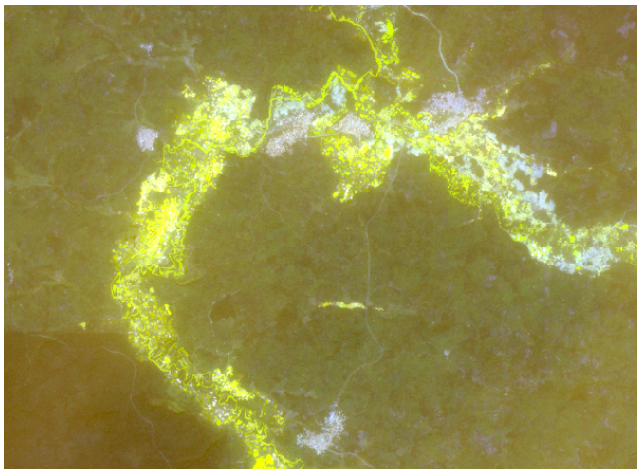

(b) False colour composite (FCC) - Sentinel-2 bands 2, 3 and 12

Figure 22: Comparison of the True Colour Image and the False Colour Composite, the inputs used in the Iso Cluster Unsupervised Classification procedure.

The FCC is based on the Modified Normal Difference Water Index (MNDWI), shown in Figure 23. The MNDWI can be computed using both Shortwave Infrared (SWIR) bands of the Sentinel-2 package. However, the SWIR 2 band (see Figure **??**) was shown to be more sensitive for the detection of mining pits, built-up/bareland, and different agricultural crop classes.

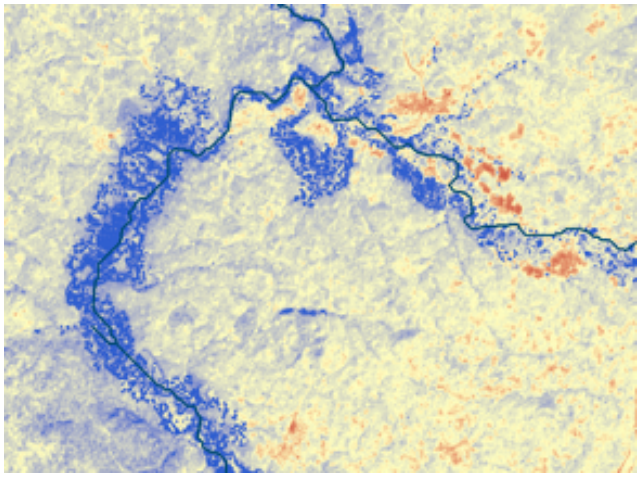

(a) MNDWI using band 11 (SWIR 1)

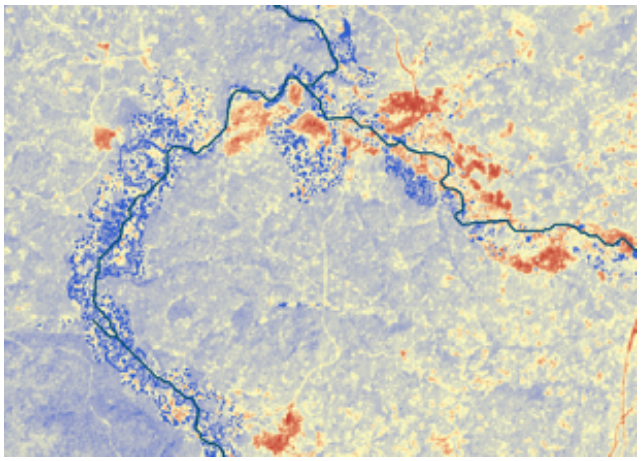

(b) MNDWI using band 12 (SWIR 2)

Figure 23: Comparison of the Modified Normal Difference Water Index (MNDWI) computed using band 11 (1610.4-1613.7 nm) and band 12 (2185.7-2202.4 nm). Blue indicates MNDWI > 0, red indicates MNDWI < 0.

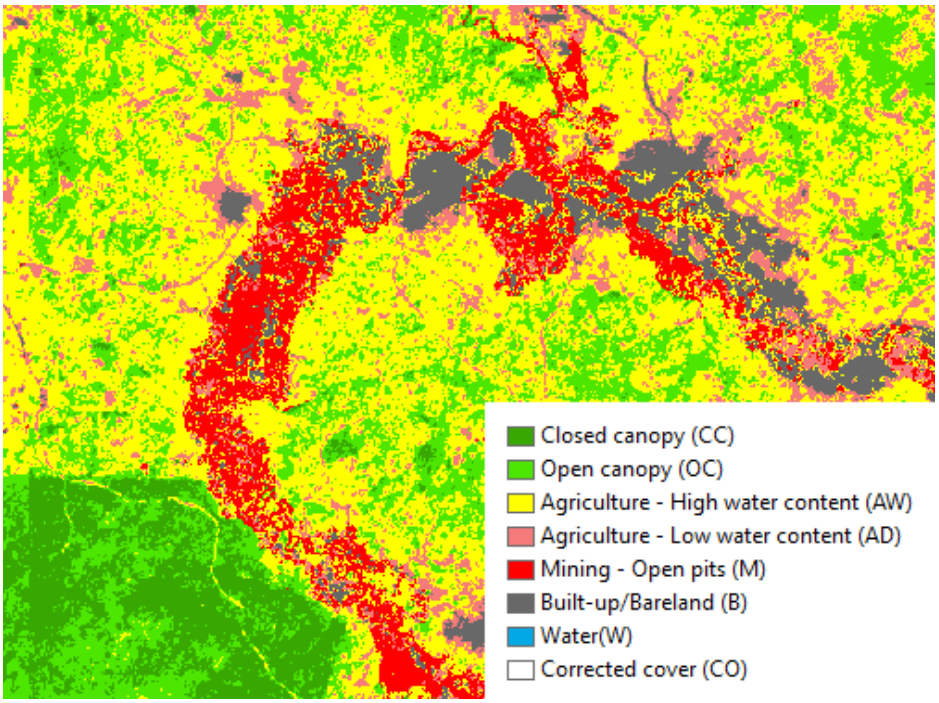

Figure 24: Land use classification based on the TCI and FCC.

Figure 24 demonstrates the resulting land use classification of the TCI and FCC images.

D. WHO recommended heavy metal exposure limits

Type	Unit	Al	As	Cd	Cr	Cu	Fe	Hg	Mn	Ni	Pb	Se	Zn
Drinking water	[mg/l]	0.2	0.01	0.003	0.05	2	0.3	0.001	0.4	0.07	0.01	0.01	3
Sediment	[mg/kg]	1	7	1.1	50	36	28000	2	600	25	23		88
Soil	[mg/kg]							0.05					

Table 16: WHO recommended limits of heavy metal concentrations by environmental compartment [7, 11, 84, 85].

E. Spectral signatures of land use classes

The spectral signatures by land use class are visualized in Figure 25. The spectral signatures of mining pits show noticeable differences to the other classes in Band 2 (Blue), Band 3 (Green), Band 11 and Band 12 (Shortwave Infrared SWIR 1 and 2). This spectral signature has similarities to the Modified Normal Difference Water Index (MNDWI) that differences the green and SWIR bands of Sentinel-2 to visualize water content distribution due to the high absorbability of SWIR on water.

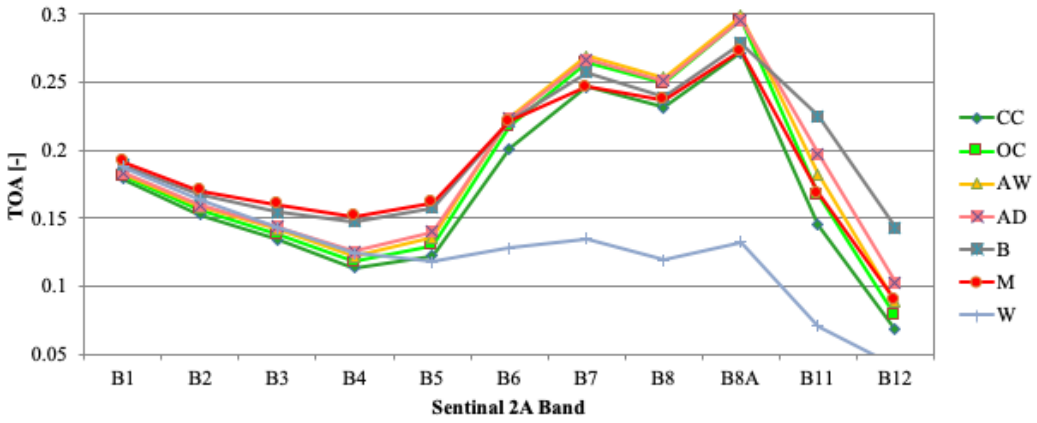

Figure 25: Results of the spectral analysis of land use classes. Top of Atmosphere Reflectance (TOA) was averaged for each land use class for all Sentinel-2 bands.

F. Comparison of MNDWI and NDVI by land use class

Figure 26 compares the MNDWI and NDVI of the land use classes of the Pra basin. While the NDVI shows little separation between mining and built-up/bareland areas, the MNDWI is able to successfully distinguish between the two land use types.

Figure 26: Comparison of the MNDWI and NDVI by land use class.

G. Buffer analysis

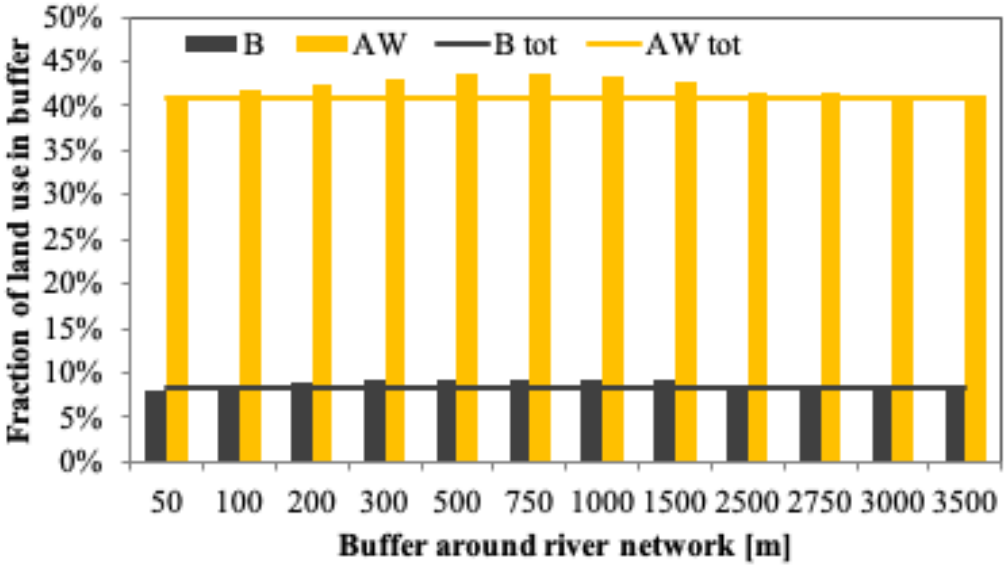

Figure 27: Proximity analysis of the B and AW classes comparing proximity to river to fraction of land use.

H. Validation of the FLO1K dataset

Figure 28 visualizes the correlation analysis of the IWRM reported discharges and the mean FLO1K dataset. Table 17 shows the related data. The FLO1K dataset showed an excellent fit to the IWRM reported values.

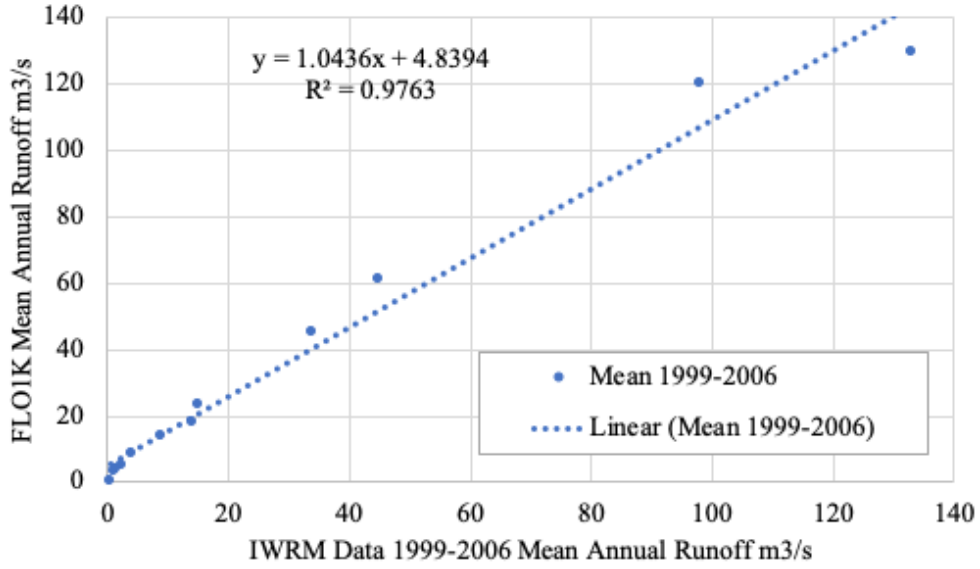

Figure 28: Correlation of IWRM reported discharges and the mean FLO1K dataset.

River gauging station	Basin	Total catchment	Estimated areal rainfall	Local runoff	Runoff coeff	Mean annual runoff	Mean annual runoff	Mean annual runoff FLO1K	STD - FLO1K
		km2	mm	mm/a		m3/s	mm3/s	m3/s	m3/s
Daboase	Pra	22820	1600	532	0.33	133	4200	130	52.1
Twifo-Praso	Pra	20766	1450	230	0.16	98	3100	120	49.2
Assin-Praso	Pra	9792	1400	137	0.1	45	1420	61	26.9
Dunkwa/Adwumain	Pra / Offin	8344	1375	122	0.09	34	1085	45	16.7
Ampunyase	Pra / Jimi	396	1375	124	0.09	1.6	49	4	1.1
Adiembra	Pra / Offin	3132	1350	146	0.11	14	440	18	6.5
Bekwai/Anwia-Nkwanta	Pra / Oda	958	1350	131	0.1	4	125	8	3.1
Mmuronem	Pra / Anum	1799	1375	159	0.12	9	285	14	5.7
Offinso	Pra / Offin	674	1350	119	0.09	2.5	80	5	2.0
Dadieso	Pra	103	1400	159	0.11	0.5	16	n.a.	n.a.
Akim-Oda	Pra / Birim	3247	1400	146	0.1	15	480	23	10.1
Osino	Pra /Birim	208	1450	170	0.12	1.2	39	3	0.9

Table 17: Results of the validation procedure comparing IWRM reported discharges and the mean FLO1K dataset.

I. Landscape evolution due to mining

Figure 29 demonstrates the evident erosive behaviour of mining pits based on the DEM of Difference by comparing landscape elevation change from 2000 to 2015 and underlying mining pit fields.

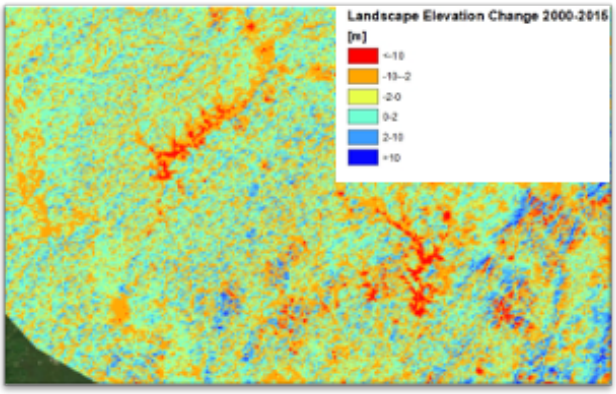

(a) Example of landscape elevation change from 2000-2015 in the Mid-Offin region, showing significant erosion of riverbed and -banks in mining areas.

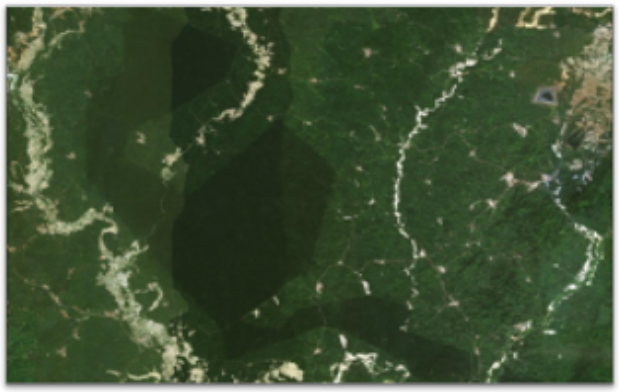

(b) True colour image showing mining pit fields underlying regions that experience the most significant erosion.

Figure 29: Example of erosive behaviour underlying mining sites based on the DEM of Difference between 2000-2015.

J. Pollutant routing algorithm

```
%% Initialise data
% Read tifs as grid object matrices

DEM = GRIDobj('DEMxutm.tif');
[DEM_utm,DEM_zone] = reproject2utm(DEM,30);

% Get iteration length, iteration length s computes pollutant potential map
% across s cells, e.g. distance = s* cell size
% If cell size = 30m, s = 100 --> results cover 30*100m away from source,
% e.g. 3000 m from source
%DEM = DEM_utm;


ppot = GRIDobj('pitsexm.tif');

% fill sinks in DEM
DEM = fillsinks(DEM);
DEM.Z(DEM.Z<0) = NaN;
DEM.Z(DEM.Z==0) = NaN;

%remove last row and line of DEM to equal size of ppot
dem_rast = DEM.Z;
dem_rast(end,:) = [];
dem_rast(:,end) = [];


%% Pollutant potential mapping
% Initialise matrices
E = zeros(size(dem_rast));
SE = zeros(size(dem_rast));
S = zeros(size(dem_rast));
SW = zeros(size(dem_rast));
W= zeros(size(dem_rast));
NW = zeros(size(dem_rast));
N = zeros(size(dem_rast));
NE = zeros(size(dem_rast));

res = DEM.cellsize;
diag = (res*res + res*res)^0.5;

for i = 2:(length(dem_rast(:,1))-1)
for j = 2:(length(dem_rast(1,:))-1)
E(i,j) = (dem_rast(i,j)-dem_rast(i,j+1))/res;
SE(i,j) = (dem_rast(i,j)-dem_rast(i+1,j+1))/diag;
S(i,j) = (dem_rast(i,j)-dem_rast(i+1,j))/res;
SW(i,j) = (dem_rast(i,j)-dem_rast(i+1,j-1))/diag;
W(i,j) = (dem_rast(i,j)-dem_rast(i,j-1))/res;
NW(i,j) = (dem_rast(i,j)-dem_rast(i-1,j-1))/diag;
N(i,j) = (dem_rast(i,j)-dem_rast(i-1,j))/res;
NE(i,j)= (dem_rast(i,j)-dem_rast(i-1,j+1))/diag;
end
end

% Compute total slope difference
slope_denom = zeros(size(E));

E(E<0) = 0;
SE(SE<0) = 0;
```

```
S(S<0) = 0;
SW(SW<0) = 0;
W(W<0) = 0;
NW(NW<0) = 0;
N(N<0) = 0;
NE(NE<0) = 0;

E_slope=zeros(size(E));
SE_slope=zeros(size(E));
S_slope=zeros(size(E));
SW_slope=zeros(size(E));
W_slope=zeros(size(E));
NW_slope=zeros(size(E));
N_slope=zeros(size(E));
NE_slope=zeros(size(E));


% get slope-based routing weights
for i = 1:length(E(:,1))
for j = 1:length(E(1,:))
slope_denom(i,j) = E(i,j)+SE(i,j)+S(i,j)+SW(i,j)+W(i,j)+NW(i,j)+N(i,j)+NE(i,j);
E_slope(i,j)=E(i,j)/slope_denom(i,j);
SE_slope(i,j)=SE(i,j)/slope_denom(i,j);
S_slope(i,j)=S(i,j)/slope_denom(i,j);
SW_slope(i,j)=SW(i,j)/slope_denom(i,j);
W_slope(i,j)=W(i,j)/slope_denom(i,j);
NW_slope(i,j)=NW(i,j)/slope_denom(i,j);
N_slope(i,j)=N(i,j)/slope_denom(i,j);
NE_slope(i,j)=NE(i,j)/slope_denom(i,j);
end
end

% Multiply with pollutant potential map

% Get initial pollutant map where source = 1, all other cells = 0
poll = ppot.Z;
poll(isnan(poll))=0;

%set iteration steps
x = 1;
s = 500;
% Iterate through s pollutant transport steps

while x ≤ s
% get transport downstream according to slope partitioning
poll_E = poll.*E_slope;
poll_SE = poll.*SE_slope;
poll_S = poll.*S_slope;
poll_SW = poll.*SW_slope;
poll_W = poll.*W_slope;
poll_NW = poll.*NW_slope;
poll_N = poll.*N_slope;
poll_NE = poll.*NE_slope;

new_poll = zeros(size(E));

% disperse downstream proportional to slope by computing inflows into each
% cell from the direction matrices

for i = 2:length(E(:,1))-1
```

```
119 for j = 2:length(E(1,:))-1
120     if poll(i,j) ==1
121         new_poll(i,j) = 1;
122     else
123         new_poll(i,j) = poll_E(i,j-1) + poll_SE(i-1,j-1) + poll_S(i-1,j) + ...
                poll_SW(i-1,j+1) + poll_W(i,j+1) + poll_NW(i+1,j+1)+ poll_N(i+1,j) + ...
                poll_NE(i+1,j-1);
124     end
125 end
126 end
127 new_poll(isnan(new_poll))=0;
128 %max_newpol = max(new_poll, [], 'all');
129 %new_poll = new_poll./max_newpol;
130 poll = new_poll;
131 fprintf('x = %f\n', x);
132 x = x+1;
133
134 end
```

K. Example inputs and outputs to the pollutant routing algorithm

Figure 30 demonstrate example inputs into the pollutant routing algorithm (see Appendix J for source code). The required inputs are the DEM of the desired modelling area, and the initial pollutant source matrix. The pollutant source matrix is derived from the land use classification. Figure 31 demonstrates the algorithm output following n=500 runs (e.g. a modelling distance of n x 30 m). Realistic pollutant routing is evident in a diffusive fashion along the terrain slopes.

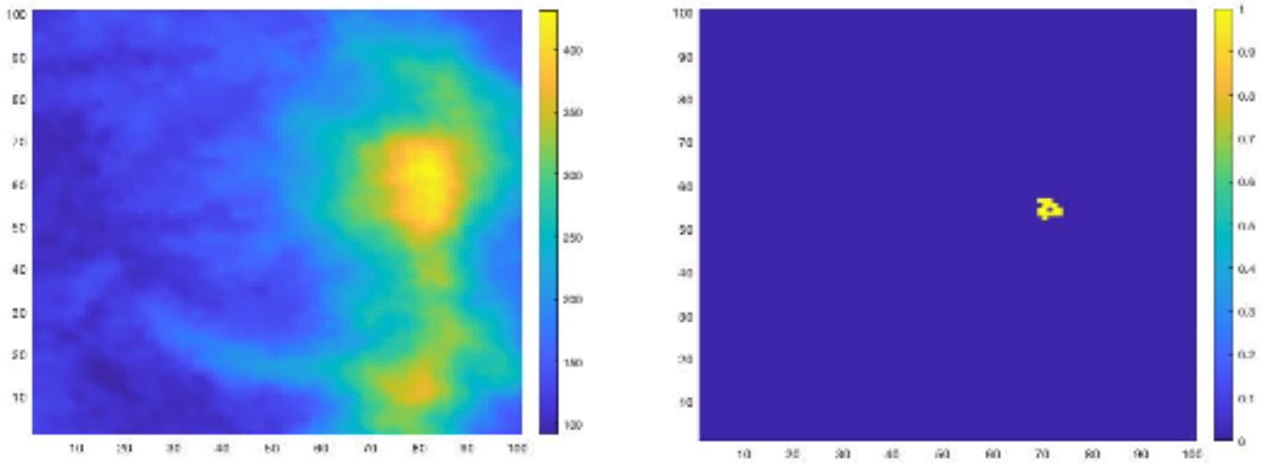

(a) Example DEM of the study area

(b) Example initial pollutant source matrix

Figure 30: Inputs into the pollutant routing algorithm.

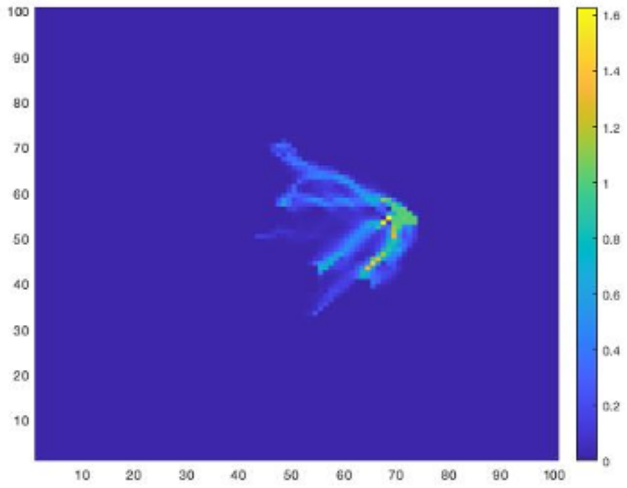

Figure 31: Output of the pollutant routing algorithm after n = 500 runs.

L. Heavy metal pollution survey

L.1. Statistics by compartment and season

Compartment		Al			As			Cd			Cr		
		W	D	U	W	D	U	W	D	U	W	D	U
Sediment [mg/kg]	#	2	2	0	30	29	32	29	29	10	27	27	22
	mean	38.959	39.931	n.a.	0.052	0.167	1.135	6.783	2.990	1.726	171.307	218.727	2.618
	st. dev	8.207	0.126	n.a.	0.210	0.078	1.618	2.147	3.038	0.238	34.282	38.536	1.366
Suspended sediment [mg/kg]	#	0	0	0	0	0	22	0	0	22	0	0	22
	mean	n.a.	n.a.	n.a.	n.a.	n.a.	2.619	n.a.	n.a.	0.683	n.a.	n.a.	53.400
	st. dev	n.a.	n.a.	n.a.	n.a.	n.a.	4.238	n.a.	n.a.	1.842	n.a.	n.a.	74.987
Soil [mg/kg]	#	0	0	0	0	0	0	0	0	0	0	0	0
	mean	n.a.	n.a.	n.a.	n.a.	n.a.	n.a.	n.a.	n.a.	n.a.	n.a.	n.a.	n.a.
	st. dev	n.a.	n.a.	n.a.	n.a.	n.a.	n.a.	n.a.	n.a.	n.a.	n.a.	n.a.	n.a.
Groundwater [mg/l]	#	0	0	55	0	0	55	0	0	56	0	0	0
	mean	n.a.	n.a.	0.095	n.a.	n.a.	0.001	n.a.	n.a.	0.002	n.a.	n.a.	n.a.
	st. dev	n.a.	n.a.	0.091	n.a.	n.a.	0.001	n.a.	n.a.	0.004	n.a.	n.a.	n.a.
Surface water [mg/l]	#	6	6	0	29	29	30	29	29	31	31	31	23
	mean	1.788	2.329	n.a.	1.119	1.692	0.015	0.057	0.034	0.006	0.109	0.166	0.001
	st. dev	4.280	5.643	n.a.	0.562	0.873	0.063	0.178	0.019	0.015	0.124	0.122	0.002

Compartment		Cu			Fe			Hg			Mn		
		W	D	U	W	D	U	W	D	U	W	D	U
Sediment [mg/kg]	#	0	0	0	27	27	22	33	33	27	27	27	0
	mean	n.a.	n.a.	n.a.	1138.552	1354.513	3960.803	0.387	0.508	0.157	183.904	234.742	n.a.
	st. dev	n.a.	n.a.	n.a.	315.643	292.177	3111.026	0.624	1.045	0.207	332.209	594.105	n.a.
Suspended sediment [mg/kg]	#	0	0	0	0	0	22	0	0	22	0	0	0
	mean	n.a.	n.a.	n.a.	n.a.	n.a.	27619.295	n.a.	n.a.	1244.098	n.a.	n.a.	n.a.
	st. dev	n.a.	n.a.	n.a.	n.a.	n.a.	36828.791	n.a.	n.a.	5457.144	n.a.	n.a.	n.a.
Soil [mg/kg]	#	0	0	0	0	0	0	21	21	5	0	0	0
	mean	n.a.	n.a.	n.a.	n.a.	n.a.	n.a.	0.605	0.069	0.084	n.a.	n.a.	n.a.
	st. dev	n.a.	n.a.	n.a.	n.a.	n.a.	n.a.	1.540	0.238	0.038	n.a.	n.a.	n.a.
Groundwater [mg/l]	#	0	0	0	0	0	56	6	6	55	0	0	56
	mean	n.a.	n.a.	n.a.	n.a.	n.a.	0.262	0.0003	0.0004	0.0083	n.a.	n.a.	0.117
	st. dev	n.a.	n.a.	n.a.	n.a.	n.a.	0.313	0.0002	0.0001	0.0205	n.a.	n.a.	0.132
Surface water [mg/l]	#	31	31	0	31	31	30	43	43	23	31	31	0
	mean	0.274	0.338	n.a.	2.586	4.846	7.314	0.087	0.099	0.001	0.048	0.154	n.a.
	st. dev	0.265	0.390	n.a.	2.739	3.322	23.913	0.119	0.129	0.002	0.214	0.219	n.a.

Compartment		Ni			Pb			Se			Zn		
		W	D	U	W	D	U	W	D	U	W	D	U
Sediment [mg/kg]	#	27	27	22	27	27	32	0	0	0	27	27	31
	mean	73.516	79.928	2.920	132.864	335.378	5.521	n.a.	n.a.	n.a.	35.623	118.323	5.960
	st. dev	32.584	34.074	1.951	55.665	289.156	1.887	n.a.	n.a.	n.a.	32.440	169.540	3.819
Suspended sediment [mg/kg]	#	0	0	22	0	0	22	0	0	0	0	0	22
	mean	n.a.	n.a.	22.657	n.a.	n.a.	9.182	n.a.	n.a.	n.a.	n.a.	n.a.	1220.655
	st. dev	n.a.	n.a.	29.461	n.a.	n.a.	17.194	n.a.	n.a.	n.a.	n.a.	n.a.	3482.276
Soil [mg/kg]	#	0	0	0	0	0	0	0	0	0	0	0	0
	mean	n.a.	n.a.	n.a.	n.a.	n.a.	n.a.	n.a.	n.a.	n.a.	n.a.	n.a.	n.a.
	st. dev	n.a.	n.a.	n.a.	n.a.	n.a.	n.a.	n.a.	n.a.	n.a.	n.a.	n.a.	n.a.
Groundwater [mg/l]	#	0	0	0	0	0	56	0	0	55	0	0	56
	mean	n.a.	n.a.	n.a.	n.a.	n.a.	0.017	n.a.	n.a.	0.049	n.a.	n.a.	0.036
	st. dev	n.a.	n.a.	n.a.	n.a.	n.a.	0.014	n.a.	n.a.	0.058	n.a.	n.a.	0.041
Surface water [mg/l]	#	31	31	31	31	31	30	0	0	0	31	31	30
	mean	0.287	0.073	0.289	0.894	0.151	0.010	n.a.	n.a.	n.a.	0.028	3.147	0.173
	st. dev	0.419	0.049	1.466	0.450	0.189	0.053	n.a.	n.a.	n.a.	0.130	2.097	0.210

Table 18: Mean, standard deviation and count of environmental pollution data by environmental compartment and season. W = wet season; D = dry season; U = Unspecified season.

L.2. Statistics by compartment and subbasin

Concentration in sediment [mg/kg]													
Subbasin	**Value**	**Al**	**As**	**Cd**	**Cr**	**Cu**	**Fe**	**Hg**	**Mn**	**Ni**	**Pb**	**Se**	**Zn**
WHO Limit		**1**	**7**	**1.1**	**50**	**36**	**28000**	**2**	**600**	**25.00**	**23**	**n.a.**	**88**
Lower Pra	Count	4	22	22	18	0	18	50	18	18	18	0	18
	Mean	39.44	0.09	4.66	166.41	n.a.	1091.10	0.16	428.18	69.88	195.69	n.a.	86.70
	STD	4.13	0.11	3.26	39.46	n.a.	287.19	0.43	766.79	35.12	273.34	n.a.	114.04
Middle Pra	Count	0	0	0	0	0	0	0	0	0	0	0	0
	Mean	n.a.	n.a.	n.a.	n.a.	n.a.	n.a.	n.a.	n.a.	n.a.	n.a.	n.a.	n.a.
	STD	n.a.	n.a.	n.a.	n.a.	n.a.	n.a.	n.a.	n.a.	n.a.	n.a.	n.a.	n.a.
Upper Pra	Count	0	0	0	0	0	0	16	0	0	0	0	0
	Mean	n.a.	n.a.	n.a.	n.a.	n.a.	n.a.	1.39	n.a.	n.a.	n.a.	n.a.	n.a.
	STD	n.a.	n.a.	n.a.	n.a.	n.a.	n.a.	1.13	n.a.	n.a.	n.a.	n.a.	n.a.
Birim	Count	0	32	10	22	0	32	25	0	22	32	0	32
	Mean	n.a.	1.14	1.73	2.62	n.a.	2900.83	0.11	n.a.	2.92	5.52	n.a.	6.08
	STD	n.a.	1.59	0.23	1.33	n.a.	2970.41	0.14	n.a.	1.91	1.86	n.a.	3.75
Offin	Count	0	34	34	34	0	34	2	34	34	34	0	34
	Mean	n.a.	0.09	5.08	209.83	n.a.	1314.15	0.27	99.68	80.62	260.61	n.a.	76.30
	STD	n.a.	0.10	3.11	37.13	n.a.	305.95	0.14	76.25	31.79	202.22	n.a.	135.00

Concentration in surface water [mg/l]													
Subbasin	**Value**	**Al**	**As**	**Cd**	**Cr**	**Cu**	**Fe**	**Hg**	**Mn**	**Ni**	**Pb**	**Se**	**Zn**
WHO Limit		**0.2**	**0.01**	**0.003**	**0.05**	**2**	**0.3**	**0.001**	**0.4**	**0.07**	**0.01**	**0.01**	**3**
Lower Pra	Count	6	22	22	20	20	20	66	20	20	20	0	20
	Mean	0.0113	1.2159	0.0203	0.1465	0.2867	2.9720	0.1211	0.0704	0.1619	0.5680	n.a.	1.6085
	STD	0.0153	0.8772	0.0259	0.1336	0.1423	1.7618	0.1273	0.1099	0.1835	0.5081	n.a.	2.1062
Middle Pra	Count	0	0	0	0	0	0	0	0	0	0	0	0
	Mean	n.a.	n.a.	n.a.	n.a.	n.a.	n.a.	n.a.	n.a.	n.a.	n.a.	n.a.	n.a.
	STD	n.a.	n.a.	n.a.	n.a.	n.a.	n.a.	n.a.	n.a.	n.a.	n.a.	n.a.	n.a.
Upper Pra	Count	0	0	0	0	0	0	16	0	0	0	0	0
	Mean	n.a.	n.a.	n.a.	n.a.	n.a.	n.a.	0.0004	n.a.	n.a.	n.a.	n.a.	n.a.
	STD	n.a.	n.a.	n.a.	n.a.	n.a.	n.a.	0.0002	n.a.	n.a.	n.a.	n.a.	n.a.
Birim	Count	4	22	22	26	4	26	24	4	26	26	0	26
	Mean	6.1245	0.0014	0.0001	0.0062	0.0430	2.0051	0.0002	0.6320	0.0040	0.0020	n.a.	0.0594
	STD	6.1738	0.0011	0.0001	0.0203	0.0432	4.3779	0.0002	0.5681	0.0053	0.0060	n.a.	0.0292
Offin	Count	2	41	42	37	36	43	3	36	44	43	0	43
	Mean	0.0695	1.3253	0.0559	0.1457	0.3616	4.7337	0.0034	0.0638	0.3725	0.4871	n.a.	1.5784
	STD	0.0315	0.8200	0.1445	0.1206	0.4004	4.0095	0.0046	0.0823	1.2403	0.5011	n.a.	2.1128

Concentration in groundwater [mg/l]													
Subbasin	**Value**	**Al**	**As**	**Cd**	**Cr**	**Cu**	**Fe**	**Hg**	**Mn**	**Ni**	**Pb**	**Se**	**Zn**
WHO Limit		**0.2**	**0.01**	**0.003**	**0.05**	**2**	**0.3**	**0.001**	**0.4**	**0.07**	**0.01**	**0.01**	**3**
Lower Pra	Count	24	24	24	0	24	24	24	24	0	24	24	24
	Mean	0.110	0.001	0.001	n.a.	0.024	0.315	0.005	0.152	n.a.	0.010	0.027	0.043
	STD	0.084	0.000	0.001	n.a.	0.037	0.378	0.006	0.170	n.a.	0.009	0.040	0.049
Middle Pra	Count	26	26	26	0	26	26	26	26	0	26	26	26
	Mean	0.084	0.001	0.002	n.a.	0.024	0.219	0.012	0.079	n.a.	0.024	0.076	0.029
	STD	0.087	0.001	0.005	n.a.	0.028	0.246	0.028	0.056	n.a.	0.016	0.063	0.033
Upper Pra	Count	0	0	0	0	0	0	12	0	0	0	0	0
	Mean	n.a.	n.a.	n.a.	n.a.	n.a.	n.a.	n.a.	n.a.	n.a.	n.a.	n.a.	n.a.
	STD	n.a.	n.a.	n.a.	n.a.	n.a.	n.a.	n.a.	n.a.	n.a.	n.a.	n.a.	n.a.
Birim	Count	3	3	3	0	3	3	3	3	0	3	3	3
	Mean	0.130	0.002	0.001	n.a.	0.013	0.363	0.003	0.219	n.a.	0.012	0.021	0.051
	STD	0.140	0.001	0.000	n.a.	0.002	0.234	0.000	0.143	n.a.	0.006	0.009	0.028
Offin	Count	1	1	2	0	2	2	1	2	0	2	1	2
	Mean	0.005	0.001	0.001	n.a.	0.015	0.120	0.005	0.075	n.a.	0.012	0.006	0.010
	STD	0.000	0.000	0.001	n.a.	0.005	0.046	0.000	0.063	n.a.	0.002	0.000	0.005

Table 19: Mean, standard deviation and count of environmental pollution data by environmental compartment and subbasin.

L.3. WHO exceedance by environmental compartment and season

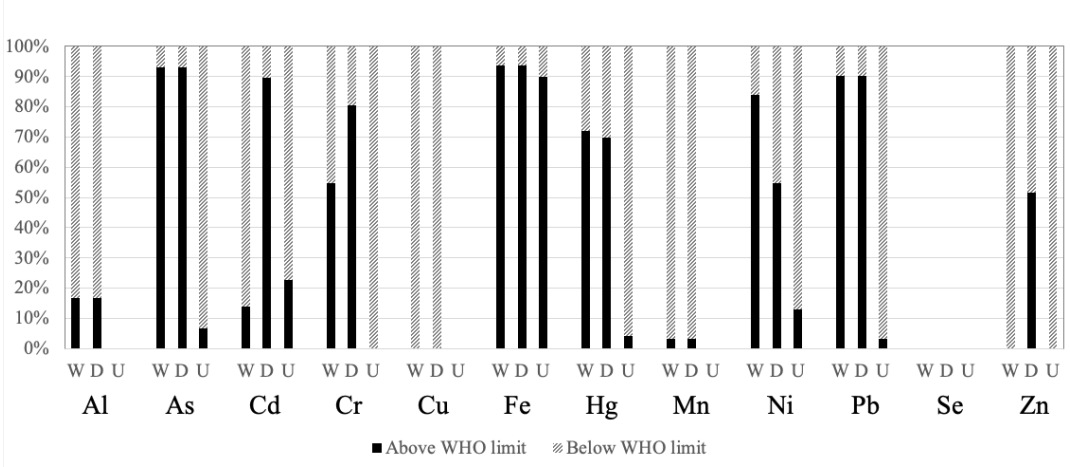

Figure 32: Fraction of surface water heavy metal concentration measurements above and below WHO recommended limits for drinking water as listed in Appendix D by season. W = wet season; D = dry season; U = Unspecified season.

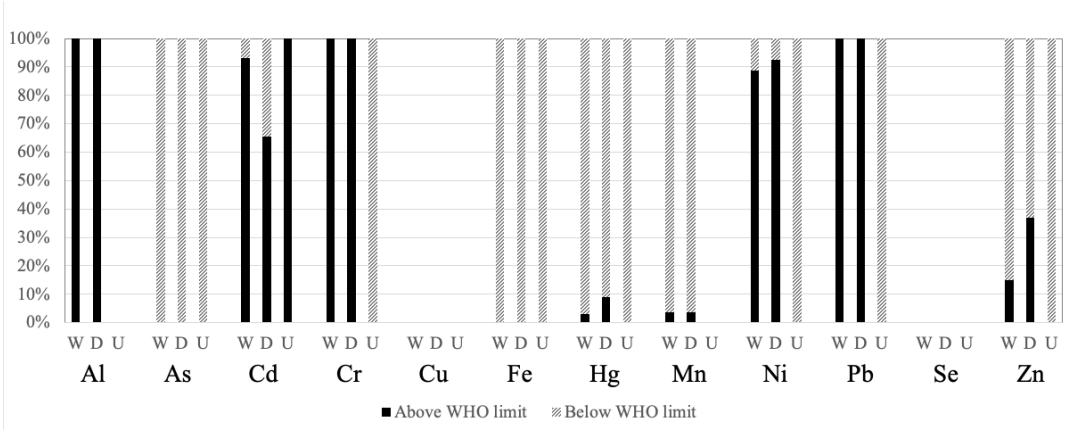

Figure 33: Fraction of sediment heavy metal concentration measurements above and below WHO recommended limits for sediment as listed in Appendix D by season. W = wet season; D = dry season; U = Unspecified season.

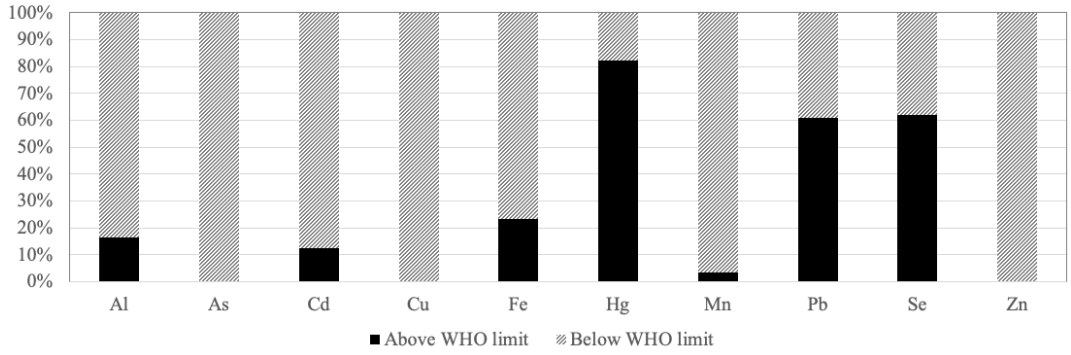

Figure 34: Fraction of groundwater heavy metal concentration measurements above and below WHO recommended limits for groundwater as listed in Appendix D by season. W = wet season; D = dry season; U = Unspecified season.

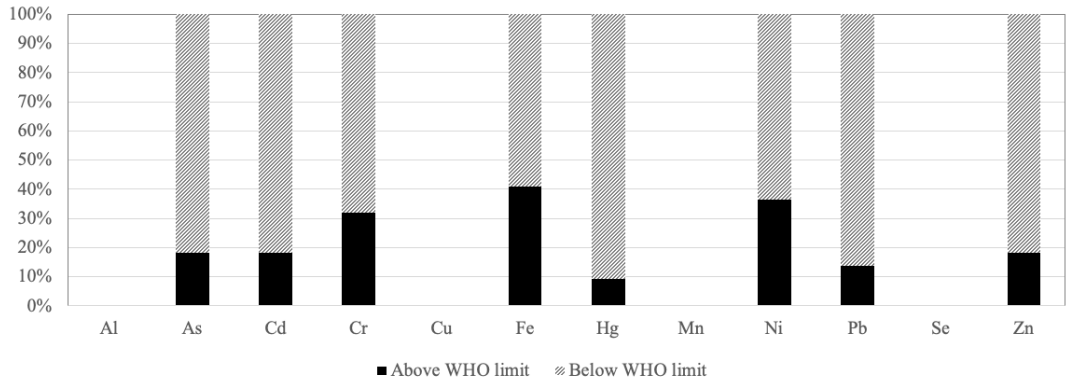

Figure 35: Fraction of suspended sediment heavy metal concentration measurements above and below WHO recommended limits for sediment as listed in Appendix D by season. W = wet season; D = dry season; U = Unspecified season.

L.4. WHO exceedance by environmental compartment and subbasin

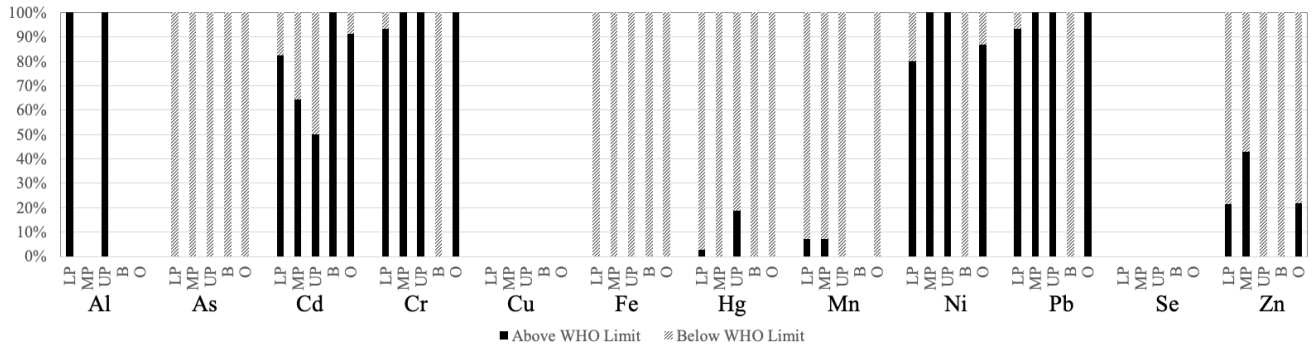

Figure 36: Fraction of sediment heavy metal concentration measurements above and below the WHO recommended limits for sediments as listed in Appendix D. Subbasins are designated as follows: LP = Lower Pra; MP = Middle Pra; UP = Upper Pra; B = Birim; O = Offin;

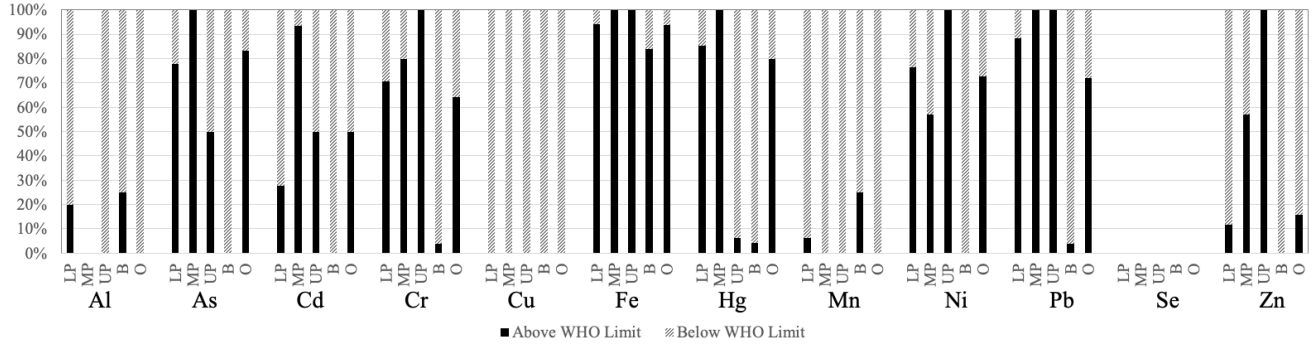

Figure 37: Fraction of surface water heavy metal concentration measurements above and below the WHO recommended limits for drinking water as listed in Appendix D. Subbasins are designated as follows: LP = Lower Pra; MP = Middle Pra; UP = Upper Pra; B = Birim; O = Offin;

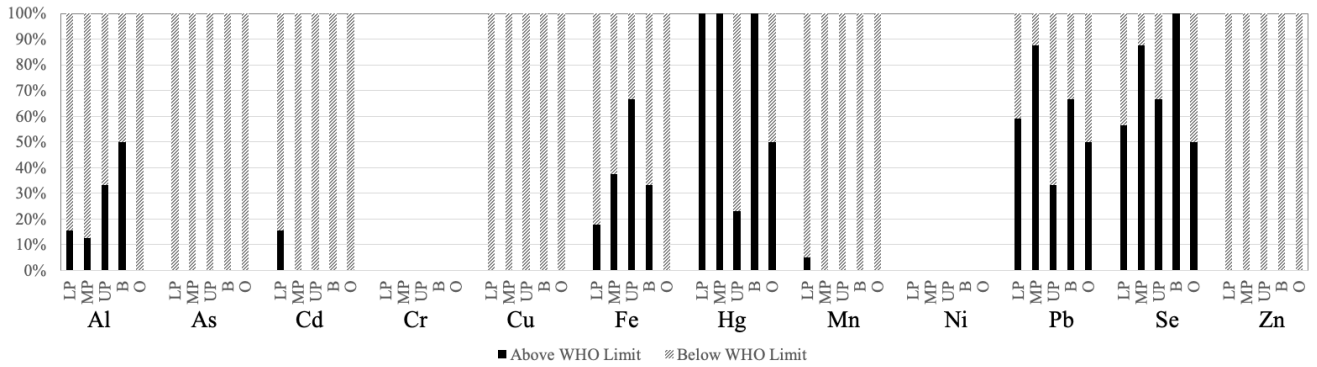

Figure 38: Fraction of groundwater heavy metal concentration measurements above and below the WHO recommended limits for drinking water as listed in Appendix D. Subbasins are designated as follows: LP = Lower Pra; MP = Middle Pra; UP = Upper Pra; B = Birim; O = Offin;

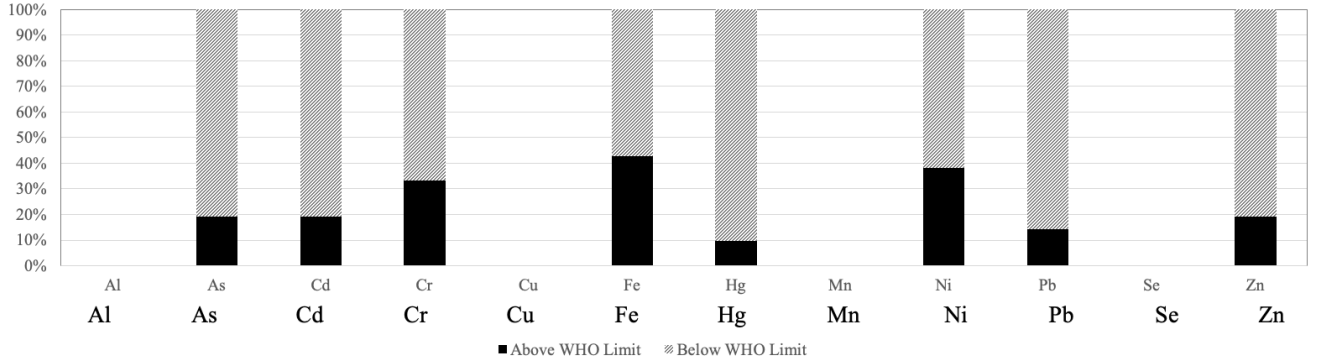

Figure 39: Fraction of suspended sediment heavy metal concentration measurements above and below the WHO recommended limits for sediments in the Birim subbasin as listed in Appendix D.

L.5. Heavy metal concentrations in fish

Figure 20 compares the statistics of various heavy metal concentrations tested in fish within the basin.

Table 20: Heavy metal concentrations recorded for various fish types in the basin.

Fish concentration [mg/kg]				
Value	**Cd**	**Cr**	**Hg**	**Ni**
Count	3	3	18	3
Mean	7.72	6.54	0.21	20.18
STD	2.88	0.74	0.34	3.31

Interestingly, fish further upstream in the Barekese reservoir presented with the highest heavy metal pollution (data only provided in Digital Appendix), compared to fish from far downstream in the Lower Pra reach. This might be due to the fish of the Barekese reservoir passing through the heavily polluted waters of the Offin, thereby absorbing high concentrations of heavy metals.

M. Floodplain inundation modelling

The case study locations are visualized in Figure 40. Computed Gumbel curves and values are summarized in Figure 41 and Table 21 respectively. Tables 22, 23 and 24 show maximum inundation area, longitudinal expansion and the raw mean channel width data.

M.1. Locations of the case studies

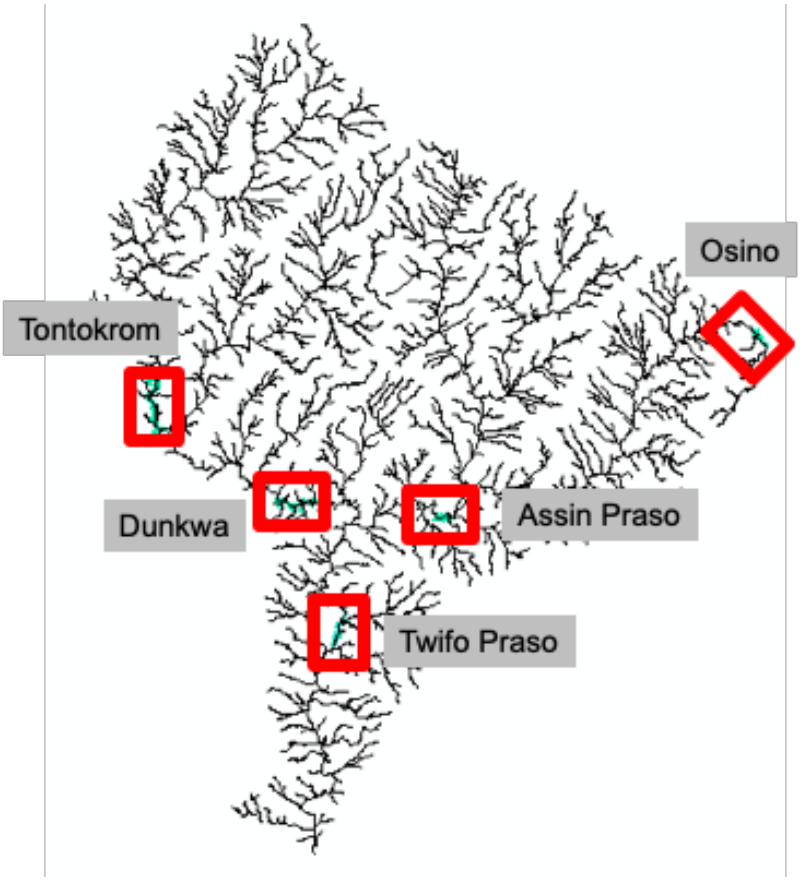

Figure 40: Case study locations used in the 2D Floodplain Model in HEC-RAS.

M.2. Gumbel frequency curves

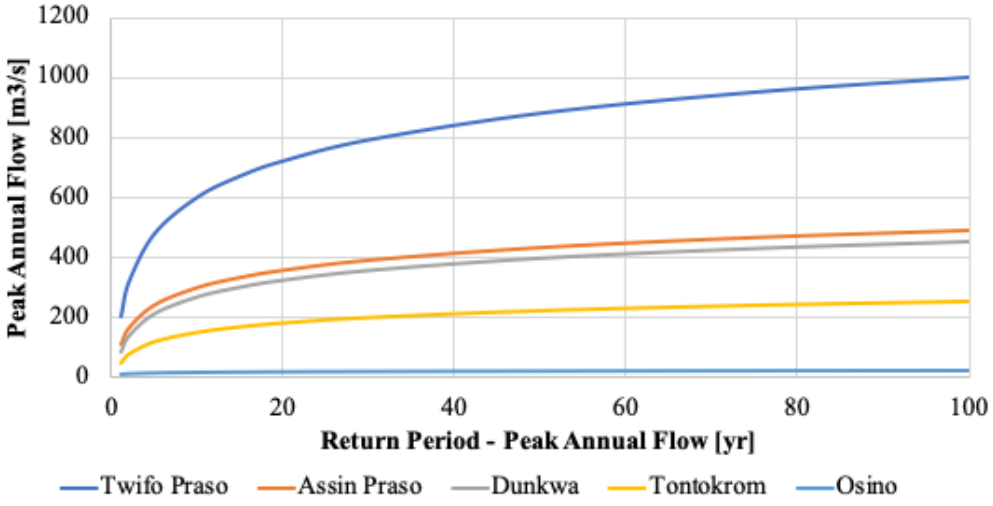

Figure 41: Gumbel frequency curves derived from annual maximum monthly flow values of the FLO1K dataset (1960-2015) for each case study location.

Table 21: Gumbel frequency flow data derived from annual maximum mean monthly flows of the FLO1K dataset (1960-2015).

Return period	Twifo Praso	Assin Praso	Dunkwa	Tontokrom	Osino
1	203.1	108.4	82.0	44.9	7.2
2	323.4	165.1	137.7	75.8	9.6
5	482.4	240.1	211.3	116.5	12.8
10	602.7	296.8	267.1	147.4	15.2
15	673.1	330.0	299.7	165.4	16.6
20	723.1	353.6	322.8	178.2	17.6
30	793.4	386.7	355.4	196.3	19.0
50	882.1	428.5	396.4	219.0	20.7
75	952.5	461.7	429.0	237.0	22.1
100	1002.4	485.3	452.2	249.8	23.1

M.3. Mean channel width

Table 22: Maximum inundation area [m2] by case study and return period, resulting from the 2D Floodplain Modelling in HEC-RAS.

Return Period [yr]	Maximum inundation area [m^2]				
	Twifo Praso	**Assin Praso**	**Dunkwa**	**Tontokrom**	**Osino**
1	863595	3826552	1227325	1978964	490345
2	958163	4283539	2219817	2338924	583388
5	1051933	4795211	2829295	2574035	676636
10	1149127	5615127	3084912	2773241	736205
15	1186394	6038813	3192692	2836364	781207
20	1206292	6243745	3311579	2896546	800320
50	1267586	6605991	3631530	3059270	845224

Table 23: Longitudinal expansion [m] by case study and return period, resulting from the 2D Floodplain Modelling in HEC-RAS.

Return Period [yr]	Longitudinal expansion [m]				
	Twifo Praso	**Assin Praso**	**Dunkwa**	**Tontokrom**	**Osino**
1	12926	26122	13493	17419	9305
2	12926	26222	25200	18219	9705
5	13426	26272	29600	18219	10005
10	15126	30192	29600	18219	10125
15	15126	31692	29600	19088	10245
20	15126	32392	29600	19088	10245
50	15126	33142	31038	19588	10245

Table 24: Mean channel width, calculated as the quotient of total inundated area and longitudinal expansion.

	Mean Channel Width [m]				
R [yr]	**Twifo Praso**	**Assin Praso**	**Dunkwa**	**Tontokrom**	**Birim**
1	66.81	146.49	90.96	113.61	52.70
2	74.13	163.36	88.09	128.38	60.11
5	78.35	182.52	95.58	141.28	67.63
10	75.97	185.98	104.22	152.22	72.71
15	78.43	190.55	107.86	148.59	76.25
20	79.75	192.76	111.88	151.75	78.12
50	83.80	199.32	117.00	156.18	82.50